Observations and Results of the FLOHOF Field Campaign 2007

Rafael Kühnel

Ludwig-Maximilians-Universität München

2008

Observations and Results of the FLOHOF Field Campaign 2007

Rafael Kühnel

Diploma Thesis

Advisor

Prof. Dr. J. Egger

Second Advisor

Dr. G. Zängl

Department of Physics

Ludwig-Maximilians-Universität München

2008

Declaration

I hereby declare that i wrote this thesis myself without sources other than those indicated herein.

Munich, June 2008

Contents

Chapter 1

Introduction

The effects of mountain topography on the atmosphere have been studied by a large variety of works. Especially the generation and development of waves through mountains and their influence on meteorological phenomena has gained significant interest.

A less detailed but broad view on the effects of mountains and the generation of waves is given by Smith (1979). The cause for topographically induced waves are buoyancy forces which tend to bring displaced air parcels back to their equilibrium level. Hence, these waves are referred to as buoyancy waves, or gravity waves. Of course, such restoring forces can only occur in stable stratifications. The stability of the atmosphere is therefore a crucial factor. Two other main factors are the flow over the topography and, of course, the topography itself. For small scale hills and mountains, the time it takes an air parcel to travel over the topography is normally less then a buoyancy oscillation which is the time needed to bring an air parcel back to equilibrium level once displaced. Therefore, buoyancy forces play a minor role compared to turbulent Reynolds stresses.

With increasing scale of the topography, the boundary layer becomes thinner, in relation to the flow scale, until buoyancy forces dominate the influence on the flow. For mountains with a horizontal extension of 10 kilometres or more, vertical accelerations are relatively small and the pressure field is nearly hydrostatic.

The assumption of hydrostatic balance simplifies the governing equations but eliminate any trapped waves propagating downstream. The assumption is thus only valid for small amplitude and gently sloped mountains. Another constraint is the constant background flow and stability. The influence of the hydrostatic assumption on the generated waves was studied by Keller (1994).

For narrow ridges or high velocities of the background flow, the waves are decaying with height. The phase lines are vertical and the flow is close to an

irrotational one. However, the decay of the vertical displacement with height is bound to accelerations and the hydrostatic assumption is no longer valid. Wider ridges and low velocities will tend to form vertical propagating waves without decay. The phase lines of these waves tilt upstream. A fact that is caused by the upward transport of energy away from the topography that caused the wave. The flow is asymmetric near the ground with low speed and high pressure on the windward side and high speed and low pressure on the leeward side. This asymmetry causes a pressure drag on the topography and this momentum is transported vertically by the waves. The influence of wind shear on the drag of buoyancy waves was studied by Teixeira and Miranda (2004).

The flow over a mountain is often considered to be part of a large scale system. This leads to the assumption that the excited waves are stationary. Still, some works have considered instationary conditions. Bell (1974) studied the generation of waves by a time dependent flow. He assumed a harmonic time dependence. His results showed, that waves are not only generated by the fundamental frequency of the time dependency, but also at all of its harmonics. Further studies on waves, generated by a transient wind, have been performed for example by Lott and Teitelbaum (1993). They considered a wind starting from zero and returning to zero after a finite time. Bannon and Zehnder (1985) considered the surface pressure and mountain drag for a oscillating airflow. They showed, that during the accelerations of the airflow, the vertically decaying modes deepen and broaden the pressure asymmetry.

In the period from 20 July to 24 August, 2007, the *FLOHOF* (FLow Over an around HOFsjökull) field campaign took place at Hofsjökull in central Iceland. The aim of this campaign was to observe and analyse how the flow over and around an 'ideal' mountain evolves in time. Special interest was laid on the impact of instationary flows on the waves exerted by Hofsjökull (see section 3.1 for further information on this mountain), since no field program has been performed yet to investigate the transience of mountain waves. During the *FLOHOF* field campaign, 18 autonomous weather stations have been placed on and around Hofsjökull. Balloon soundings had been done in the north of the mountain to get a view on wind profiles in the vertical. Remotely controlled model planes (*KALI*) have been used to measure vertical temperature and humidity profiles.

This work gives a view on the campaign and the observations of the autonomous weather stations, as well as on the balloon and *KALI* soundings. Two and three-dimensional, linear and hydrostatic models were analysed for an ideal mountain as well as for the Hofsjökull topography. Chapter 2 illustrates the basic gravity wave theory, as well as the models used. Chapter 3 gives an overview of the instrumentation of the autonomous weather sta-

tions, balloon soundings and *KALI* soundings. In chapter 4 the results of the measurements during the field campaign and of all model calculations are presented. Chapter 5 gives a discussion of the observations and the model calculations. In chapter 6, a summary is given. Additional plots can be found in the appendix, chapter A.

Chapter 2

Theory

2.1 Buoyancy Force

The basic force leading to gravity waves is the buoyancy force. Therefore gravity waves are often referred to as buoyancy waves. The vertical momentum equation for an inviscid fluid can be written as

$$\frac{Dw}{Dt} = -\frac{1}{\rho}\frac{\partial p}{\partial z} - g$$

The background pressure field (p_0 in the following) is hydrostatic, if the pressure force closely balances the gravitational force.

$$\frac{1}{\rho_0}\frac{\partial p_0}{\partial z} = -g \tag{2.1}$$

It is assumed that the pressure of the parcel adjusts instantaneously to the environmental pressure field once displaced, so that $p = p_0$. The pressure in the equation above can be replaced with the help of the hydrostatic equation (2.1)

$$\frac{Dw}{Dt} = -\frac{1}{\rho}\frac{\partial p}{\partial z} - g = g\Big(\frac{\rho_0 - \rho}{\rho}\Big)$$

The parcel undergoes a net upward force, if it is less dense than its surroundings, and a net downward force, if it is denser than the surrounding air. This force is called buoyancy. Density differences can be created in two ways. First, by local heating or cooling of the parcel, and second, by moving the parcel into a different environment.

2.2 Basic Equations

To derive an expression for orographic induced gravity waves, we start from the well known momentum equations, the continuity equation and the thermodynamic equation. We consider an incompressible hydrostatic atmosphere. The Boussinesq approximation is employed in which density is treated as a constant except where it is coupled with gravity. Effects of rotation are neglected. To simplify the equations we follow the methods as described by Holton (2004).

$$\frac{\partial u}{\partial t} + u\frac{\partial u}{\partial x} + v\frac{\partial u}{\partial y} + w\frac{\partial u}{\partial z} + \frac{1}{\rho}\frac{\partial p}{\partial x} = 0 \tag{2.2}$$

$$\frac{\partial v}{\partial t} + u\frac{\partial v}{\partial x} + v\frac{\partial v}{\partial y} + w\frac{\partial v}{\partial z} + \frac{1}{\rho}\frac{\partial p}{\partial y} = 0 \tag{2.3}$$

$$\frac{\partial w}{\partial t} + u\frac{\partial w}{\partial x} + v\frac{\partial w}{\partial y} + w\frac{\partial w}{\partial z} + \frac{1}{\rho}\frac{\partial p}{\partial z} + g = 0 \tag{2.4}$$

$$\frac{\partial u}{\partial x} + \frac{\partial v}{\partial y} + \frac{\partial w}{\partial z} = 0 \tag{2.5}$$

$$\frac{\partial \Theta}{\partial t} + u\frac{\partial \Theta}{\partial x} + v\frac{\partial \Theta}{\partial y} + w\frac{\partial \Theta}{\partial z} = 0 \tag{2.6}$$

u and v are the horizontal wind components, w is the vertical wind component, ρ is density, p is pressure, g is the gravitational acceleration and Θ is potential temperature. These equations are now linearised by:

$$\begin{aligned} u &= U + u' \\ v &= V + v' \\ w &= w' \\ \Theta &= \Theta_0 + \Theta' \\ p &= p_0 + p' \\ \rho &= \rho_0 + \rho' \end{aligned}$$

U and V are mean wind components, which might vary with height, Θ_0 and p_0 are background potential temperature and background pressure, as well only dependent on height. ρ_0 is the background density, which is constant. Primed variables designate the deviation from basic state. By using these expressions in the equations above one gets:

$$\frac{\partial u'}{\partial t} + U\frac{\partial u'}{\partial x} + V\frac{\partial u'}{\partial y} + w'\frac{\partial U}{\partial z} + \frac{1}{\rho_0}\frac{\partial p'}{\partial x} = 0 \tag{2.7}$$

$$\frac{\partial v'}{\partial t} + U\frac{\partial v'}{\partial x} + V\frac{\partial v'}{\partial y} + w'\frac{\partial V}{\partial z} + \frac{1}{\rho_0}\frac{\partial p'}{\partial y} = 0 \tag{2.8}$$

$$\frac{\partial w'}{\partial t} + U\frac{\partial w'}{\partial x} + V\frac{\partial w'}{\partial y} + \frac{1}{\rho_0 + \rho'}\frac{\partial (p_0 + p')}{\partial z} + g = 0 \tag{2.9}$$

$$\frac{\partial u'}{\partial x} + \frac{\partial v'}{\partial y} + \frac{\partial w'}{\partial z} = 0 \tag{2.10}$$

$$\frac{\partial \Theta'}{\partial t} + U\frac{\partial \Theta'}{\partial x} + V\frac{\partial \Theta'}{\partial y} + w'\frac{\partial \Theta_0}{\partial z} = 0 \tag{2.11}$$

Products of deviations from basic state were neglected. The last two terms in equation (2.9) can be approximated as:

$$\frac{1}{\rho_0 + \rho'}\frac{\partial (p_0 + p')}{\partial z} + g = \frac{1}{\rho_0(1 + \frac{\rho'}{\rho_0})}\Big(\frac{\partial p_0}{\partial z} + \frac{\partial p'}{\partial z}\Big) + g = \frac{(1 - \frac{\rho'}{\rho_0})}{\rho_0(1 - (\frac{\rho'}{\rho_0})^2)}\Big(\frac{\partial p_0}{\partial z} + \frac{\partial p'}{\partial z}\Big) + g \tag{2.12}$$

$(\frac{\rho'}{\rho_0})^2$ is assumed to be small and thus can be neglected. The background pressure satisfies the hydrostatic equation

$$\frac{\partial p_0}{\partial z} = -\rho_0 g \tag{2.13}$$

therefore equation (2.12) can be simplified to:

$$\frac{1}{\rho_0}\Big(1 - \frac{\rho'}{\rho_0}\Big)\frac{\partial p_0}{\partial z} + \frac{1}{\rho_0}\frac{\partial p'}{\partial z} + g = \frac{1}{\rho_0}\frac{\partial p'}{\partial z} + \frac{\rho'}{\rho_0}g$$

The last expression in the equation above can be replaced by an expression for the potential temperature. The potential temperature is defined by:

$$\Theta = \frac{p}{\rho R}\Big(\frac{p_s}{p}\Big)^{\kappa}$$

where R is the gas constant for dry air and $\kappa = \frac{R}{c_p}$, with c_p the specific heat of dry air at constant pressure. p_s is the pressure at a basic level, usually 1000 hPa. Taking the logarithm of the potential temperature gives:

$$\ln\Theta = \ln p - (\ln\rho + \ln R) + \kappa(\ln p_s - \ln p)$$

by using $c_p = c_v + R$, with c_v the specific heat of dry air at constant volume, one yields:

$$\ln\Theta = \ln p - (\ln\rho + \ln R) + (1 - \frac{c_v}{c_p})(\ln p_s - \ln p) =$$
$$\frac{1}{\gamma}\ln p - \ln\rho + constant \tag{2.14}$$

with $\gamma = \frac{c_v}{c_p}$. If one uses the linearised expressions for Θ, p and ρ one gets:

$$\ln\left(\Theta_0(1 + \frac{\Theta'}{\Theta_0})\right) = \frac{1}{\gamma}\ln\left(p_0(1 + \frac{p'}{p_0})\right) - \ln\left(\rho_0(1 + \frac{\rho'}{\rho_0})\right) + constant$$

using the approximation $\ln(1+\epsilon) \approx \epsilon$ for $\epsilon \ll 1$ and keeping in mind, that Θ satisfies equation (2.14), the equation above simplifies to:

$$\frac{\Theta'}{\Theta_0} \approx \frac{1}{\gamma}\frac{p'}{p_0} - \frac{\rho'}{\rho_0}$$

solving for ρ' yields:

$$\rho' \approx -\rho_0\frac{\Theta'}{\Theta_0} + \frac{\rho_0}{\gamma}\frac{p'}{p_0}$$

For buoyancy waves, density fluctuations due to pressure changes are small compared to those due to temperature changes. Therefore, the second term in the equation above can be neglected.

$$\frac{\Theta'}{\Theta_0} = -\frac{\rho'}{\rho_0}$$

The equations of motion can be written as:

$$\frac{\partial u'}{\partial t} + U\frac{\partial u'}{\partial x} + V\frac{\partial u'}{\partial y} + w'\frac{\partial U}{\partial z} + \frac{1}{\rho_0}\frac{\partial p'}{\partial x} = 0 \tag{2.15}$$

$$\frac{\partial v'}{\partial t} + U\frac{\partial v'}{\partial x} + V\frac{\partial v'}{\partial y} + w'\frac{\partial V}{\partial z} + \frac{1}{\rho_0}\frac{\partial p'}{\partial y} = 0 \tag{2.16}$$

$$\frac{\partial w'}{\partial t} + U\frac{\partial w'}{\partial x} + V\frac{\partial w'}{\partial y} + \frac{1}{\rho_0}\frac{\partial p'}{\partial z} - g\frac{\Theta'}{\Theta_0} = 0 \tag{2.17}$$

$$\frac{\partial u'}{\partial x} + \frac{\partial v'}{\partial y} + \frac{\partial w'}{\partial z} = 0 \tag{2.18}$$

$$\frac{\partial \Theta'}{\partial t} + U\frac{\partial \Theta'}{\partial x} + V\frac{\partial \Theta'}{\partial y} + w'\frac{\partial \Theta_0}{\partial z} = 0 \tag{2.19}$$

2.3 Linear 2D Model — Wave Solution

This model consideres a two–dimensional flow over a mountain ridge ($x - z$ plane) with constant horizontal wind component. The following methods are based on Holton (2004). The basic equation of motion from chapter 2.2 reduced to two dimensions are:

$$\frac{\partial u'}{\partial t} + U\frac{\partial u'}{\partial x} + \frac{1}{\rho_0}\frac{\partial p'}{\partial x} = 0 \tag{2.20}$$

$$\frac{\partial w'}{\partial t} + U\frac{\partial w'}{\partial x} + \frac{1}{\rho_0}\frac{\partial p'}{\partial z} - g\frac{\Theta'}{\Theta_0} = 0 \tag{2.21}$$

$$\frac{\partial u'}{\partial x} + \frac{\partial w'}{\partial z} = 0 \tag{2.22}$$

$$\frac{\partial \Theta'}{\partial t} + U\frac{\partial \Theta'}{\partial x} + w'\frac{\partial \Theta_0}{\partial z} = 0 \tag{2.23}$$

Subtracting the partial derivative of equation (2.21) with respect to z from the partial derivative of equation (2.20) with respect to x, we are able to eliminate p'

$$\frac{\partial}{\partial t}\Big(\frac{\partial w'}{\partial x} - \frac{\partial u'}{\partial z}\Big) + U\frac{\partial}{\partial x}\Big(\frac{\partial w'}{\partial x} - \frac{\partial u'}{\partial z}\Big) - \frac{g}{\Theta_0}\frac{\partial \Theta'}{\partial x} = 0$$

Partial differentiation of the equation above with respect to x and with the help of equation (2.22) we get:

$$\Big(\frac{\partial}{\partial t} + U\frac{\partial}{\partial x}\Big)\Big(\frac{\partial^2 w'}{\partial x^2} + \frac{\partial^2 w'}{\partial z^2}\Big) - \frac{g}{\Theta_0}\frac{\partial^2 \Theta'}{\partial x^2} = 0$$

By partial differentiation of equation (2.23) with respect to x two times and differentiation of the last equation, one yields a single equation for w'

$$\Big(\frac{\partial}{\partial t} + U\frac{\partial}{\partial x}\Big)^2\Big(\frac{\partial^2 w'}{\partial x^2} + \frac{\partial^2 w'}{\partial z^2}\Big) + \frac{g}{\Theta_0}\frac{\partial \Theta_0}{\partial z}\frac{\partial^2 w'}{\partial x^2} = 0$$

The last term in this equation can be written as:

$$\frac{g}{\Theta_0}\frac{\partial \Theta_0}{\partial z} = g\frac{\partial \ln \Theta_0}{\partial z} \equiv N^2 \tag{2.24}$$

where N^2 is the square of the buoyancy frequency.

$$\Big(\frac{\partial}{\partial t} + U\frac{\partial}{\partial x}\Big)^2\Big(\frac{\partial^2 w'}{\partial x^2} + \frac{\partial^2 w'}{\partial z^2}\Big) + N^2\frac{\partial^2 w'}{\partial x^2} = 0 \tag{2.25}$$

The airflow is assumed to be steady, therefore, the equation above reduces to:

$$\Big(U\frac{\partial}{\partial x}\Big)^2\Big(\frac{\partial^2 w'}{\partial x^2} + \frac{\partial^2 w'}{\partial z^2}\Big) + N^2\frac{\partial^2 w'}{\partial x^2} = 0$$

This equation has a solution of the form:

$$w' = \Re\{\widehat{w}\exp(i\phi)\} \tag{2.26}$$

where $\widehat{w} = \widehat{w_r} + i\widehat{w_i}$ is a complex amplitude and $\phi = kx + mz$ is the phase function depending on x and z with wave number k in the horizontal and m in the vertical. Applying the wavelike solution on the last equation we get the dispersion relationship for m

$$\begin{aligned} &(Uik)^2(i^2k^2 + i^2m^2) + N^2i^2k^2 = 0 \\ \Leftrightarrow &- U^2k^2(k^2 + m^2) + N^2k^2 = 0 \\ \Leftrightarrow &m = \pm\sqrt{\frac{N^2}{U^2} - k^2} \end{aligned} \tag{2.27}$$

For $\frac{N^2}{U^2} > k^2$ the root above is positive and m is real, leading to vertical propagating waves of the form $w' = \widehat{w}\exp(i(kx + mz))$. For $\frac{N^2}{U^2} < k^2$ the root is negative and m is imaginary. Vertical trapped waves of the form $w' = \widehat{w}\exp(ikx)\exp(-mz)$ will ocurr. From equation (2.27) one can see, that vertical propagation is only possible if $|N| > |Uk|$, which means that the frequency of the topography relative to the horizontal mean wind is less than the buoyancy frequency. Suitable conditions for propagating waves are those with stable stratification, weak horizontal mean wind and a topography with low wave numbers (wide ridges).

Concerning the sign of the root in equation (2.27) the following considerations have to be done. If m is imaginary the root has to be positive for a decay of the wave with height. For the case of vertical propagating waves we take a closer look at the group velocities. The solution for equation

(2.25) is the same as for equation (2.3), but with a different phase function ($\phi = kx + mz - \nu t$). The dispersion relationship of equation (2.25) is:

$$\begin{aligned}(\nu - Uk)^2(k^2 + m^2) - N^2k^2 &= 0\\ \Leftrightarrow \nu &= Uk \pm \frac{Nk}{\sqrt{k^2 + m^2}}\end{aligned}$$

The phase velocities are given by:

$$\begin{aligned}c_x &= \frac{\nu}{k} = U \pm \frac{N}{\sqrt{(k^2 + m^2)}}\\ c_z &= \frac{\nu}{m} = \frac{Uk}{m} \pm \frac{(Nk)}{m\sqrt{(k^2 + m^2)}}\end{aligned}$$

The group velocities are:

$$\begin{aligned}c_{gx} &= \frac{\partial \nu}{\partial k} = U \pm \frac{Nm^2}{\sqrt{(k^2 + m^2)^3}}\\ c_{gz} &= \frac{\partial \nu}{\partial m} = \pm\frac{(-Nkm)}{\sqrt{(k^2 + m^2)^3}}\end{aligned}$$

One can see, that the vertical group velocity c_{gz} has a sign opposite to that of the vertical phase speed c_z. The group velocity is perpendicular to the phase propagation. In the case of topographic waves the source of energy is the ground and energy is propagated upwards. This implies an upward component of the vertical group velocity and a downward component of the vertical phase speed. For this to be true m has to have the same sign as k.

2.4 Linear 2D Model — Pressure at the Lower Boundary

In the following, a solution for orography-induced gravity waves is developed in which pressure observations are used as a lower boundary condition. The usual method is to use $w = u\frac{\partial h}{\partial x}$ at the lower boundary, where u is the horizontal wind component, w is the vertical wind component and h is the topography. Here, pressure is used instead. This is done because pressure observations are available at the ground. The basis are the linearised equations (2.15) — (2.19) of motion from chapter 2.2.

$$\frac{\partial u'}{\partial t} + U\frac{\partial u'}{\partial x} + V\frac{\partial u'}{\partial y} + w'\frac{\partial U}{\partial z} + \frac{1}{\rho_0}\frac{\partial p'}{\partial x} = 0 \tag{2.28}$$

$$\frac{\partial v'}{\partial t} + U\frac{\partial v'}{\partial x} + V\frac{\partial v'}{\partial y} + w'\frac{\partial V}{\partial z} + \frac{1}{\rho_0}\frac{\partial p'}{\partial y} = 0 \tag{2.29}$$

$$\frac{1}{\rho_0}\frac{\partial p'}{\partial z} - g\frac{\Theta'}{\Theta_0} = 0 \tag{2.30}$$

$$\frac{\partial u'}{\partial x} + \frac{\partial v'}{\partial y} + \frac{\partial w'}{\partial z} = 0 \tag{2.31}$$

$$\frac{\partial \Theta'}{\partial t} + U\frac{\partial \Theta'}{\partial x} + V\frac{\partial \Theta'}{\partial y} + w'\frac{\partial \Theta_0}{\partial z} = 0 \tag{2.32}$$

Terms with w' in equation (2.30) were neglected because we consider hydrostatic conditions. By dividing equation (2.32) through Θ_0, the potential temperature can be replaced by a potential temperature perturbation normalized by the background potential temperature. Keeping the definition of buoyancy frequency in mind, equation (2.24), equation (2.32) can be written as:

$$\frac{\partial \tilde{\Theta}}{\partial t} + U\frac{\partial \tilde{\Theta}}{\partial x} + V\frac{\partial \tilde{\Theta}}{\partial y} + \frac{N^2}{g}w' = 0 \tag{2.33}$$

with $\tilde{\Theta} = \frac{\Theta'}{\Theta_0}$. Adding the partial derivative of equation (2.28) with respect to x and the partial derivative of equation (2.29) with respect to y one yields:

$$D\Big(\frac{\partial u'}{\partial x} + \frac{\partial v'}{\partial y}\Big) + \frac{\partial w'}{\partial x}\frac{\partial U}{\partial z} + \frac{\partial w'}{\partial y}\frac{\partial V}{\partial z} + \frac{1}{\rho_0}\Big(\frac{\partial^2 p'}{\partial x^2} + \frac{\partial^2 p'}{\partial y^2}\Big) = 0$$

D designates the total derivative by $D = \frac{\partial}{\partial t} + U\frac{\partial}{\partial x} + V\frac{\partial}{\partial y}$. With the help of equation (2.31) it follows:

$$-D\Big(\frac{\partial w'}{\partial z}\Big) + \frac{\partial w'}{\partial x}\frac{\partial U}{\partial z} + \frac{\partial w'}{\partial y}\frac{\partial V}{\partial z} + \frac{1}{\rho_0}\nabla_h^2 p' = 0 \tag{2.34}$$

The suffix h of the Nabla operator stands for horizontal. Solving (2.33) for w' leads to:

$$w' = -\frac{g}{N^2}D\tilde{\Theta} \tag{2.35}$$

If the atmosphere is considered to be in hydrostatic equilibrium, equation (2.30) reduces to:

$$\frac{1}{\rho_0}\frac{\partial p'}{\partial z} - g\tilde{\Theta} = 0 \tag{2.36}$$

Replacing w' in equation (2.34) with the help of equation (2.35) one gets:

$$\begin{aligned}
&\frac{g}{N^2}\Big(D\frac{\partial}{\partial z}(D\tilde{\Theta}\Big) - \frac{\partial}{\partial x}(D\tilde{\Theta})\frac{\partial U}{\partial z} - \frac{\partial}{\partial y}\Big(D\tilde{\Theta})\frac{\partial V}{\partial z}\Big) + \frac{1}{\rho_0}\nabla_h^2 p' = 0 \\
\Leftrightarrow &\frac{g}{N^2}\Big(D\Big(\frac{\partial^2\tilde{\Theta}}{\partial t\partial z} + U\frac{\partial^2\tilde{\Theta}}{\partial x\partial z} + V\frac{\partial^2\tilde{\Theta}}{\partial y\partial z}\Big)\Big) + \frac{1}{\rho_0}\nabla_h^2 p' = 0
\end{aligned}$$

Using equation (2.36) to eliminate $\tilde{\Theta}$, the equation above simplifies to:

$$\frac{1}{N^2\rho_0}D^2\frac{\partial^2 p'}{\partial z^2} + \frac{1}{\rho_0}\nabla_h^2 p' = 0 \Leftrightarrow D^2\frac{\partial^2 p'}{\partial z^2} + N^2\nabla_h^2 p' = 0$$

This equation is dependent on N, p'. The total derivative D is dependent on the horizontal wind component u. It includes no shear of the backround flow ($\frac{\partial U}{\partial z}$). However a shear of the background flow was not excluded from the beginning. If one considers a steady two–dimensional flow, it can be written as:

$$U^2\frac{\partial^2}{\partial x^2}\frac{\partial^2 p'}{\partial z^2} + N^2\frac{\partial^2 p'}{\partial x^2} = 0 \Leftrightarrow \frac{\partial^2 p'}{\partial z^2} + \frac{N^2}{U^2}p' = 0 \tag{2.37}$$

This form is now applied on a discrete $N \times M$ — grid with $z = j\Delta z, j = 0, \ldots N$ and $x = l\Delta x$, $l = 0, \ldots M$, yielding:

$$\frac{p_{j+1} - 2p_j + p_{j-1}}{\Delta z^2} + \frac{N_b^2}{U_j^2}p_j = 0$$

p_j and U_j denote pressure and mean wind at level $z = j\Delta z$. To avoid confusions with the grid indices, the buoyancy frequency is written as N_b from now on. N equations (level $0, \ldots N$) are set up with in total $N + 2$ variables $(p_0, \ldots p_{N+1})$. This was done for all M grid points. To be able to solve this system, two boundary conditions have to be introduced.

$$
\begin{array}{rcrcrcl}
p_{N+1} & + & \Big(\frac{N_b^2}{U_N^2}(\Delta z)^2 - 2\Big)p_N & + & p_{N-1} & = & 0 \\
p_N & + & \Big(\frac{N_b^2}{U_{N-1}^2}(\Delta z)^2 - 2\Big)p_{N-1} & + & p_{N-2} & = & 0 \\
 & & \cdots & & & & \\
 & & \cdots & & & & \\
 & & \cdots & & & & \\
p_2 & + & \Big(\frac{N_b^2}{U_1^2}(\Delta z)^2 - 2\Big)p_1 & + & p_0 & = & 0
\end{array} \tag{2.38}
$$

The unknown p_0 was replaced by the observed pressure at the ground. To get an expression for p_{N+1} the following approach was made. Equation (2.37) has a wave like solution of the form $p = \widehat{p}\exp(i(kx + mz))$ with a complex amplitude $\widehat{p}$ and a phase function depending on x and z with wave numbers k in the horizontal and $m = \frac{N_b}{U}$ in the vertical. If U is constant, one can make the following assumption:

$$
\begin{aligned}
\frac{\partial p}{\partial x} &= ik\widehat{p}\exp(i(kx + mz)) \\
\frac{\partial p}{\partial z} &= im\widehat{p}\exp(i(kx + mz)) \\
\Rightarrow \frac{\partial p}{\partial z} &= \frac{m}{k}\exp(i(kx + mz))
\end{aligned}
$$

Writing this in a discrete form yields an expression for p_{j+1} depending on p_j.

$$
\begin{aligned}
\frac{p_{j+1} - p_j}{\Delta z} &= im\widehat{p}\exp i(kx + j\Delta z) = imp_j \\
\Rightarrow p_{j+1} &= (im\Delta z + 1)p_j
\end{aligned}
$$

p_{N+1} in equation (2.38) can be replaced and the system can be solved.

$$
\begin{array}{ccccccccc}
 & & \Big(\frac{N_b^2}{U_N^2}(\Delta z)^2 + im\Delta z - 1\Big)p_N & + & p_{N-1} & = & 0 \\
p_N & + & \Big(\frac{N_b^2}{U_{N-1}^2}(\Delta z)^2 - 2\Big)p_{N-1} & + & p_{N-2} & = & 0 \\
 & & \cdots & & & & \\
 & & \cdots & & & & \\
 & & \cdots & & & & \\
p_2 & + & \Big(\frac{N_b^2}{U_1^2}(\Delta z)^2 - 2\Big)p_1 & + & p_0 & = & 0
\end{array}
$$

Since pressure observations at the lower boundary are used for the calculations above, the "parcel" boundary condition, which states that the air parcels have to follow the slope of the mountain, is not included. However, this condition still has to be valid. For each disturbance calculation, it is possible to calculate a height profile that satisfies the "parcel" condition. The equation is derived in the following. Under steady and two–dimensional conditions, equation (2.33) reduces to:

$$U\frac{\partial\tilde{\Theta}}{\partial x} + \frac{N^2}{g}w' = 0 \tag{2.39}$$

With the help of equation (2.36), $\tilde{\Theta}$ can be replaced in the equation above. The vertical wind perturbation w' is replaced by the "parcel" boundary condition $w = U\frac{\partial h}{\partial x}$. One yields:

$$\frac{U}{\rho_0}\frac{\partial^2 p'}{\partial x \partial z} + N^2 U\frac{\partial\tilde{h}}{\partial x} = 0 \tag{2.40}$$

This equation can be solved for $\tilde{h}$, which is the new height profile.

$$\tilde{h} = -\frac{1}{\rho_0 N^2}\frac{\partial p'}{\partial z} \tag{2.41}$$

In a discrete form, the equation above is:

$$\tilde{h}(x) = -\frac{1}{\rho_0 N^2}\frac{p_1 - p_0}{\Delta z} \tag{2.42}$$

2.5 Linear 3D Model — Wave Modes

In this chapter, a three–dimensional flow over an isolated mountain is considered. The flow is hydrostatic and incompressible. The background flow is assumed to be constant with height. The basic equations were derived in chapter 2.2. This model will be used to calculate steady state solutions of air flow over Hofsjökull. The following calculations are based on Spengler's "Gravity Waves" (2008).

$$\frac{\partial u'}{\partial t} + U\frac{\partial u'}{\partial x} + V\frac{\partial u'}{\partial y} + w'\frac{\partial U}{\partial z} + \frac{1}{\rho_0}\frac{\partial p'}{\partial x} = 0 \tag{2.43}$$

$$\frac{\partial v'}{\partial t} + U\frac{\partial v'}{\partial x} + V\frac{\partial v'}{\partial y} + w'\frac{\partial V}{\partial z} + \frac{1}{\rho_0}\frac{\partial p'}{\partial y} = 0 \tag{2.44}$$

$$\frac{\partial w'}{\partial t} + U\frac{\partial w'}{\partial x} + V\frac{\partial w'}{\partial y} + \frac{1}{\rho_0}\frac{\partial p'}{\partial z} - g\frac{\Theta'}{\Theta_0} = 0 \tag{2.45}$$

$$\frac{\partial u'}{\partial x} + \frac{\partial v'}{\partial y} + \frac{\partial w'}{\partial z} = 0 \tag{2.46}$$

$$\frac{\partial \Theta'}{\partial t} + U\frac{\partial \Theta'}{\partial x} + V\frac{\partial \Theta'}{\partial y} + w'\frac{\partial \Theta_0}{\partial z} = 0 \tag{2.47}$$

Adding the partial derivative of equation (2.43) with respect to x and the partial derivative of equation (2.44) with respect to y yields:

$$\Big(\frac{\partial}{\partial t} + U\frac{\partial}{\partial y}\Big)\Big(\frac{\partial u'}{\partial x} + \frac{\partial v'}{\partial y}\Big) + \frac{1}{\rho_0}\Big(\frac{\partial^2 p'}{\partial x^2} + \frac{\partial^2 p'}{\partial y^2}\Big) = 0$$

The first term in equation above can be simplified with equation (2.46).

$$\Big(\frac{\partial}{\partial t} + U\frac{\partial}{\partial y}\Big)\Big(-\frac{\partial w'}{\partial z}\Big) + \frac{1}{\rho_0}\Big(\frac{\partial^2 p'}{\partial x^2} + \frac{\partial^2 p'}{\partial y^2}\Big) = 0 \tag{2.48}$$

Applying the horizontal nabla operator $\nabla_h = (\frac{\partial^2}{\partial x^2} + \frac{\partial^2}{\partial y^2})$ on equation (2.45) and (2.47), one gets the following:

$$\Big(\frac{\partial}{\partial t} + U\frac{\partial}{\partial x} + V\frac{\partial}{\partial y}\Big)\Big(\frac{\partial^2 w'}{\partial x^2} + \frac{\partial^2 w'}{\partial y^2}\Big) + \frac{1}{\rho_0}\frac{\partial}{\partial z}\Big(\frac{\partial^2 p'}{\partial x^2} + \frac{\partial^2 p'}{\partial y^2}\Big) - \frac{g}{\Theta_0}\Big(\frac{\partial^2 \Theta'}{\partial x^2} + \frac{\partial^2 \Theta'}{\partial y^2}\Big) = 0$$

$$\Big(\frac{\partial}{\partial t} + U\frac{\partial}{\partial x} + V\frac{\partial}{\partial y}\Big)\Big(\frac{\partial^2 \Theta'}{\partial x^2} + \frac{\partial^2 \Theta'}{\partial y^2}\Big) + \Big(\frac{\partial^2 w'}{\partial x^2} + \frac{\partial^2 w'}{\partial y^2}\Big)\frac{\Theta_0}{\partial z} = 0$$

By use of the total derivative $(\frac{\partial}{\partial t} + U\frac{\partial}{\partial y} + V\frac{\partial}{\partial y})$, the first equation above can be transformed to replace Θ in the second one. Therefore, the second equation has to be divided by $\frac{g}{\Theta_0}$. One yields:

$$\Big(\frac{\partial}{\partial t} + U\frac{\partial}{\partial y} + V\frac{\partial}{\partial y}\Big)^2\Big(\frac{\partial^2 w'}{\partial x^2} + \frac{\partial^2 w'}{\partial y^2}\Big) + \Big(\frac{\partial}{\partial t} + U\frac{\partial}{\partial y} + V\frac{\partial}{\partial y}\Big)\Big(\frac{1}{\rho_0}\frac{\partial}{\partial z}\Big(\frac{\partial^2 p'}{\partial x^2} + \frac{\partial^2 p'}{\partial y^2}\Big)\Big) + \Big(\frac{\partial^2 w'}{\partial x^2} + \frac{\partial^2 w'}{\partial y^2}\Big)\frac{g}{\Theta_0}\frac{\partial \Theta_0}{\partial z} = 0$$

The partial derivative of equation (2.48) with respect to z provides an expression to replace the pressure terms in the last equation. The last term in the equation above can be replaced by the square of the buoyancy frequency N, as defined previously in chapter 2.3 equation (2.24).

$$\Big(\frac{\partial}{\partial t} + U\frac{\partial}{\partial y} + V\frac{\partial}{\partial y}\Big)^2\Big(\frac{\partial^2 w'}{\partial x^2} + \frac{\partial^2 w'}{\partial y^2} + \frac{\partial^2 w'}{\partial z^2}\Big) + \Big(\frac{\partial^2 w'}{\partial x^2} + \frac{\partial^2 w'}{\partial y^2}\Big)N^2 = 0$$

The flow is considered to be steady, therefore, the derivative with respect to time vanishes. Effects of rotation are neglected since the horizontal dimension of the mountain is less than 50 kilometres. The mountain is rotated into the mean wind so that only U is remaining and V disappears. The wave perturbation is assumed to remain hydrostatic. This assumption is made due to the fact that the travelling time of an air parcel over the mountain is much longer than the period of a buoyancy oscillation. The wave equation simplifies to:

$$\Big(U\frac{\partial}{\partial y}\Big)^2\Big(\frac{\partial^2 w'}{\partial x^2} + \frac{\partial^2 w'}{\partial y^2} + \frac{\partial^2 w'}{\partial z^2}\Big) + \Big(\frac{\partial^2 w'}{\partial x^2} + \frac{\partial^2 w'}{\partial y^2}\Big)N^2 = 0$$

The solution is of the form $w = \widehat{w}\exp(i(kx + ly + mz))$ with complex amplitude and the horizontal wave numbers k and l. The vertical wave number is designated by m. Applying this solution on the equation above one gets the dispersion relationship for m.

$$(Uik)^2(k^2 + l^2 + m^2) + N^2(k^2 + l^2) = 0 \tag{2.49}$$

$$\Leftrightarrow m^2 = \frac{N^2}{U^2k^2}(k^2 + l^2) - (k^2 + l^2) \tag{2.50}$$

For relatively broad mountains and under typical atmospheric conditions with $N = 0.01\frac{1}{s}$ and $U = 10\frac{m}{s}$, it is assumed that small wavelengths are

only excited minimally. The wave numbers contributing to the solution are such that $k, l \ll \frac{N}{U}$. The second term on the right side of the dispersion relationship is hence ignored, which is equivalent to assuming hydrostatic balance initially (Keller, 1994). The dispersion relationship simplifies to

$$m^2 = \frac{N^2}{U^2}\frac{k^2 + l^2}{k^2} \tag{2.51}$$

2.6 Statistics

Covariances and correlations have been calculated for the pressure perturbation field. The formulas and methods are described shortly. For further details see Storch and Zwiers (1999). The expected value of a discrete random variable X with probability function f_X and realisation x of X is given by:

$$E(X) = \sum_X x f_X(x)$$

The expected value is the average value a random variable will take when the experiment is repeated continously. The observed meteorological parameters are assumed to have a uniform distribution which means that the observed values have equal likelihood. The expected value is thus represented by the mean μ of the variable. As here, for example, for pressure at station j and sampling moment t with $t = 0, \ldots N$.

$$\mu_j = \frac{1}{N}\sum_{t=0}^{N} p_j(t)$$

The variance σ^2 of a discrete random variable X with probability function f_X is given by:

$$\sigma^2 = E((X - \mu)^2) = \sum_X (x - \mu)^2 f_X(x)$$

It is a characterization of the variables dispersion about the mean. Applied on the example given above, the variance of the pressure was calculated as follows:

$$\sigma_j^2 = \frac{1}{N}\sum_{t=0}^{N} (p_j(t) - \mu_j)^2$$

The covariance is a measure of the dependency of discrete random variables. The covariance matrix is defined by:

$$\Sigma_{\vec{X},\vec{X}} = E((\vec{X} - \vec{\mu})(\vec{X} - \vec{\mu})^T)$$

The (i, j) – element of Σ can be expressed as:

$$\sigma_{i,j} = E((x_i - \mu_i)(x_j - \mu_j))$$

If the deviations from the mean of two random variables tend to have the same sign, the covariance between these variables is positive. Negative variances occur for deviations from the mean with opposite sign. The covariance is not scale invariant. To avoid possible difficulties due to scaling, the correlation can be calculated, which is defined by:

$$\rho_{i,j} = \frac{\sigma_{i,j}}{\sqrt{\sigma_i^2 \sigma_j^2}}$$

where $\sigma_{i,j}$ is the covariance and σ_i^2 respectively σ_j^2 are the variances. The correlation always takes values between -1 and 1 and is an indication of the linear relationship between two random variables

Chapter 3

Placement and Instrumentation

3.1 Hofsjökull

Hofsjökull is the third largest glacier in Iceland. It is located in the centre of Iceland. The shape of Hofsjökull is almost round with a diametre of 35 to 40 kilometres. The summit of Hofsjökull is at about 1770 metres above sea level. The height relative to the surrounding areas is approximately 1000 metres. The mountain has a second summit on the north eastern side called Miklafjell with a height of 1468 metres. Since the mountain is covered by ice and snow, its surface is very smooth. To the south west of Hofsjökull is Kerlingarfjöll with a height of 1488 metres. Further south and in the north are large gravel fields without any higher mountains. To the east of Hofsjökull lies Vatnajökull, approximately 30 kilometres distant, to the west lies Langjökull about the same distance away. Therefore, Hofsjökull can be regarded as a fairly isolated mountain.

The Rossby number R, calculated by $R = \frac{U}{f_0 L}$, with U the mean wind speed, f_0 the Coriolis parameter and L the dimension of the obstacle, gives an idea of the influence of the earth's rotation on the flow. For Hofsjökull it is about 2, thus effects of rotation can be neglected. The Froude number $F = \frac{Nh}{U}$, with N the buoyancy frequency and h the vertical extent of the obstacle, ranges from 0.5 to high values. Blocked and unblocked flows are possible.

3.2 Autonomous Weather Stations

For measuring basic meteorological parameters, autonomous weather stations were in use. 18 autonomous weather stations have been placed over and around Hofsjökull. Thereby two stations of the Swiss Federal Institute of

Technology Zurich (ETH), twelve stations of the Geophysical Institute in Bergen (GFI) and five stations of the Meteorological Institute in Munich (MIM) where installed.

3.2.1 Placement

For the placement of the stations, several aspects had to be considered. Since the region of Hofsjökull is very remote, the accessibility of the stations was a major problem. Crevasses cut off some places on the glacier, so that the recovery of the stations after the period of measurements was not guaranteed. Similar problems applied for the stations on ground around Hofsjökull. Fast changing melt water rivers could only be crossed by car or not at all. As the stations had to be checked at least once after their installation, most of them could not be placed at too remote locations. In addition, the sampling rate of the stations had influence on the placement. The storing units of the stations had to be changed regularly depending on the sampling rate. The MIM stations, for example, had to be checked every eleven days. The placement of the stations can be seen in figure 3.1. Five stations had been placed close to the northern edge of the glacier (N1 – N5) from west to east, and three additional north of N3 in a south to north axis. On the glacier, one big north to south axis was over the summit of Hofsjökull (HN10 - HS15) and one smaller axis was expanding from HN16 over a plateau eastwards to HE15 on Miklafjell. Four stations had been placed at the south of the glacier (S1 - S4). Table 3.1 gives an overview of the coordinates and altitude, table 3.2 an overview of the site of the stations.

3.2.2 Sensors

The measured parameters were temperature, relative humidity, atmospheric pressure, wind direction and speed, as well as precipitation. Stations without pressure sensor were additionally equipped with an *Opus 10 TPR* autonomous pressure sensor. Table 3.3 shows the instrumentation of all the stations in detail.

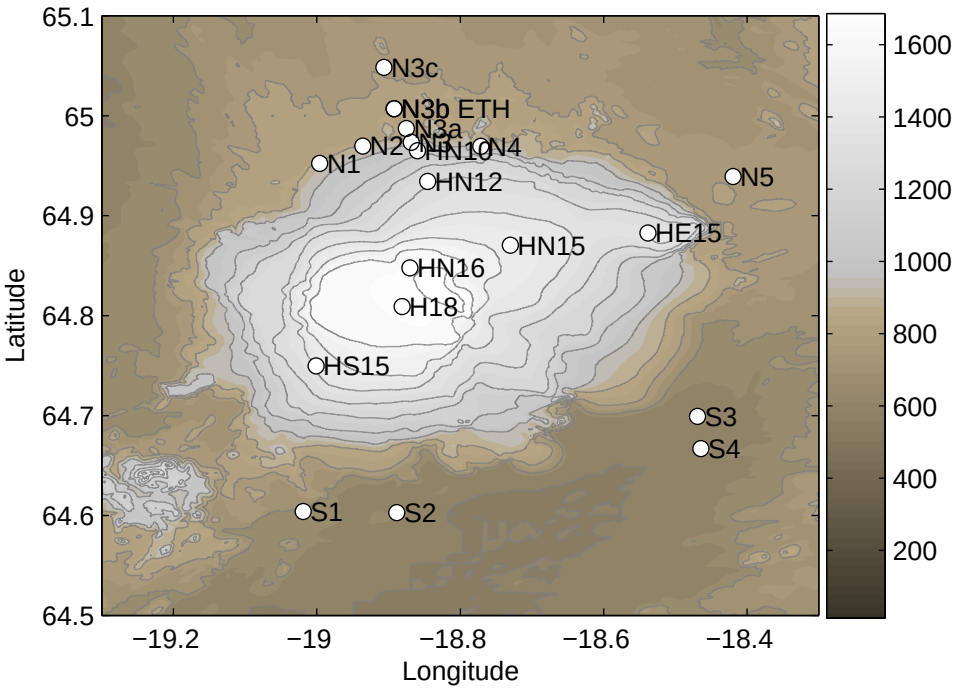

Figure 3.1: Map of Hofsjökull with positions of the automatic weather stations. The topography is based on data from the 2000 Shuttle Radar Topography Mission. Pay attention that the scales of the x and y–axis differ slightly.

station	latitude [$^\circ N$]	longitude [$^\circ W$]	altitude [m]
N1	64.95242	18.99595	845
N2	64.96977	18.93593	894
N3	64.97350	18.86832	880
N3a	64.98727	18.87507	865
N3b	65.00700	18.89228	845
N3c	65.04848	18.90638	809
N4	64.96957	18.77147	954
N5	64.93917	18.41943	807
HN10	64.96497	18.85978	996
HN12	64.93432	18.84538	1175
HN15	64.87057	18.73022	1497
HE15	64.88268	18.53813	1458
HN16	64.84782	18.87028	1603
H18	64.80902	18.88107	1777
HS15	64.74975	19.00107	1486
S1	64.60400	19.01900	695
S2	64.60288	18.88838	636
S3	64.69933	18.46895	629
S4	64.66692	18.46430	620

Table 3.1: Identification, position and altitude of the automatic weather stations.

station	description of site	institute
N1	Gravel field 300 m from the edge of the glacier	GFI
N2	Top of small gravel ridge 300 m from the edge of the glacier	GFI
N3	Gravel field 30 m from the edge of the glacier	ETH
N3a	Lava field 2 km from the edge of the glacier	MIM
N3b	Lava field with sparse vegetation about 4 km from the edge of the glacier	ETH
N3c	Gravel field 10 km from the edge of the glacier	MIM
N4	Top of a gravel moraine 500 m from the edge of the glacier	GFI
N5	Gravel field 7 km from the edge of the glacier	GFI
HN10	Northward sloping area of the glacier	GFI
HN12	Snow field in a small depression	MIM
HN15	Plateau north-east of the summit with snow surface	MIM
HE15	Summit of Miklafjell at the eastern ridge of the glacier	GFI
HN16	Northward facing slope north of the summit with snow surface	MIM
H18	Plateau at the summit of the glacier with snow surface	GFI
HS15	Southward facing slope south-west of the summit with snow surface	GFI
S1		OPUS
S2		GFI
S3		GFI
S4		GFI

Table 3.2: Identification, site and institute of the automatic weather stations.

station	T	rH	Wdir	Wspd	Wgst	pres	precip
N1	√	√	√	√	√	√ *(OPUS)*	√
N2	√		√	√		√	√
N3	√	√	√	√		√	√
N3a	√	√	√	√		√	√
N3b	√	√	√	√		√	√
N3c	√	√	√	√		√	√
N4	√	√	√	√	√	√ *(OPUS)*	√
N5	√	√	√	√		√	√
HN10	√	√	√	√		√ *(OPUS)*	√
HN12	√	√	√	√		√	√
HN15	√	√	√	√		√ *(OPUS)*	√
HE15	√		√	√		√ *(OPUS)*	√
HN16	√	√	√	√		√	√
H18	√	√	√	√		√	√
HS15	√	√	√	√		√	√
S1						√ *(OPUS)*	√
S2	√	√	√	√		√ *(OPUS)*	√
S3	√	√	√	√		√ *(OPUS)*	√
S4	√		√	√		√	√

Table 3.3: Intstrumentation of the automatic weather stations. T: Temperature, rH: relative Humidity, Wdir: Wind direction, Wspd: Wind speed, Wgst: Wind gust, pres: Pressure, precip: Precipitation.

Specification GFI–stations: The GFI–stations used the *AANDERAA air pressure sensor 2810*. The measurements are done by a thin membrane that is exposed to atmospheric pressure on one side and to a vacuum on the other. The membrane is furnished with 4 diffused resistors that form a Wheatstone bridge. The output signal is proportional to the atmospheric pressure (*AANDERAA*, 2006). During the measurements, the sensor was placed in a metal box that was attached to the pole of the weather station to protect it from precipitation.

For air temperature measurements, the GFI–stations used the *AANDERAA air temperature sensor 3455*. This sensor is based on the ohmic half-bridge principle and employs a 2000 Ohm film–type platinum resistor as the sensing element. The sensors were covered by radiation screens that hinders heating by direct sunshine (*AANDERAA*, 2006).

The GFI–stations measured relative humidity by the *AANDERAA relative humidity sensor 3445*. These sensors were covered by a radiation and precipitation screen, as well. The sensors employed a capacitive polymer for humidity sensing (*AANDERAA*, 2003).

Wind direction was measured with *AANDERAA wind direction sensor 3590*. These sensors consists of a light wind vane pivoted on top of a housing. A compass is magnetically coupled to the vane inside the housing. The direction is measured every second and averaged when read out (*AANDERAA*, 2006).

For wind speed measurements, the *AANDERAA wind speed sensors 2740* were used. These sensors consist of a three cup rotor on top of an aluminum housing. The rotor is furnished with a magnet. The rotation of the magnet is sensed by a magneto inductive switch located inside the housing. The arithmetic mean of the wind speed is read out (*AANDERAA*, 2006).

Table 3.4 shows details for all the sensors.

Specification ETH–stations: The ETH-stations used two different pressure sensors. The *VAISALA PTB 100 analogue barometer* and the *DRUCK RPT 410 barometric pressure sensor*. The *VAISALA PTB 100* consist of a silicon diaphragm that bends when the pressure changes. Thereby, the height of the vacuum gap in the sensor is changed as well as the capacitance of the sensor, which is measured and converted into a pressure reading (*VAISALA*, 2007).

Temperature was measured by the *CAMPBELL 107 temperature probe* which consists of a thermistor encapsulated in an epoxy-filled aluminum housing (*CAMPBELL*, 2007).

For relative humidity measurements, the ETH-stations used the *VAISALA*

AANDERAA	
Air pressure sensor 2810	
Measuring Range:	920 to 1080 hPa
Accuracy:	0.2 hPa
Resolution:	0.2 hPa
Operation Temp. Range:	-40 to +47 °C
AANDERAA	
Air temperature Sensor 3455	
Measuring Range:	-43 to +48 °C
Accuracy:	0.1% of range
Resolution:	0.1% of range
AANDERAA	
Relative humidity sensor 3445	
Measuring Range:	0 to 100% relative humidity (RH)
Accuracy:	2% (RH)
Resolution:	0.1%
Operation Temp. Range:	-40 to +50 °C
AANDERAA	
Wind direction sensor 3590	
Measuring Range:	0 to 360 degrees Magnetic
Threshold Speed:	Less than 0.3 m/s
Accuracy:	Better than 5 degrees Magnetic
Operation Temp. Range:	-40 to +50 °C
AANDERAA	
Wind speed sensor 2740	
Measuring Range:	Up to 79 m/s
Threshold Speed:	Less than 0.3 m/s
Accuracy:	2% or 0.2 m/s, whichever is the greater

Table 3.4: GFI-stations specifications

HMP 45 relative humidity probe. These probes work by a thin polymer film, that either absorbs or releases water vapour as the relative humidity of the ambient air rises or drops. The dielectric properties of the polymer depend on the amount of water contained in it. The instrument measures the capacitance of the sensor and converts it into a humidity reading (*www.vaisala.com*).

Wind direction and speed was measured with the *VAISALA WINDCAP Ultrasonic Wind Sensor WMT50*. The ultrasonic wind sensor measured the transit time, which is the time it takes for the ultrasound to travel from

one transducer to another depending on the wind speed along the ultrasonic path. This was done at three different paths orientated in a triangle. From these paths the wind direction and speed is calculated (*www.vaisala.com*).

Table 3.5 shows detail for all the sensors.

Vaisala	
PTB100 pressure sensor	
Measuring Range:	600 to 1060 hPa
Accuracy:	0.5 to 2 hPa
Operation Temp. Range:	-40 to +60 °C
Druck	
RPT 410 pressure sensor	
Measuring Range:	600 to 1100 hPa
Accuracy:	0.5 to 2 hPa
Resolution:	0.01 hPa
Operation Temp. Range:	-40 to +60 °C (-40 to 140 °F)
Campbell	
107 temperature sensor	
Measuring Range:	-35 to +50 °C
Accuracy:	$<$ 0.2 to 0.4 °C
Vaisala	
HMP45 humidity sensor	
Measuring Range:	0.8 to 100% relative humidity (RH)
Accuracy:	2% to 3% RH
Vaisala	
WMT50 wind speed	
Measuring Range:	0 to 60 m/s
Accuracy:	0.3 m/s or 3% to 5%, whichever is greater
Vaisala	
WMT50 wind direction	
Measuring Range:	0 to 360 degrees Magnetic
Accuracy:	3 degrees Magnetic
Resolution:	1 degree Magnetic

Table 3.5: ETH-stations specifications

Specification MIM–stations: The MIM-stations use the *VAISALA DPA21 Pressure Transducer* for pressure sensing. The working principle is similar to that of the *VAISALA PTB 100* mentioned above, but it consists of three transducer units. The output signal is the mean of all three units.

Temperature and relative humidity was measured with a combined temperature-humidity sensor from *FISCHER*. The temperature sensor consisted of a *PT100* resistor. Relative humidity was sensed via a capacitive sensor. Both sensors were covered by a ventilated housing to protect them from direct radiation and weather.

For wind speed measurements, the MIM-stations used a cup vane anemometer. Wind direction was measured via a wind vane.

Table 3.6 shows detail for all the sensors.

Station N1: Station N1 was situated on a gravel field approximately 300 metres from the edge of the glacier. The station recorded from 24 July to 23 August 2007 without any defects. An *OPUS 10* pressure sensor was placed at the station.

Station N2: Station N2 was positioned on top of a small gravel ridge 300 metres from the edge of the glacier. The station recorded from 26 July to 22 August 2007. The wind direction sensor was changed on 9 August 2007. The measured wind direction was constant before. After replacing the sensor, the measured values were changing reasonable. From 2 August, 6:03 to 7:21 LT the wind speed dropped to 0 m/s instantaneously. During the period from 15 August, 4:31 - 8:15 LT, wind direction kept constant and from 7:27 to 9:15 LT wind speed was 0 m/s.

Station N3: Station N3 was positioned on a gravel field 30 metres from the edge of the glacier. The station recorded from 22 July to 22 August 2007. On 2 August the temperature and relative humidity sensors were removed to be tested at station N3b. They did not record any data the days before. It was tried to fix the station with a new software upload, but the sensors kept defect for the rest of the campaign. Pressure, wind direction and wind speed were still sensed without problems. In the period from 10 August, 10:12 LT to 12 August, 18:34 LT the station did not record any data.

Station N3a: Station N3a was situated on a lava field 2 km from the edge of the glacier. Some problems with the settings of the station caused a data loss in the period from 24 July to 27 July 27 2007. From then on the station recorded correctly until 22 August.

Station N3b: Station N3b was positioned on a lava field with sparse vegetation near Ingolfsskali cottage. The station recorded from 22 July to 22 August, 2007 without any problems.

Vaisala	
DPA21 pressure sensor	
Measuring Range:	500 to 1050 hPa
Accuracy:	0.3 hPa -range 800 to 1050 hPa -temperature 5 to 55 °C
	0.5 hPa -range 500 to 1050 hPa -temperature -40 to 55 °C
Resolution:	0.1 hPa
Operation Temp. Range:	-40 to +70 °C
Fischer	
T/F temperature sensor	
Measuring Range:	-30 to 70 °C
Accuracy:	0.1 °K + 0.0017 x $\|t\|$ t = measured temperature in °C
Fischer	
T/F humidity sensor	
Measuring Range:	0 to 100% relative humidity (RH)
Accuracy:	$<$ 2% RH
LISA	
wind speed sensor	
Measuring Range:	0 to 60 m/s
Accuracy:	1% of measuring range
Operation Temp. Range:	-35 to +70 °C
RITA	
Gray wind direction sensor	
Measuring Range:	1 to 360 degrees Magnetic
Accuracy:	2 degrees Magnetic
Resolution:	1.4 degrees Magnetic
Operation Temp. Range:	-30 to 70 °C

Table 3.6: MIM-stations specifications

Station N3c: Station N3c was placed on a gravel field 10 km from the edge of the glacier. The station was installed on 27 July and ran till 22 August 2007, but had some problems. The data from 28 July to 3 August 2007 and 6 August to 10 August 2007 was lost. These defects might have been caused by an incorrect channel assignment.

Station N4: Station N4 was situated on top of a gravel moraine 500 m from the edge of the glacier. The station recorded from 24 July to 21 August 2007 without any problems.

Station N5: Station N5 was placed on a gravel field approximately 7 km from the edge of the glacier in the north-east of Hofsjökull. The station recorded from 28 July to 23 August 2007. There are two incidents of wind speed indicating 0 m/s for some hours at 6 August and 15 August. The temperature was above zero degrees during that time so that icing can be excluded.

Station HN10: Station HN10 was situated in the sloping area on the north side of the glacier. The station recorded from 26 July to 20 August 2007. Due to ice melting, the pole of the station tilted and rotated, which lead to incorrect wind direction and wind speed readings. Attempts were made to stabilize the pole via azimuthal fixations, but the problem could not be fixed in total. Within a first check of the station at 30 July, the north–marker of the wind direction vane was pointing towards 110 degrees relative to magnetic north (measured with a GPS). The second check of the station was on 2 August. The north direction of the wind sensor was pointing towards 40 degrees relative to magnetic north. The last check of the station was on 10 August. The north direction of the wind direction sensor was pointing towards 10 degrees relative to magnetic north. The wind speed dropped instantaneously to 0 m/s for some hours at the following dates: 28 July, 2 August and 13 August. Incidents of constant wind direction occurred on: 27 July, 28 July, 13 August, 15 August and 16 August. These problems were probably caused by icing.

Station HN12: Station HN12 was positioned on a snow field in a small depression of the ablation area. The station was installed 23 July 2007, but lost their settings and was not able to record any data until 2 August 2007. Because of the melting snow surface, the station was found tilted within the first check at 25 July 2007 and was erected again. Wind direction showed constant values of about 300 degrees and temperature showed minus degrees

and large fluctuations. Due to snow melting and high wind speeds, the station crashed into the snow sometime between 2 August and 10 August. It was erected again during a check 10 August. From this point of time, wind direction and temperature could not be sensed any longer because of defect sensors. All other sensors were working normal.

Station HN15: Station HN15 was situated on a plateau in the accumulation area. The station recorded from 25 July to 20 August 2007. Only temperature was sensed wrong for some 40 minutes on 25 July. Zero wind speed occurred on: 1 August to 2 August, 4 and 5 August, as well as 12 August and from 14 August to 15 August.

Station HE15: Station HE15 was positioned on the summit of Miklafjell at the eastern ridge of the glacier. The station recorded from 25 July to 20 August 2007. The station suffered a lot from icing. Large periods of zero wind speed and constant wind direction can be found from 26 July to 6 August. From then on, the station kept sensing without problems until 12 August. In the time from 12 August to 20 August, incidents of icing can be found once again.

Station HN16: Station HN16 was situated on a northward facing slope in the accumulation area of the glacier. The station was erected 22 July, 2007 but did not record any data before 28 July. From then on, the station kept working until 19 August 2007. The relative humidity measurements show very low values from 9 August to the end of the campaign. Probably caused by an ice crust on the sensor. There are some smaller periods of zero wind speed on 1 August, 4 and 5 August. And a long period from 12 August to 16 August, to a high probability caused by icing.

Station H18: Station H18 was positioned on a plateau on the summit of the glacier. The station recorded from 26 July to 20 August 2007. During a check at 2 July, the station was found with partly ice covered mast and sensors. The station was influenced by icing over the whole measurement period. This caused lack of data during the periods from 31 July to 2 August, 3 August to 7 August and 11 August to 16 August. On 27 July, 29 July, 18 August, 19 August and 20 August wind direction and wind speed could not be sensed for some hours.

Station HS15: Station HS15 was positioned on a southward facing slope in the accumulation area. The station recorded from 26 July to 20 August

2007. The station worked without problems. Only two incidents of icing occurred on 28 July and 19 August with zero wind speed and constant wind direction for some hours.

Station S1: Station S1 was equipped only with an *OPUS* pressure sensor and worked without any major problems.

Stations S2, S3, S4: Station S2, S3 and S4 were placed in the south and south east of Hofsjkull. The stations recorded from 26 July to 22 August 2007 (S2), respectively 25 July to 23 August 2007 (S3/S4). These stations could not be checked due to their remote placement but seemed to work without any problems. For the same reason, the sampling interval was set to 5 minutes unlike all other stations, which had a 2 minutes sampling interval.

3.3 Vertical Soundings

The following systems were used to gain information on the vertical wind, relative humidity and temperature profiles.

- Theodolites for wind velocity and wind direction soundings with helium balloons.
- Remotely controlled model aircraft's *(KALI)* for measurements of temperature and relative humidity profiles.

3.3.1 Wind Profile Measurements via Balloon Soundings

Helium filled balloons were used for the measurements of the vertical wind profiles. The balloons were tracked optically with two modified theodolites. Every ten seconds, azimuth and elevation of the balloon were sensed simultaneously at both theodolites. With the help of these four angles, and with the knowledge of the length and orientation of the basis between the theodolites, the position of the balloon could be calculated for every sampling moment. The velocity vector and, of course, the horizontal wind velocity and direction was determined with the help of the position changes and the time interval between the samples (Mayer, 2005).

The velocity vector was calculated by the difference quotient of the position vectors $\vec{P}$.

$$\vec{v}(t + \frac{\Delta t}{2}) = \frac{\vec{P}(t + \Delta t) - \vec{P}(t)}{\Delta t}$$

and time interval $\Delta t = 10sec$. The horizontal wind velocity was then calculated by:

$$v_h = \sqrt{u^2 + v^2}$$

with u and v the horizontal components of the wind vector. The wind direction was determined by:

$$dd = \frac{180^\circ}{\pi} \arctan\left(\frac{-v}{u}\right) = \frac{180^\circ}{\pi} \arctan\left(\frac{v}{u}\right) + 180^\circ$$

Thereby, the signs of u and v had to be considered to gain angles between 0 and 360° (Schween, 1998).

The basis was to the north–west of Ingolfsskali cottage (station N3b) in the north of Hofsjökull. It had a south–east to north–west orientation of 320 degrees magnetic north and a length of approximately 1600 metres. Theodolite 1 was situated in a lava field near Ingolfsskali cottage. Theodolite 2 was placed on an airfield with plain gravel ground. The balloon start was on a small hill between the two theodolites. The orientation and length of the basis was determined by triangulation procedures with the two theodolites. These procedures are described in detail by Schween (1998). Unfortunately it was not possible to install a second basis in the south of the mountain.

3.3.2 Temperature and Relative Humidity Soundings via *KALI*

The remotely controlled model plane *KALI* was used for vertical temperature and relative humidity soundings. The planes were used before in field campaigns in Bolivia (Mayer, 2005) or the Kali Gandaki valley in Nepal, as well as in the *AllgEx* campaign 2005 (Ablinger, 2006). The system consists of an electrical driven soaring plane, two sensors for relative humidity and temperature, one sensor for pressure and a data logger. The relative humidity and temperature sensors were attached to the lower side of the wings near the aircraft body. The logger and pressure sensor were placed inside the aircraft.

The sensors were developed by the engineering office *D. Würtenberger*. All sensors needed to be calibrated with individual calibration factors. Two logger setups were in use. Since new sensors were ordered shortly before the campaign, no calibration could be done for them. These sensors were driven

in combination with calibrated sensors so that a new sensor was always in simultaneous use with an already calibrated sensor. For the new sensor, the same calibration factors were used as for the already calibrated sensor. The measured values of these sensor combination showed a good correlation.

The pressure sensor was used for the determination of height above ground. The sensor had a resolution of about 1 hPa, which gives a height resolution of approximately 8 metres. The resolution of the temperature sensors was approximately 0.2° Kelvin within a measuring range from -20 to +30 °C. The relative humidity sensors had a measuring range from 0 to 100% and the accuracy was stated to be 2%. The resolution was about 0.6%. For more details about the calibration of the sensors and the *KALI* system see Mayer (2005) and Ablinger (2006).

The *KALI* flights took some 30 minutes in generall and were started in combination with the balloon launches. Since both soundings relied on optical tracking, they could only be conducted during fair weather conditions.

3.4 Pressure Data Processing

The synoptic situation had of course large impact on the observed pressure values. To be able to lay focus on the small scale activities around Hofsjökull, the pressure data needed to be filtered from synoptic influence. Due to the fact that all the stations were positioned on different heights, the pressure data needed to be reduced to a basic level as well. The weather stations differed in the sampling interval. Stations equipped with *OPUS* pressure sensors measured pressure with a sampling interval of one minute compared to the two minute sampling interval of the stations with other pressure sensors. Stations in the south of Hofsjökull had a sampling interval of five minutes because of the remote placement. The whole dataset was brought to an one minute resolution via linear interpolation. Because most of the stations were placed higher than 800 meters above sea level, pressure was not reduced to sea level. Instead the arithmetic mean of the whole observation period was subtracted from each sampling moment for each station.

$$p_0(i,t) = p(i,t) - \frac{1}{N}\sum_{t=1}^{N} p(i,t)$$

$p(i,t)$ is pressure at time t and station i. To clear the observations from synoptic influence the spacial mean, the arithmetic mean of all stations at a certain point of time, was subtracted from each sampling moment.

$$p_0'(i,t) = p_0(i,t) - \frac{1}{M}\sum_{i=1}^{M} p_0(i,t)$$

Through this pressure observations were reduced to pressure disturbance observations.

Chapter 4

Results

4.1 Synoptic Situation

The large scale weather situation during the *FLOHOF*-campaign was dominated by several low pressure systems, which passed Iceland in the south.

A low pressure system was developing south of Greenland 22 July, moving eastwards and passing Iceland in the south 25 July to 26 July. Thereby, it left Iceland under the influence of easterly to north-easterly winds. Cold and wet air masses reached Iceland on the back side of the low pressure system. From then to 30 July pressure gradients were weak leading to calm north-easterly winds.

During 30 July, another low pressure system developed over southern Greenland, intensified and passed Iceland in the time from 31 July to 2 August. Within that time, winds intensified as well turning from west to south. This system brought warm and wet air with it from the south. On the backside of the system, winds turned to north-east again.

A second intense low pressure system evolved south of Greenland. This pressures system passed Iceland in the south 3 August to 4 August and joined the leading system east of Iceland. Wet and cold air from the north reached Iceland on the backside of this large pressure system. For the next days, the system kept position and weakened.

7 August, another low pressure system developed south of Greenland. Winds turned again to south-west. This system passed Iceland 8 August to 9 August in the south, but lost much of its intensity. On the forefront of the system, warm and wet air masses could reach the island. The system remained south-east of Iceland leading to north-easterly winds bringing once again cold air from the north.

In the period from 14 August to 16 August, the system intensified again

and moved over Great Britain and Scandinavia to the north-east. Iceland was still on the backside of the system, cold and relatively dry air could reach the island with north-westerly to north-easterly winds.

A further low pressure system passed Iceland far south 17 August to 19 August leading to weak south-westerly winds. From 20 August, a high pressure system over the northern Atlantic gained influence on Iceland. Winds were intensifying and with a clear southerly component.

The figures 4.1 to 4.4 show the reanalysis of the NCEP (www.wetterzentrale.de). The dates were choosen to match the periods described in section 4.4.

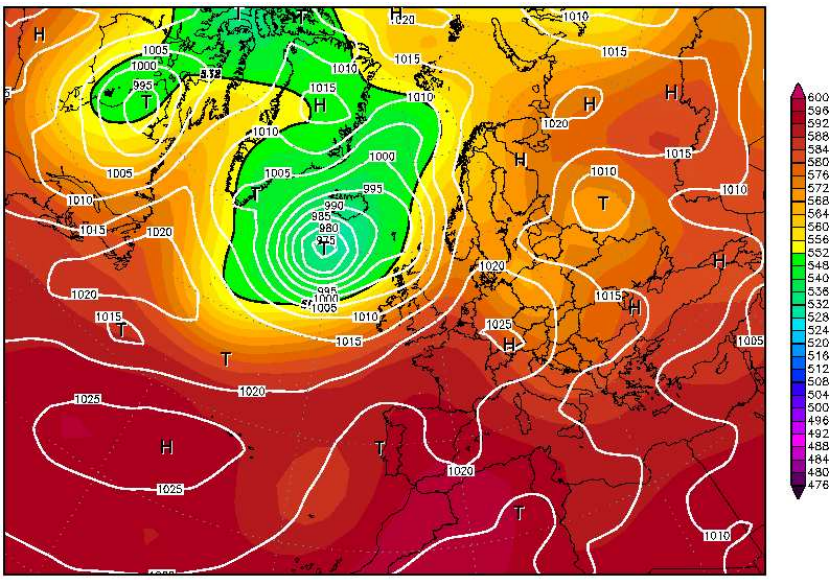

Figure 4.1: Reanalysis of the NCEP (www.wetterzentrale.de). The plot shows the 500 hPa geopotential (gpdm) and surface pressure (hPa) from 4 August 2007, 00 UTC.

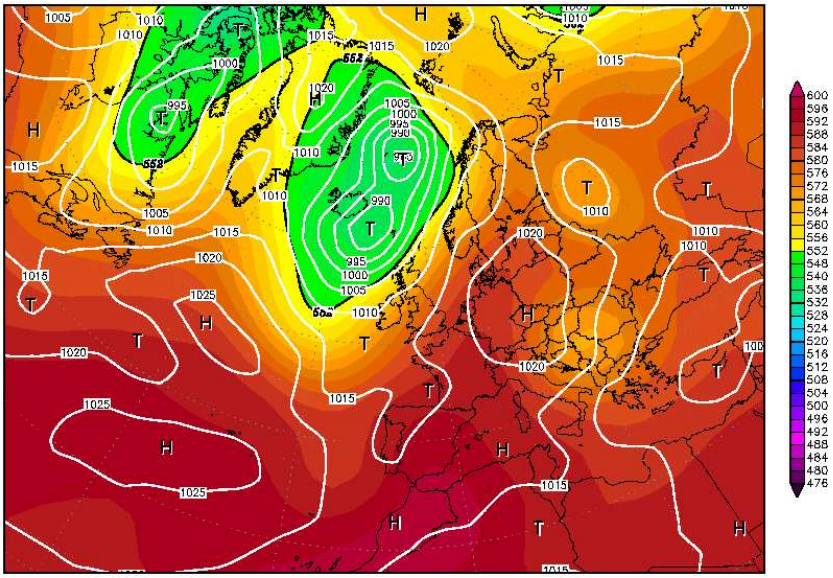

Figure 4.2: Reanalysis of the NCEP (www.wetterzentrale.de). The plot shows the 500 hPa geopotential (gpdm) and surface pressure (hPa) from 5 August 2007, 00 UTC.

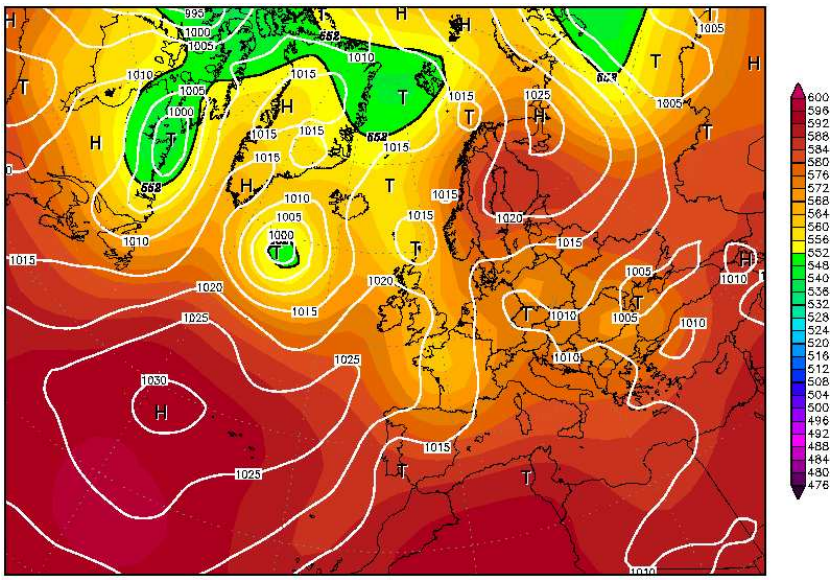

Figure 4.3: Reanalysis of the NCEP (www.wetterzentrale.de). The plot shows the 500 hPa geopotential (gpdm) and surface pressure (hPa) from 8 August 2007, 00 UTC.

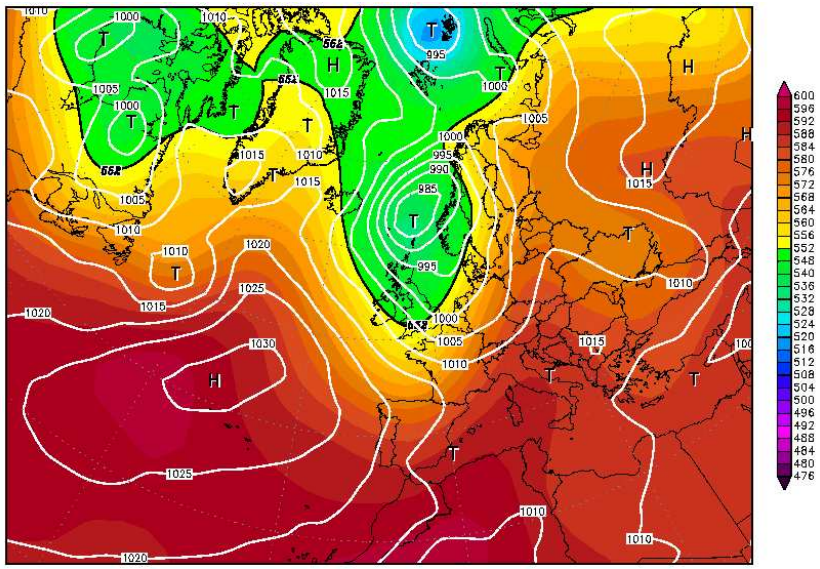

Figure 4.4: Reanalysis of the NCEP (www.wetterzentrale.de). The plot shows the 500 hPa geopotential (gpdm) and surface pressure (hPa) from 16 August 2007, 00 UTC.

4.2 Automatic Weather Stations – Observed Parameters

Pressure: The pressure was at a local minimum at 26 July. The highest station, H18 on 1777 m above sea level, measured an absolute pressure of 810 hPa. The observed pressure at the lowest station, S4 on 620 m above sea level, was 125 hPa higher with a value of 935 hPa. The pressure rose for approximately 10 hPa during the next four days and reached a maximum on 29 August. It followed a drop of about 20 hPa during the next two days. Pressure climbed again for some 10 hPa until on 2 August and dropped for approximately 15 hPa to its minimum during the campaign on 4 August. It followed a raise of about 25 hPa. From then on, pressure kept relatively constant for the next five days. A weak drop of about 5 to 10 hPa took place from 11 August to 19 August. After that, the pressure rose again for some 20 hPa the last days of the campaign.

Wind direction: The wind directions were around east during the beginning of the campaign from 24 July to 29 July. They changed to south-west the night from 28 July to 29 July. In the following period to 2 August, the winds turned cyclonic to northerlies. After that, they changed to easterlies again for the next two days. A cyclonic turn to southerly winds followed from 4 August to 5 August. The stations in the south (S2 S4) changed more or less instantaneously to southerly winds on 5 August. The dominating direction was south in the time from 6 August to 10 August. After that, northerly to north-easterly winds prevailed until 16 August. Most of the stations turned anticyclonic to south-westerly wind directions during the following two days. This continuously turn could not be observed at the southerly stations. They changed once again directly to south-westerly winds. The south-westerly directions did last until the end of the campaign.

Wind speed: Wind speeds were about 5 m/s most of the time. Some stations observed an increase in the time from 30 July to 6 August. Especially the stations in the south S2 to S4 and HS15 measured up to 20 m/s. The stations N1, N2 and N4 showed a similar structure in the north. The N3 stations however observed more constant wind speeds. The stations on the mountain suffered a lot from icing, these were the stations H18, HN16, HN15 and HE15. Unfortunately, no wind speed measurements are available at the summit stations H18 and HE15 during that time. The stations HN16 and HN15 show only a slight increase to about 10 m/s. It is not known, if these observations are reliable. A second period of increased wind speeds took

place from 12 August to 17 August. This increase is once again strongest for the southern stations and HS15.

Temperature: The measured temperature at the stations in the south and in the north show a clear diurnal cycle with an amplitude of 5 to 10 °C. The mean temperature was about 7 °C in the south in the period from 26 July to 6 August. The stations in the north showed temperatures between 2 and 5 °C in the same period. Mean temperatures rose in the time from 6 August to 12 August with about 10 °C in the south and 7 °C in the north. They fell again for about 5 °C and showed a slight increase to the end of the campaign. The stations on the mountain observed more constant temperatures. The summit station H18 for example showed temperatures of 0 to -4 °C most of the time. In the warm period from 6 August to 12 August, the mean temperature rose to 1 °C. The other stations on the glacier measured a similar behaviour, albeit with higher temperatures depending on the altitude of the station.

Relative humidity: The relative humidity at the southern stations S2 and S3 varied around 75%, as well with a diurnal cycle. The minimum was hereby in the afternoon, the maximum in the morning. The amplitude of this variation was about 20 to 50%. The stations on the glacier showed a very high relative humidity of or near 100% over the whole campaign. The stations in the north observed as well a diurnal cycle with high values of near 100% in the morning and values of 75 to 50% in the afternoon. In the period from 6 August to 11 August, a drop to values of 50 to 80% was measured at the northern stations.

Pressure disturbance: The absolute pressure observations were reduced to pressure perturbations to get a detailed view of the small scale pressure situation around Hofsjökull. The details of this reduction can be seen in chapter 3.4.

The perturbations were between -2 and 2 hPa in general. They showed an opposite behaviour on the northern and southern side of the mountain, depending on the wind direction. Periods of north-easterly winds were accompanied by negative perturbations in the south and positive perturbations in the north. Three occurrences of that kind could be observed in the time from 31 July to 2 August, 3 August to 5 August and 14 August to 17 August. The mountain stations showed large positive perturbations of 1 to 2 hPa during the first two periods, but different ones during the time from 14 August to 17 August. The summit stations H18 and HE15 followed the southern

stations and show as well negative perturbations down to -2 hPa, whereas the stations HN16, HN15 and HN12 showed only weak values around zero.

The period of southerly winds from 7 August to 11 August showed a positive perturbation at the stations HS15, H18 and HE15. The values at the southern stations were only weak positive. A negative perturbation could be observed at the northern stations.

Plots of the observations of the automatic weather stations and of the pressure perturbation during the campaign can be seen in the Appendix, chapter A.

4.3 Covariance and Correlation of Pressure Disturbance

Figure 4.5 shows a plot of the covariances of the pressure perturbations. The calculation of the perturbation is described in the chapter 3.4.

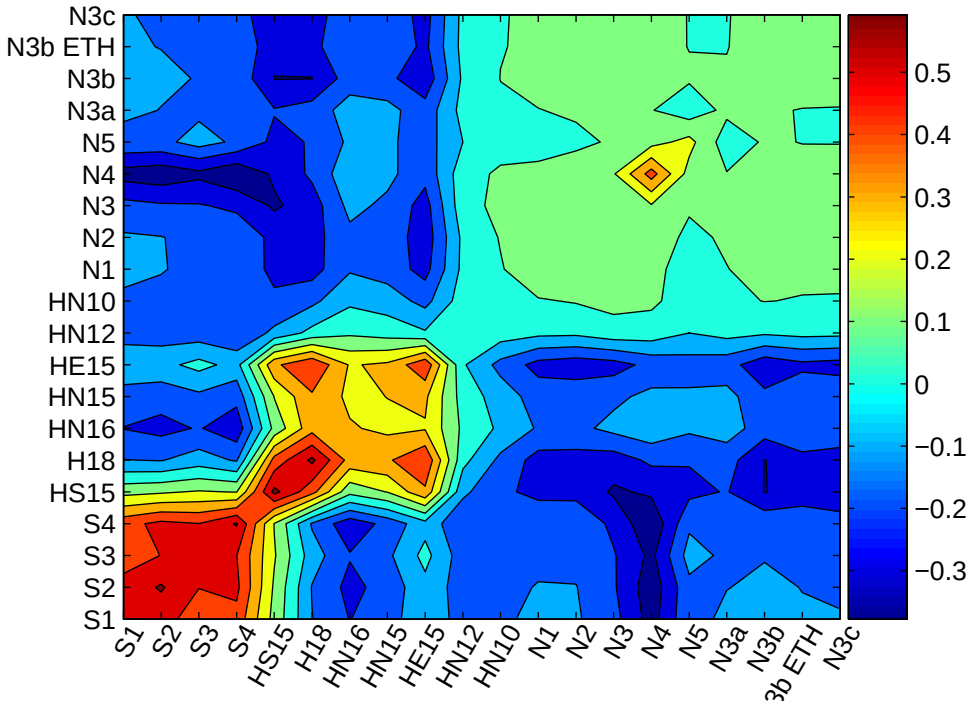

Figure 4.5: Pressure perturbation covariance in $(\text{hPa})^2$.

The four southern stations (S1 to S4) and the mountain stations HS15 and H18 show the highest variances of about $0.5(\text{hPa})^2$. These stations are

followed by the mountain stations HN16, HN15 and HE15, as well as N4, with variances of 0.2 to 0.4$(\text{hPa})^2$. The northern stations, beginning from HN12, show variances of about 0.1$(\text{hPa})^2$. The covariances of the four southerly stations are relatively uniform and the highest ones with about 0.5$(\text{hPa})^2$. The mountain stations are positive correlated too, but do not have that uniform structure. The highest correlation of these stations can be seen between station HS15, H18 and HE15 with about 0.5$(\text{hPa})^2$, which may arise from a higher wave activity over the southern parts of the mountain and the fact that H18 as well as the Miklafjell station HE15 are summit stations. The northern stations including HN12 and HN10 are positive correlated with covariances of about 0.1$(\text{hPa})^2$. Station N4 shows the nethermost covariance compared to the southern stations. An explanation could be the fact that the main wind directions were north-east and south-west. N4 lies hereby closer to the flow axis.

Figure 4.6 shows the correlations of the pressure perturbations.

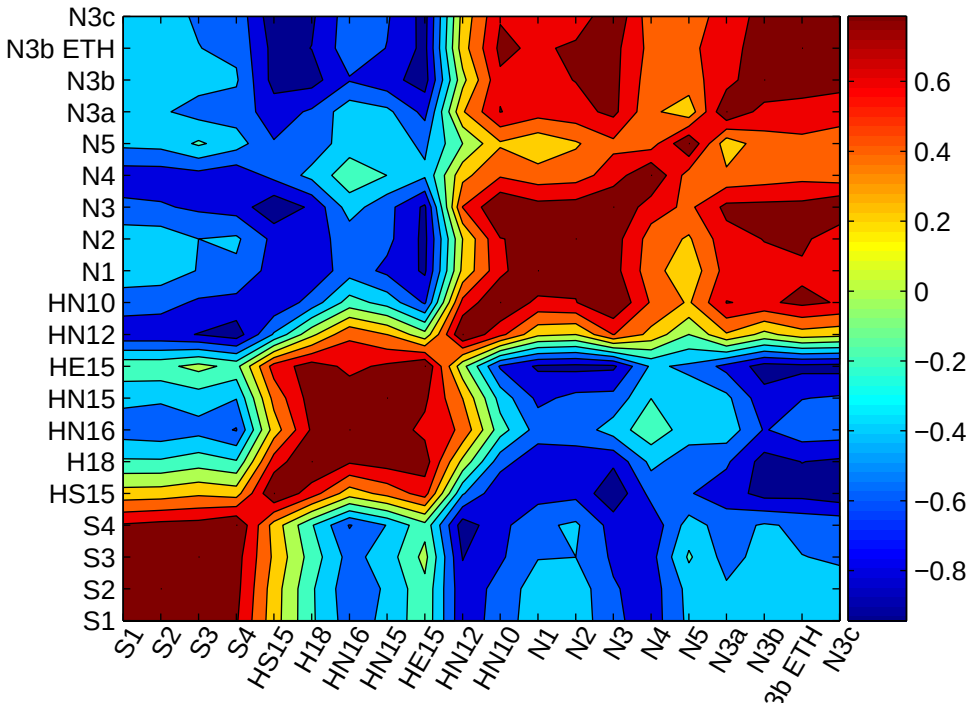

Figure 4.6: Pressure perturbation correlation.

Three areas of high correlation greater then 0.6 can be seen. One group of very uniform correlated stations are the ones in the south (S1 to S4). The mountain stations (HS15, H18, HN16, HN15 and HE15) form another group, however, with a more distinct structure. HS15, the station south of

the summit, is with a value of about 0.2 remarkable lower correlated to the northern stations HN16 and HN15. HN12 and HN10 have to be attributed to the northern stations, which form the last group (N1 to N5, HN12 and HN10). N5 shows a weaker correlation of 0.2 to 0.4 to all the other stations of the group, which might be explained by the more remote placement of the station in the east (figure 3.1).

4.4 Pressure Disturbance Profiles

Pressure disturbance profiles for the axis S1, HS15, H18, HN16, HN12, HN10, N3, N3a, N3b and N3c were calculated for four periods. Thereby, periods were chosen, in which the wind direction was relatively constant.

Period from 3 August to 4 August: The first period is from 3 August to 4 August with winds from east and wind speeds around 10 m/s. The stations in the north tend to have a southern wind component, while the ones in the south show a northern component. The summit station H18 shows winds directly from east. The stations HE15 and HN15 have as well a northerly component. The wind velocity measurements suggest that the stations H18, HE15 and HN16 suffered from icing, during that period. The station N1 differs from the rest of the northern stations by showing a northerly component. Since this station was placed in the north-east of the mountain, the lee side for that period, this is possibly caused by the flow around the mountain. The highest wind speeds occurred at the stations N1, N2, N4 and HS15 with values of 15 m/s. The stations N5, HN15 and HN16 show the smallest wind velocities around 5 m/s. It is not known if the values of HN15 and HN16 are caused by icing. The value of N5 seems plausible, since the station was on the windward side of the mountain during that period.

Figure 4.7 shows the pressure disturbance profile. The pressure disturbance profile of that period shows a positive disturbance over the centre of the mountain and negative values in the south and the north of the mountain. The values of H18 and HN16 are about 1 hPa. The negative perturbations are -1.25 hPa in the south and -0.75 hPa in the north. A second maximum can be observed at N3 with 0.25 hPa. The standard deviation is relative constant along the relief with values of 1 to 1.25 hPa. This maximum can be observed at all four periods described in this chapter. Even if the wind direction differs significantly. It seems to be caused by local orographic phenomena.

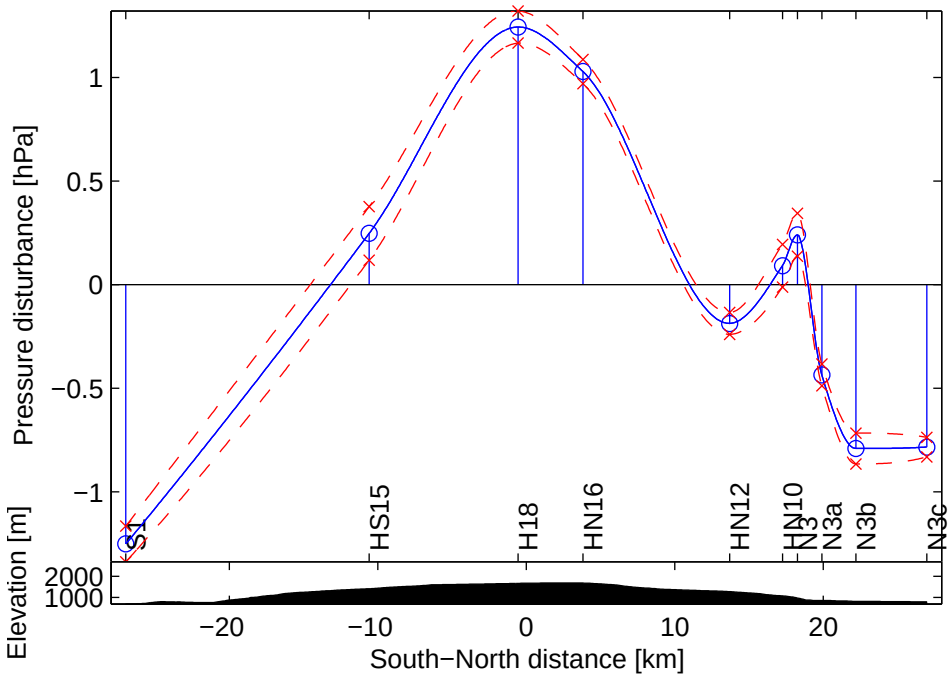

Figure 4.7: Pressure disturbance profile of the period from 3 August to 4 August. The lower part of the plot shows the relief of Hofsjökull with markers for the positions of the stations along the south-north axis. The solid line shows the mean pressure disturbance. The dashed lines show the standard deviations. The explicit values for the mean pressure disturbance and standard deviations at the stations are marked with circles and crosses. The values between the stations have been interpolated.

Period from 5 August 00:00–12:00 LT: The second period is from 5 August 00:00 to 12:00 LT. Winds were blowing from north with wind speeds of 5 to 10 m/s during that time. The stations H18, HN16, HN15 and HE15 suffered from icing. For H18 and HE15 neither wind direction nor wind speed measurements are available during that period. HN16 and HN15 show only wind direction readings, which have to be regarded with caution. It is not known if these measurements were influenced by icing as well. The northern stations show winds directly from north with wind velocities of 4 to 8 m/s. Station HN12 shows smaller values of about 2 to 6 m/s. The stations HN16 and HS15 show wind directions of north to north-east. Thereby, the largest wind velocities occur at station HS15 with values of 12 to 15 m/s. The stations in the south-east of the mountain, S3 and S4, measured as well north to north-easterly winds with velocities of 10 m/s. Station S2 in

the south shows large fluctuations in velocity and direction. The winds are varying between north-westerlies and north-easterlies with 2 to 10 m/s.

Figure 4.8 shows the pressure disturbance profile. The pressure perturbation shows a narrow but intense maximum at station N3 of 1.1 hPa. The neighbouring minimums are at the stations HN12 and N3b with values of about -0.1 hPa. A second maximum occurs at station HN16 with 0.5 hPa. The perturbation is close to zero at the summit station H18 and drops from there to the southern stations continuously to a value of -1.1 hPa at station S1. The northern stations, from stations N3c to HN16, have very small standard deviations of only 0.05 hPa. They grow going further south and reach values of 1.7 hPa at the southern stations HS15 and S1.

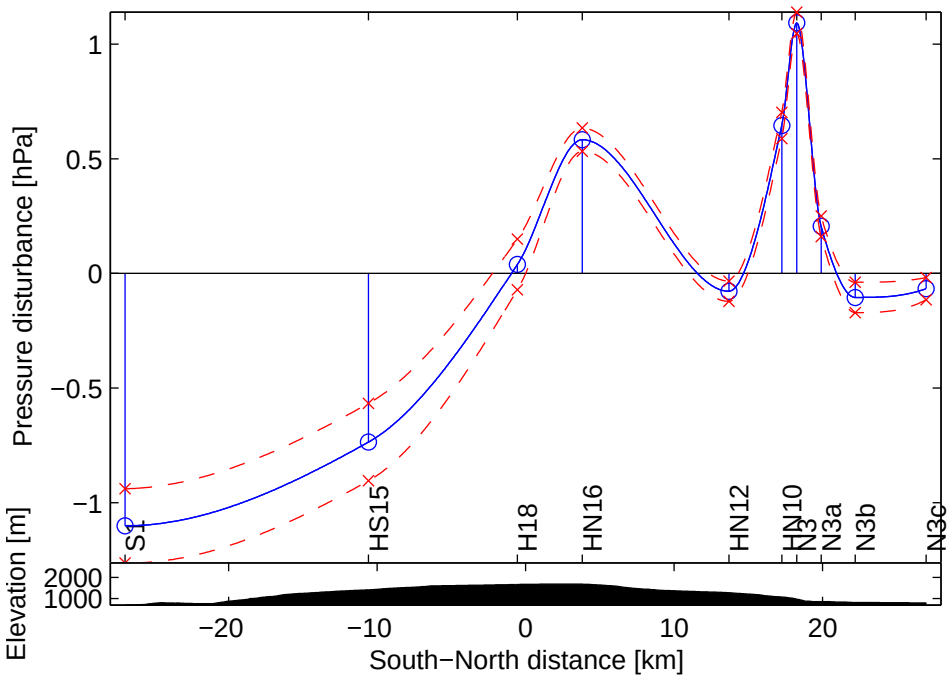

Figure 4.8: Pressure disturbance profile of the period from 5 August 00:00–12:00 LT. The lower part of the plot shows the relief of Hofsjökull with markers for the positions of the stations along the south-north axis. The solid line shows the mean pressure disturbance. The dashed lines show the standard deviations. The explicit values for the mean pressure disturbance and standard deviations at the stations are marked with circles and crosses. The values between the stations have been interpolated.

Period from 7 August to 10 August: The third period is from 7 August to 10 August with southerly winds. Wind speeds show a diurnal cycle during that time. The maxima were reached in the afternoon. The daily variations were strongest at station N4, N5 and N2. The mountain stations, especially HS15, H18, HN15 and HE15, show more constant wind speeds. The values are varying between 1 and 6 m/s at most of the stations. The highest wind speeds occur at the northerly stations N2, N3, N4 and N5, as well as HN16 with values up to 10 m/s. The directions were constant from south with little variations at most of the stations. Only the stations HS15, S3 and S4 showed strong departures from that. Station HS15 shows south-easterly winds, while the direction at the stations S3 and S4 have a westerly component. The stations N3b and N3a had some events of strong wind direction variations. Station N3b shows westerly winds midday 8 August.

Figure 4.9 shows the pressure disturbance profile. The pressure disturbance shows a strong maximum at the stations HS15 and H18 with 1 hPa. The disturbance is decreasing to the south, but still positive at stations S1 with 0.3 hPa. The decline in the north is much steeper than in the south. The perturbation drops to -0.7 hPa at station HN12. As in the profiles above, there is still a local maximum at the stations HN10 and N3. The disturbance is with -0.2 hPa still negative but approximately 0.5 hPa higher than at the surrounding stations. The standard deviation varies little between 0.05 and 0.07 hPa for all stations but N3a. There it increases to 0.19 hPa.

Period from 15 August to 16 August: The last period is from 15 August to 16 August with northerly winds again. The stations H18, HN16, HN15 and HE15 suffered again from icing. The wind speeds were relative uniform at the northern side of the mountain with values of 7 m/s on average. The stations N3 and N3b observed some fluctuations with wind velocities up to 30 m/s in the forenoon. The wind direction measurements varied very intense from that point of time at both stations. Station S2 shows large variations in wind speed and direction as well. The direction is cyclonic from north-east to west in the mean. The wind speed is fluctuating between 2 and 10 m/s. HS15 and S3 measured wind speeds of 10 to 20 m/s from north-east. The wind direction had a westerly component at station HN15 and a velocity of 7 m/s. It is not known how reliable these observations are due to the fact that this station suffered from icing.

Figure 4.10 shows the pressure disturbance profile.The pressure perturbation shows positive values in the north and negative values in the south. The maximum lies hereby at station N3 with 1.4 hPa. A second smaller maximum can be observed at station N3b with 0.8 hPa. This maximum is

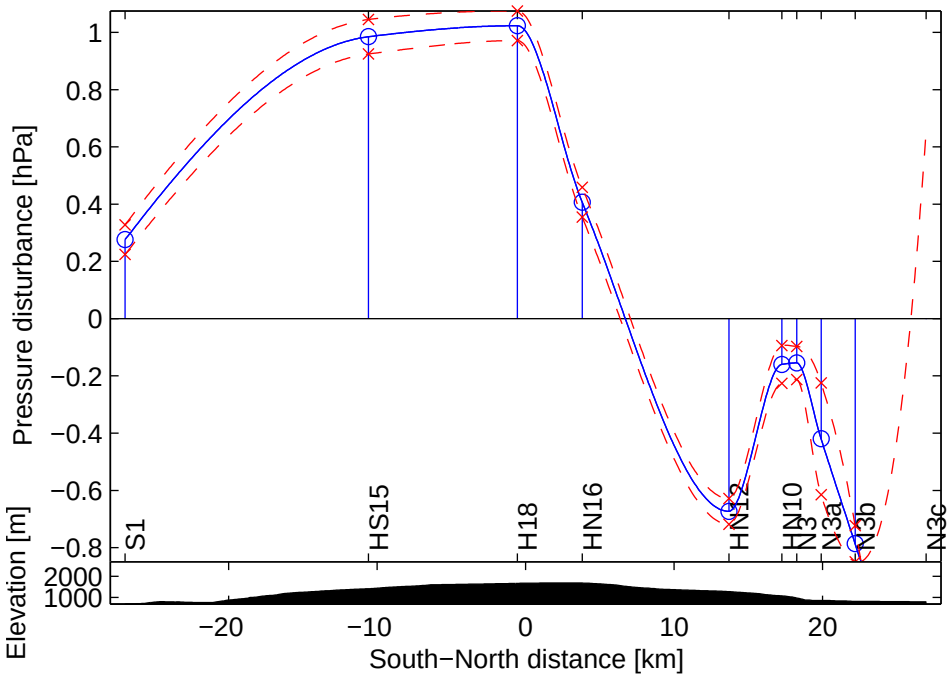

Figure 4.9: Pressure disturbance profile of the period from 7 August to 10 August. The lower part of the plot shows the relief of Hofsjökull with markers for the positions of the stations along the south-north axis. The solid line shows the mean pressure disturbance. The dashed lines show the standard deviations. The explicit values for the mean pressure disturbance and standard deviations at the stations are marked with circles and crosses. The values between the stations have been interpolated.

broader than that at station N2 and only 0.2 hPa greater than the neighbouring values. In the south of N3, the perturbation drops to -0.2 hPa at the stations HN12 and HN16. The decrease is not that continuously as in the case from 5 August. There is a second drop from station HN16 to H18 of -0.9 hPa. The disturbances of H18 and HS15 are of equal size with -1 hPa. At station S1, the perturbation is -0.8 hPa. The standard deviations of the disturbance are in the south approximately 1.5 hPa. In the north, including stations HN16 and HN12, they take values of 0.05 to 0.1 hPa. The largest standard deviation can hereby be observed at station N3b.

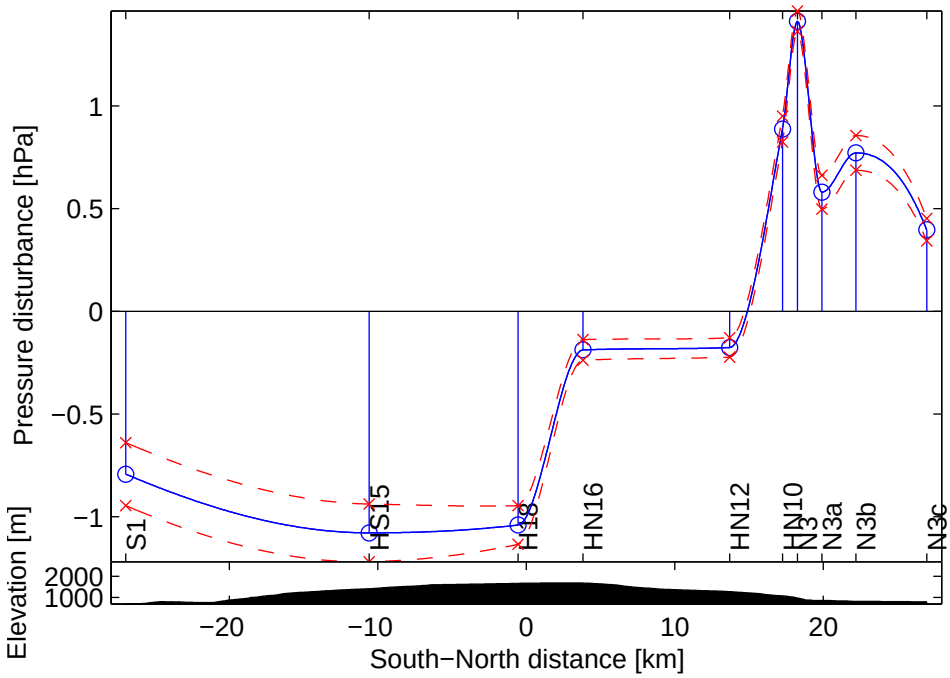

Figure 4.10: Pressure disturbance profile of the period from 15 August to 16 August. The lower part of the plot shows the relief of Hofsjökull with markers for the positions of the stations along the south-north axis. The solid line shows the mean pressure disturbance. The dashed lines show the standard deviations. The explicit values for the mean pressure disturbance and standard deviations at the stations are marked with circles and crosses. The values between the stations have been interpolated.

4.5 *Balloon* Soundings

Since the vertical wind soundings were bounded to fair weather conditions, it was not possible to conduct them on regular basis. Measurements had to be stopped during rain and bad visibility. The cloud base was as well crucial to the soundings by limiting the height of the ascents.

The first soundings were done on 29 July. They showed a constant wind from south west with velocities of approximately 7 m/s. The highest ascent was up to 1633 metres. On 30 July the wind direction was as well from south west turning anticyclonic within the lowest 100 metres. It changed to southerly winds during the day. Wind speeds were about 7 to 10 m/s relatively constant with height. The wind velocities near the ground were increasing during the day from 15 to 20 m/s. The winds changed to northerlies at 1 August. The profiles showed again very constant wind directions and

velocities of 5 to 10 m/s with height. During the soundings from 5 August, the northerly directions kept on with velocities of 5 to 7 m/s. The direction turned to north-west in the evening and to west on 6 August. The wind speeds were slightly increasing to 10 m/s.

The morning of 7 August, the direction in the lowest 500 metres was south-east with wind velocities from 6 to 2 m/s decreasing with height. Above 500 metres, they turned to west with more constant wind speeds of about 4 m/s. From 10:30 to 12:20 LT, winds were directly from south with 2 to 4 m/s, very constant in height, above 2000 metres slightly turning to west. The following profiles of the day show a commuting structure even with regions of northerly winds. The wind speed shows a clear minimum of 1 to 2 m/s in the height from 200 to 1100 metres. This height is congruent with that of the varying directions. It is very likely, that these wind perturbations are caused by waves over and in the lee of the mountain. These wind conditions continued until 10 August. The profiles of the first half of 8 August show a wave like pattern in the velocity profiles. Especially the profile of 8 August 12:30 LT (figure 4.11) shows oscillating wind velocities up to the height of 1500 metres. The values are commuting between 1 and 5 m/s with a wavelength of approximately 500 to 600 metres. The profiles 8 August 12:30, 14:25, 16:27 and 18:24 LT show northerly wind directions below 1000 metres.

From 12 August to 14 August, winds were north-easterlies with constant profiles of speed and direction. Wind velocities were about 7 to 10 m/s. Periods of northerly winds were often accompanied by low cloud cover in the north of the mountain. Due to this the average height of the ascents was between 500 and 1000 metres.

On 17 August, the profiles showed southerly winds again with approximately 5 m/s. The profile from 11:02 LT shows a clear wind shear at about 1213 metres. The direction below is south east, above it is turning to west. The following ascents did not reach that height. At 17:01 LT the profile shows northerly winds below 200 metres with speeds of 5 to 2 m/s decreasing with height.

On August 18, winds were westerlies with 2 to 4 m/s, relatively constant in velocity and direction. The general westerly direction kept on the next days. However on 19 August, the wind direction from the ground to 1500 metres were easterly.

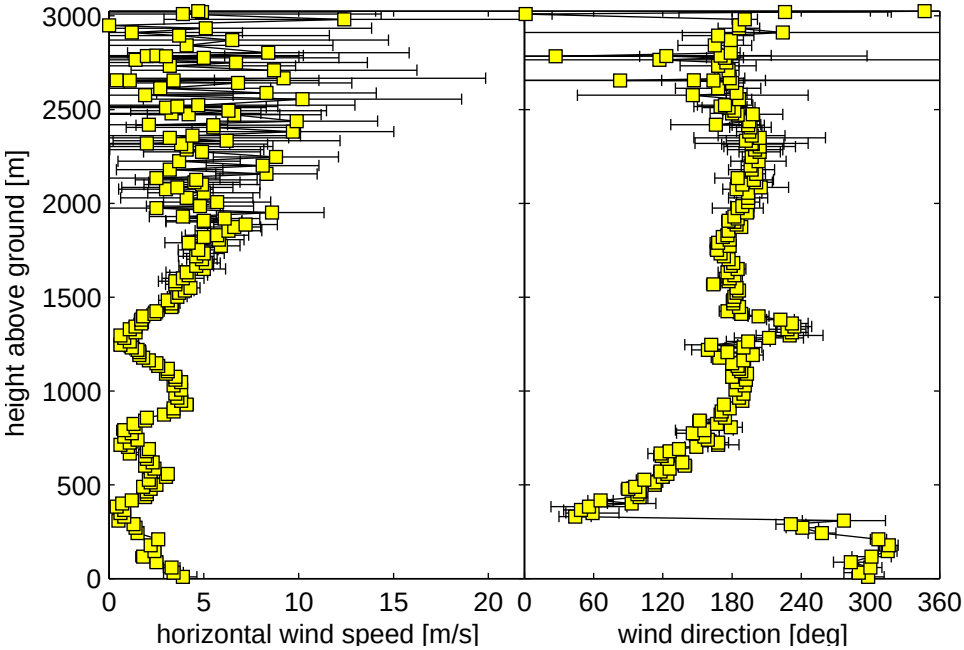

Figure 4.11: Wind profile of the balloon sounding from 8 August, 12:30 LT. The left plot shows the horizontal wind velocity in m/s, the right plot the wind direction in degrees.

4.6 *KALI* Soundings

The temperature profiles were adiabatic most of the time. The relative humidity showed a well mixed atmosphere during most of the ascents. Some inversions occurred as described in the following.

The ascent from 5 August 16:28 LT showed a constant temperature in the height of 1300 to 1400 metres. Relative humidity was decreasing by 20% from 90%. This inversion got stronger the next ascent and dropped to a height of approximately 1000 metres. There were constant winds from north with about 5 m/s during that time. The next day, 6 August, winds turned to westerlies. In the morning at 5:55 LT, an inversion was sounded at 500 metres. Below the relative humidity decreased with height from 80% at the ground to 60% at 500 metres. This inversion climbed during the next hours to approximately 900 metres and intensified. At 10:04 LT, the temperature increased from -1°C at 700 metres to 2°C at 900 metres. Relative humidity was at 80% to 100% below the inversion and dropped to 50% above. The winds were turning from north to west the night 5 August to 6 August.

An inversion at the ground was measured 7 August 6:36 LT about 200

metres thick (figure 4.12 and figure 4.13). The relative humidity was declining by 20% in that layer. It disappeared within the next two hours. At 14:20 LT a new inversion was forming at 1300 metres. It intensified and climbed up to 1600 metres. The relative humidity profile showed first a well mixed atmosphere with 80% up to 1500 metres. There, it increased to 95%. During the day the profile changed to a linear increasing one with values of 60% at the ground and 100% in 1700 metres. The following days, inversions could be found at 500 metres on 8 August (figure 4.14 and figure 4.15) and 1100 metres on 9 August. These were not that strong and disappeared after midday.

On 17 August 9:07 LT, a similar situation was present. The wind profile showed southerly winds with approximately 10 m/s. A strong inversion was found at 1200 to 1300 metres. The relative humidity was decreasing by 20% in that height. The inversion weakened in the time to the next ascent. The wind profile shows a strong shear in the height of the inversion. Therefore it might be different air masses instead of wave perturbations.

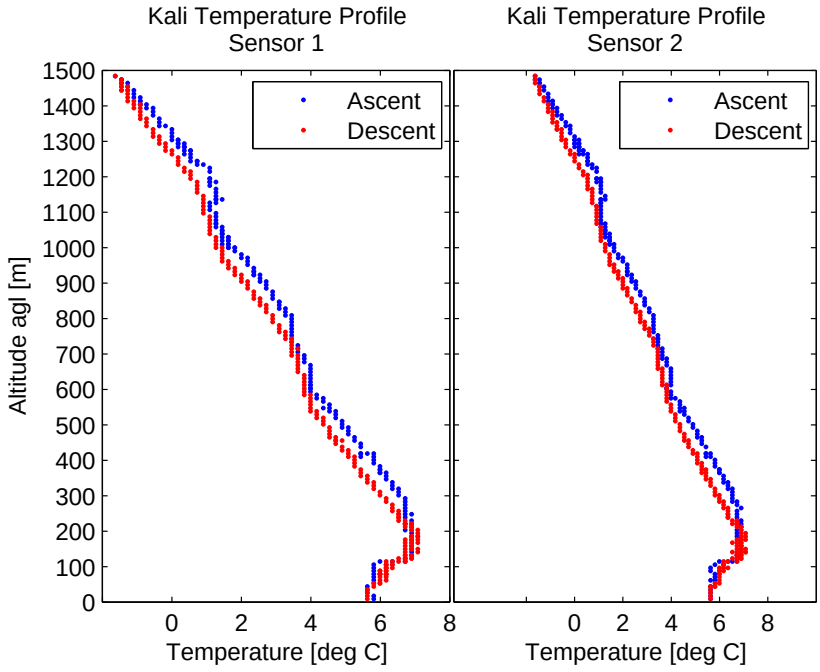

Figure 4.12: Kali temperature profile from 7 August 2007, 6:36 LT.

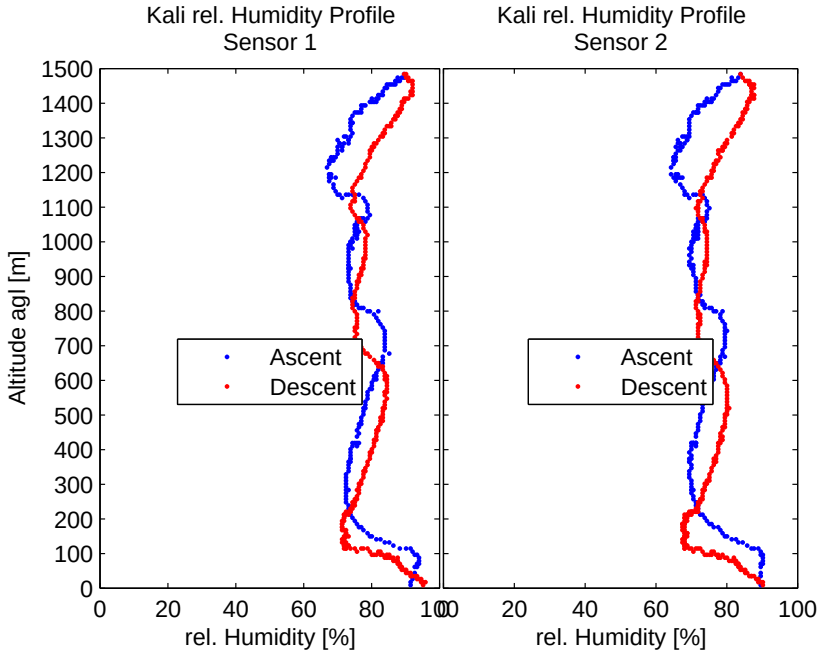

Figure 4.13: Kali relative humidity profile from 7 August 2007, 6:36 LT.

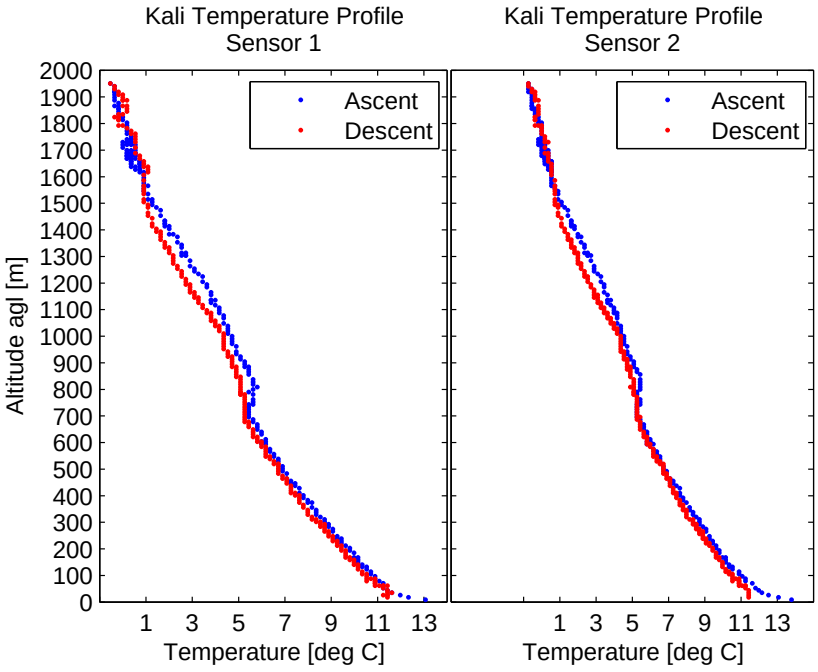

Figure 4.14: Kali temperature profile from 8 August 2007, 12:28 LT.

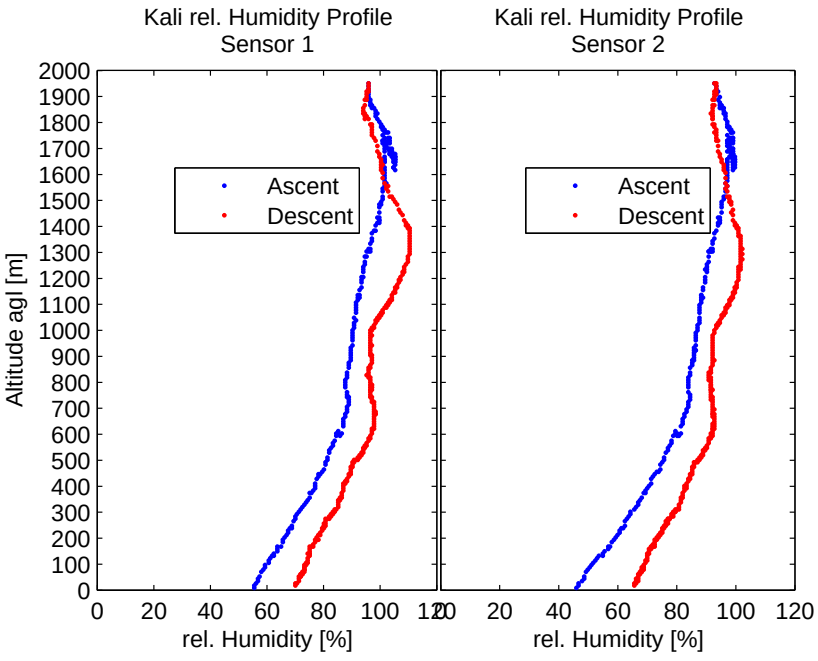

Figure 4.15: Kali relative humidity profile from 8 August 2007, 12:28 LT.

4.7 Linear 2D Model

Two 2D–models have been used in the present work. This section shows the results of the linear two–dimensional model, in which the vertical wind component is used at the lower boundary. It is compared with the two–dimensional model, in which pressure was used at the lower boundary in chapter 5.

First, the model is applied on a mountain with ideal shape. A single sinusoidal ridge of length L and maximal height H is considered. The background flow is constant and uniform with a value of 10 m/s. The buoyancy frequency N is $0.01\mathrm{s}^{-1}$ and the density ρ is $1.2\frac{\mathrm{kg}}{\mathrm{m}^3}$. Both are assumed to be independent of height. Rotation is neglected and the atmosphere is considered to be in hydrostatic equilibrium. The shape of the mountain is represented by:

$$\begin{aligned} h(x) &= \frac{H}{2}(\cos(\frac{2\pi}{L}x)+1) && x = -\frac{L}{2},\ldots,\frac{L}{2} \\ h(x) &= 0 && x < -\frac{L}{2}, x > \frac{L}{2} \end{aligned}$$

In this very case, $H = 1000$ metres and $L = 40$ kilometres. These physical dimensions are close to that of Hofsjökull. The single ridge can be represented as a Fourier series of the form:

$$\tilde{h}(x) = \frac{A_0}{2} + \sum_{s=1}^{\infty}(A_s\cos(k_s x) + B_s\sin(k_s x))$$

with known coefficients A_s and B_s, and horizontal wave numbers k_s. The structure of the vertical wind field over the mountain can be calculated by using equation (2.26) from chapter 2.3. Therefore, the vertical wave numbers m_s are calculated with the help of equation (2.27) from chapter 2.3. The complex amplitude is gained as followed. It is assumed that air parcels close to the surface will follow the slope of the ridge when they travel across. This boundary condition can be expressed by:

$$w'(z=0) = U\frac{\partial h}{\partial x} \tag{4.1}$$

If this is applied on each Fourier component $\tilde{h_s}(x) = A_s\cos(k_s x) + B_s\sin(k_s x)$ one gets:

$$w'_s(z=0) = Uk_s(B_s\cos(k_s x) - A_s\sin(k_s x)) \tag{4.2}$$

From equation (2.26) from chapter 2.3 we know the structure of the velocity field. It follows that:

$$
\begin{aligned}
w'_s(z=0) &= \Re[\widehat{w}_s \exp(i(k_s x))] \\
w'_s(z=0) &= \Re[\widehat{w}_{s,r}\cos(k_s x) - \widehat{w}_{s,i}\sin(k_s x) + i(\widehat{w}_{s,i}\cos(k_s x) + \widehat{w}_{s,r}\sin(k_s x))] \\
w'_s(z=0) &= \widehat{w}_{s,r}\cos(k_s x) - \widehat{w}_{s,i}\sin(k_s x) \qquad (4.3)
\end{aligned}
$$

Comparison of equation (4.2) and equation (4.3) yields an expression for $\widehat{w}$.

$$
\begin{aligned}
\widehat{w}_{s,r} &= U k_s B_s \\
\widehat{w}_{s,i} &= U k_s A_s
\end{aligned}
$$

The vertical wind field of each component is thus calculated by:

$$
\begin{aligned}
w'_s(x,z) &= \Re[(U k_s B_s + i U k_s A_s)\exp(i(k_s x + (m_{s,r} + i m_{s,i})z))] \\
w'_s(x,z) &= U k_s (B_s \cos(k_s + m_{s,r} z) - A_s \sin(k_s + m_{s,r} z))\exp(-m_{s,i} z)
\end{aligned}
$$

The horizontal wind perturbation can be calculated with the help of the continuity equation (2.22) from chapter 2.3.

$$
\begin{aligned}
&\frac{\partial u'}{\partial x} + \frac{\partial w'}{\partial z} = 0 \\
\Leftrightarrow &u'_s(x,z) = -\int \frac{\partial w'_s}{\partial z} dx \\
\Leftrightarrow &u'_s(x,z) = -\frac{m_s}{k_s} w'_s(x,z) \qquad (4.4)
\end{aligned}
$$

The perturbation of the pressure field is calculated with the aid of equation (2.20) from chapter 2.3.

$$
\begin{aligned}
&U\frac{\partial u'}{\partial x} + \frac{\partial 1}{\partial \rho}\frac{\partial p'}{\partial x} = 0 \\
\Leftrightarrow &U u' + \frac{1}{\partial} p' = 0 \\
\Leftrightarrow &p'(x,z) = -U\rho u'(x,z) \qquad (4.5)
\end{aligned}
$$

The calculated vertical wind field over the ideal mountain (Figure 4.17) shows wind values between -0.8 and 0.8 m/s. The vertical wind component

near the ground is, in conformity with the boundary condition, upward directed on the windward side of the mountain and downward directed on the lee side of the mountain. The highest wind speeds occur over the centre of the ridge. The whole vertical wind field shows a backward–tilted structure with alternating directions. The vertical wavelength is approximately 6400 metres. The horizontal dimension of the wind field is equal to that of the mountain.

The horizontal wind perturbation (Figure 4.18) is of opposite sign, as visible from equation (4.4). Regions of downward directed winds are congruent with a higher horizontal wind component and vice versa. With the background flow of 10 m/s, the horizontal wind component shows values of 1 to 20 m/s. The wavelength is equal to that of the vertical wind field. However, the structure of the horizontal wind perturbation is a little bit different. The perturbation field is broader than the mountain.

From equation (4.5) one can see that the pressure perturbation (Figure 4.19) distinguishes from the horizontal wind perturbation only by the constant value $-U\rho$, which is equal to $12\frac{\mathrm{kg}}{\mathrm{m}^2 s}$ in this case. The perturbation values reach from -1 to 1 hPa. The perturbation is positive on the windward side of the mountain and negative on the leeward side near the ground. High wind speeds lead to a negative perturbation and vice versa.

Figure 4.16 shows the streamline trajectories for the ideal mountain profile.

The same calculations were done for a Hofsjökull profile. The height data based on the 2000 Shuttle Radar Topography Mission. For the mountain profile, a south to north axis was taken, which was close to the axis covered by the stations: S1, HS15, H18, HN16, HN12, HN10, N3, N3a, N3b and N3c. The conditions were the same as for the ideal mountain profile. The buoyancy frequency was $0.01\mathrm{s}^{-1}$, the background wind was 10 m/s and density was again 1.2 $\frac{\mathrm{kg}}{\mathrm{m}^3}$. Hofsjökull was regarded as an isolated mountain with no other topography around. Since the topography of Hofsjökull is not symmetric, the calculations were done for northerly and southerly winds.

The perturbations show once again a backwards tilted structure. The vertical wind components are between -1.5 and 1 m/s (Figure 4.21). The upwind and downwind fields are now split up in four to five smaller fields per wave phase. Strong wind fields occur over steep slopes. Especially the long and steep slope on the southern side of the mountain relief excites extreme up and downwind fields. Two other, but not that extreme, wind fields are north of the summit and above the north side of the mountain. The vertical wavelength is between 6000 and 6500 metres.

The horizontal wind component shows values between 1 and 18 m/s. The structures of the wind fields are more similar to that of the ideal mountain.

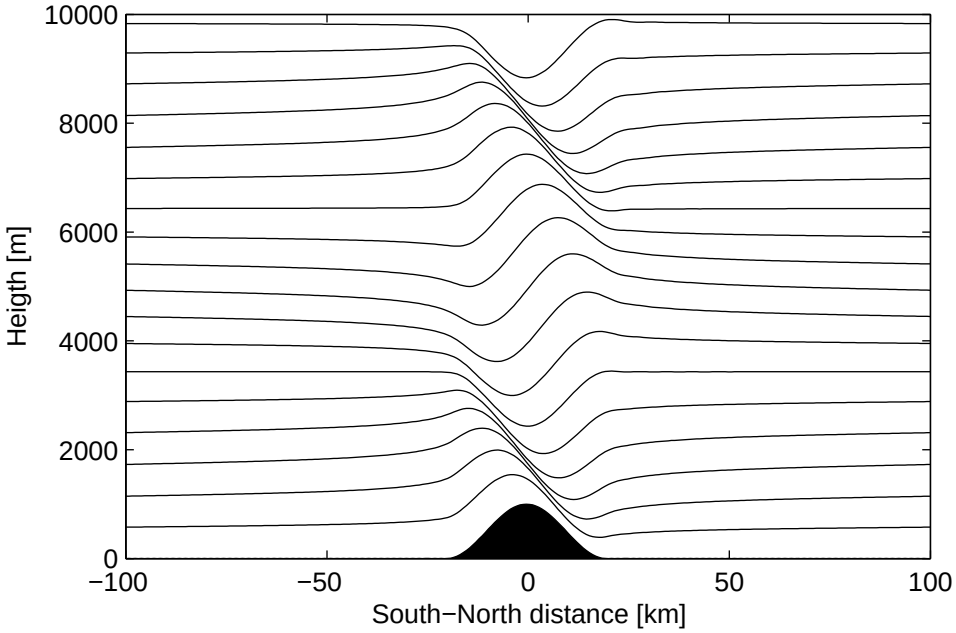

Figure 4.16: Streamline trajectories for the flow over an ideal mountain under steady and hydrostatic conditions.

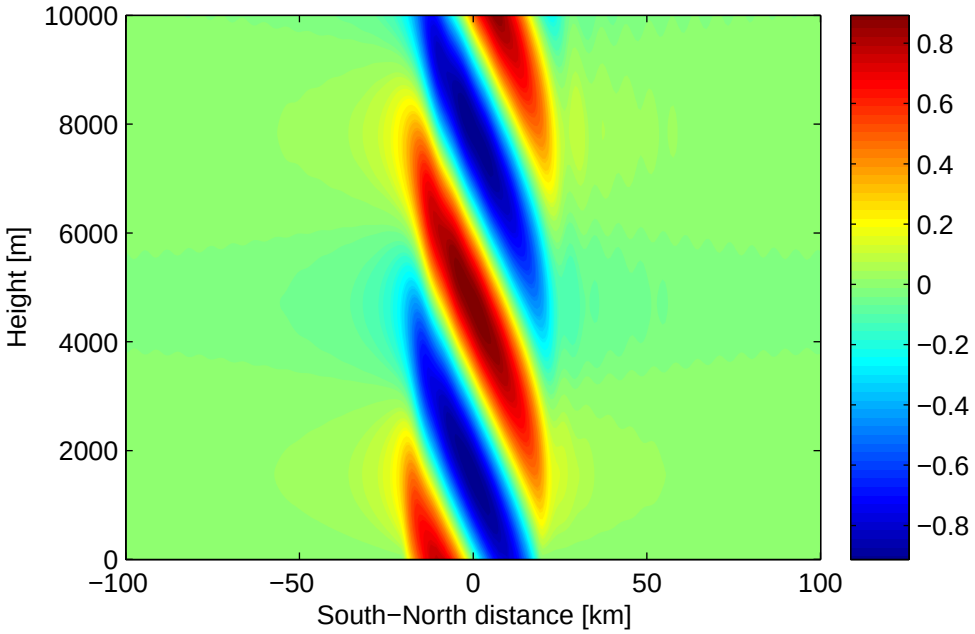

Figure 4.17: Vertical wind component in m/s for the flow over an ideal mountain under steady and hydrostatic conditions.

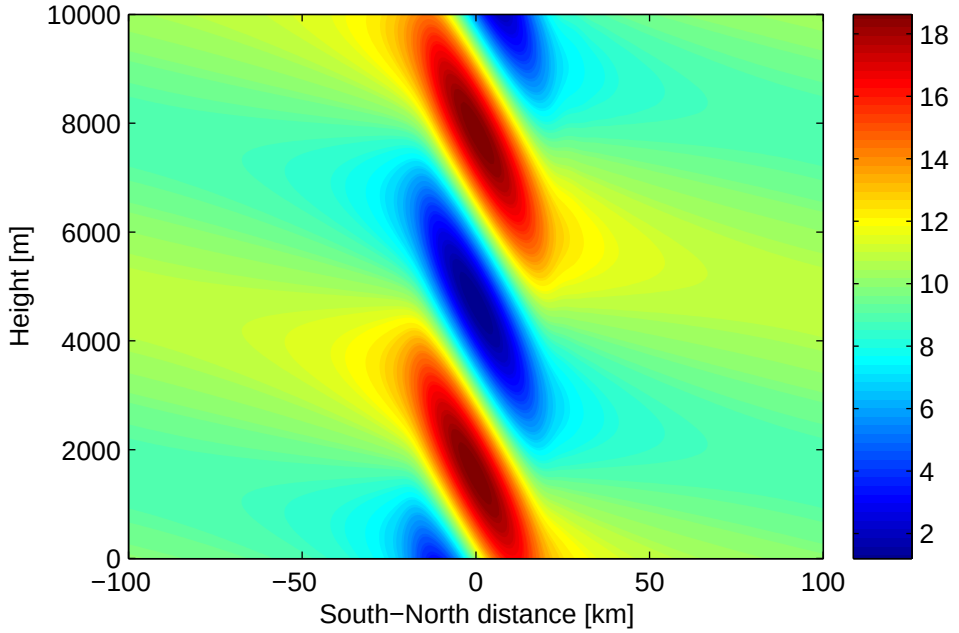

Figure 4.18: Horizontal wind component in m/s for the flow over an ideal mountain under steady and hydrostatic conditions.

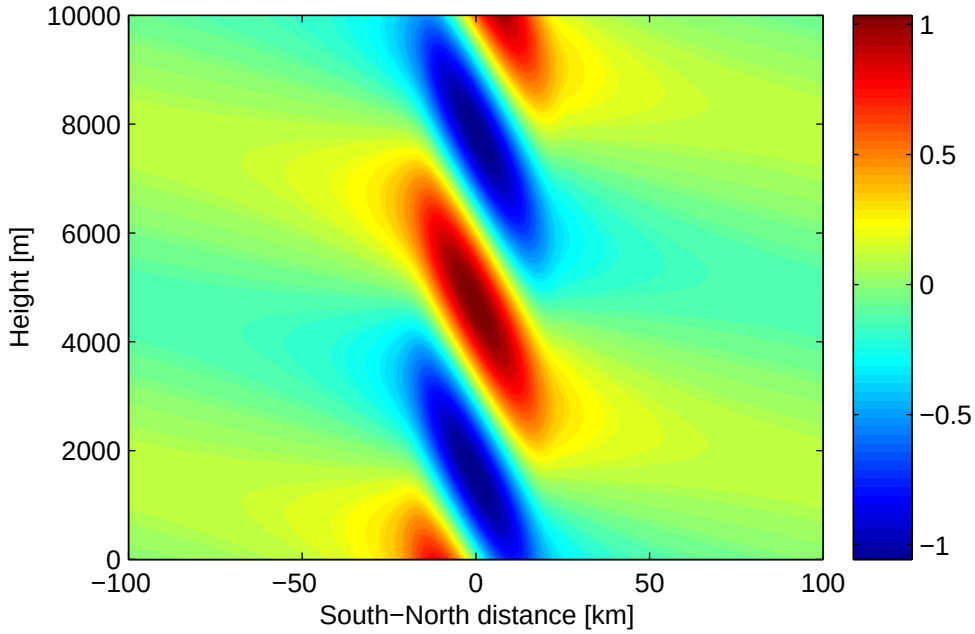

Figure 4.19: Pressure perturbation in hPa for the flow over an ideal mountain under steady and hydrostatic conditions.

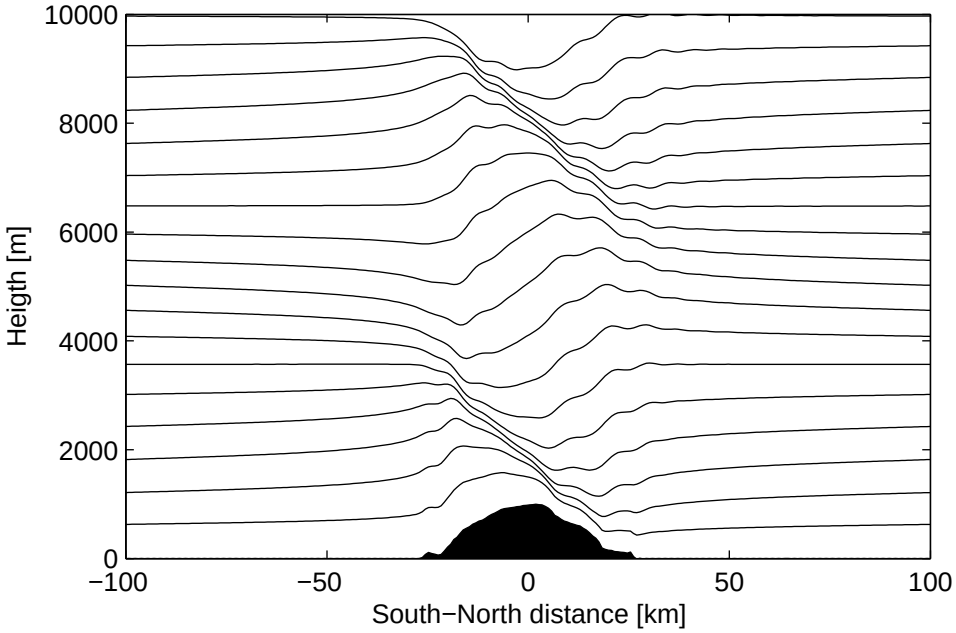

Figure 4.20: Streamline trajectories for southerly flow over a Hofsjökull profile under steady and hydrostatic conditions.

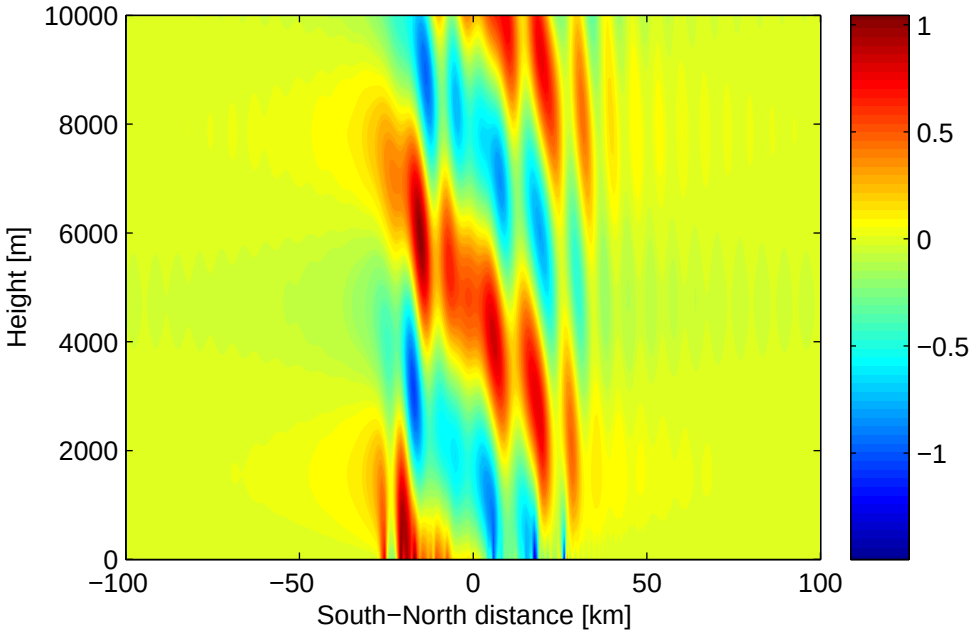

Figure 4.21: Vertical wind component in m/s for southerly flow over a Hofsjökull profile under steady and hydrostatic conditions.

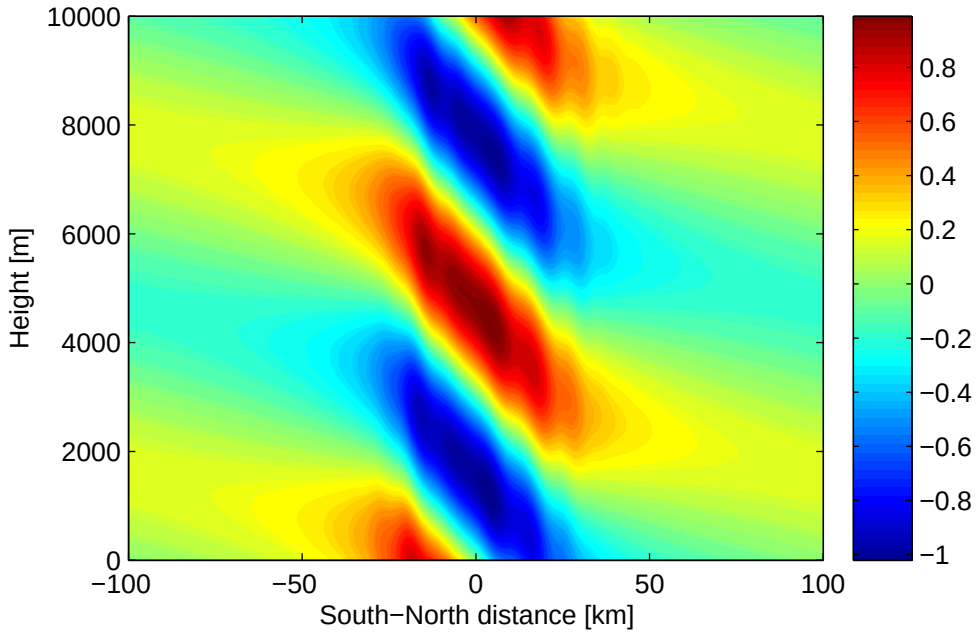

Figure 4.22: Pressure perturbation in hPa for southerly flow over a Hofsjökull profile under steady and hydrostatic conditions.

There is one big field of positive or negative horizontal wind perturbation for each phase of the wave. The same applies for the pressure perturbation fields (Figure 4.22). The values are between -1 and 1 hPa. The structure is the same as for the horizontal wind.

Figure 4.20 shows the streamline trajectories for the Hofsjökull profile.

4.8 Linear 2D Model with Pressure as Lower Boundary

The results of the two–dimensional model, in which pressure was used at the lower boundary, are presented in the following. These calculations have never been done before and where thus performed in two dimensions to start in a moderate manor. It was difficult to interpolate the pressure perturbations over the whole Hofsjkull area because of the irregular placement of the stations. Therefore the disturbance profiles were interpolated along the south to north axis described in section 4.4. The two–dimensional model was considered to approximate the structure of the wave more accurate.

For the solution of the two–dimensional model with pressure as lower boundary, three pressure profiles were used. These were the profiles with

northerly or southerly winds in the periods from 5 August 00:00 to 12:00 LT , 7 August to 10 August and 15 August to 16 August. A more detailed description of these profiles is presented in chapter 4.4. It was assumed that the pressure disturbance vanishes as one moves away from the mountain. An extrapolation was applied at both ends of the profiles. This was necessary, since the outermost points of the profiles, the stations S1 in the south and N3c in the north, did show non zero disturbances. This extrapolation was done by finding the points where the perturbation first vanishes. These points were calculated by the linear equation $x = -\frac{p'}{m}$ where x is the distance from the outer points, S1 respectively N3c, p' is the pressure disturbance at these points and $m = 0.015\frac{\text{hPa}}{\text{km}}$ is the assumed pressure gradient. The gradient was estimated from an analytic solution of the pressure field over Hofsjökull. The calculated points were added to the existing profiles. To gain a smooth profile, numerical interpolations were done between the points of the profiles. The background flow velocity was chosen as measured upstream of the mountain during that period. First, a constant background flow was assumed. The calculations have been repeated with a vertical sheared background flow. Here, the wind profiles of some pilot balloon ascents have been used. The buoyancy frequency was set to a typical value of 0.01s^{-1}.

Constant wind: The profile of 5 August 00:00 to 12:00 LT (Figure 4.23) shows a disturbance of -1.1 hPa at station S1 in the south. The disturbance was set to zero 73 km south of S1. The perturbation was much weaker in the north. It took only some few kilometres to decrease the perturbation to zero. The calculations show a periodical behaviour of the pressure perturbation in the vertical. The vertical wavelength is approximately 4500 metres. The maximum and minimum values are -1.25 and 1.25 hPa. One can see two separate perturbation fields in the horizontal. One very thin in the north with an horizontal extend of only some 10 km. The phase lines of these perturbations are much steeper than those of the second perturbation in the south. These perturbations likely represent the thin positive pressure disturbance seen in figure 4.8. The southerly disturbance reaches far more out to the south with an extend of about 100 km. Since the boundary values there have been extrapolated and are not based on observations, it is not known how realistic this structure of the perturbation is.

The profile from 7 August to 10 August (Figure 4.24) shows a more symmetric shape. The calculated pressure field above the mountain shows values ranging from -1.5 to 1.5 hPa. The vertical wavelength is approximately 3000 metres. The perturbations are not separated in several fields but have the structure of one field. Still, the influence of the local maximum at the

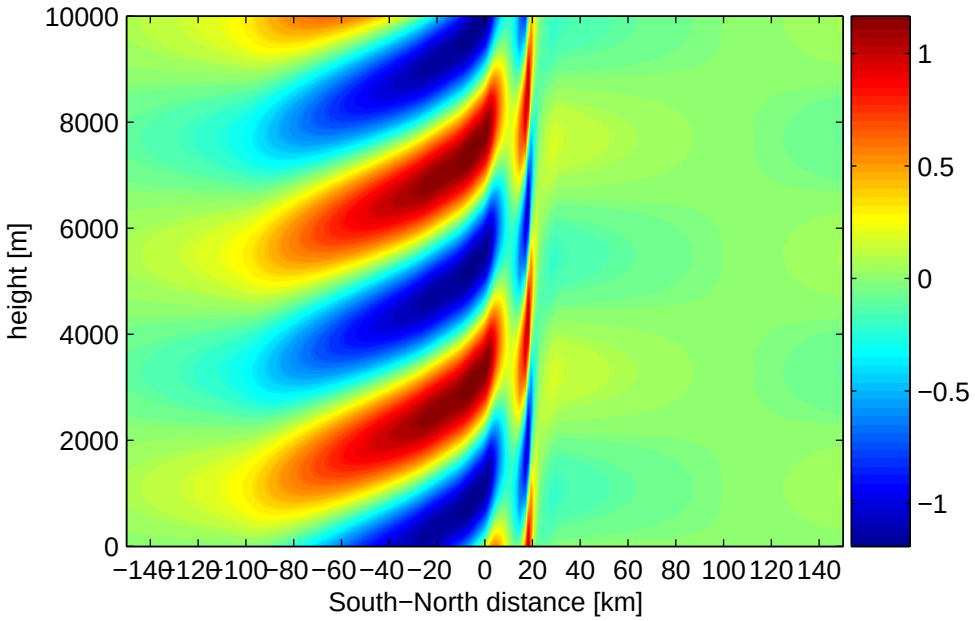

Figure 4.23: Pressure disturbance in hPa for the steady, hydrostatic flow over Hofsjökull with a constant wind of 7 m/s from north. The pressure disturbance profile from 5 August 00:00 to 12:00 LT was used as lower boundary.

stations HN10 and N3 is clearly visible in the vertical. The horizontal extend of the perturbations is about 120 km. It roughly matches the one calculated with the linear model based on the vertical wind at the surface (Chapter 4.7).

The profile from 15 August to 16 August (Figure 4.25) shows a negative perturbation in the south, similar to that from 5 August. The perturbation in the north is once again thinner but very intensive with a maximum of nearly 1.5 hPa. The structure of the perturbation field is similar to that of 5 August with a broad fading perturbation in the south and a sharp edged perturbation in the north. However, the disturbance is not separated into several smaller fields. The vertical wavelength is approximately 4500 metres.

Balloon wind profiles: For the calculation with varying wind speeds, wind profiles of the balloon soundings were used. Hereby, profiles with constant wind direction in height were used preferably. The balloon soundings had an average resolution of 10 metres. The wind profiles were averaged to a resolution of 50 metres via an arithmetic mean function. Most of the balloon soundings reached heights of 1000 to 3000 metres. To be able to calculate the perturbation up to 10000 metres, the wind profiles were extended. There-

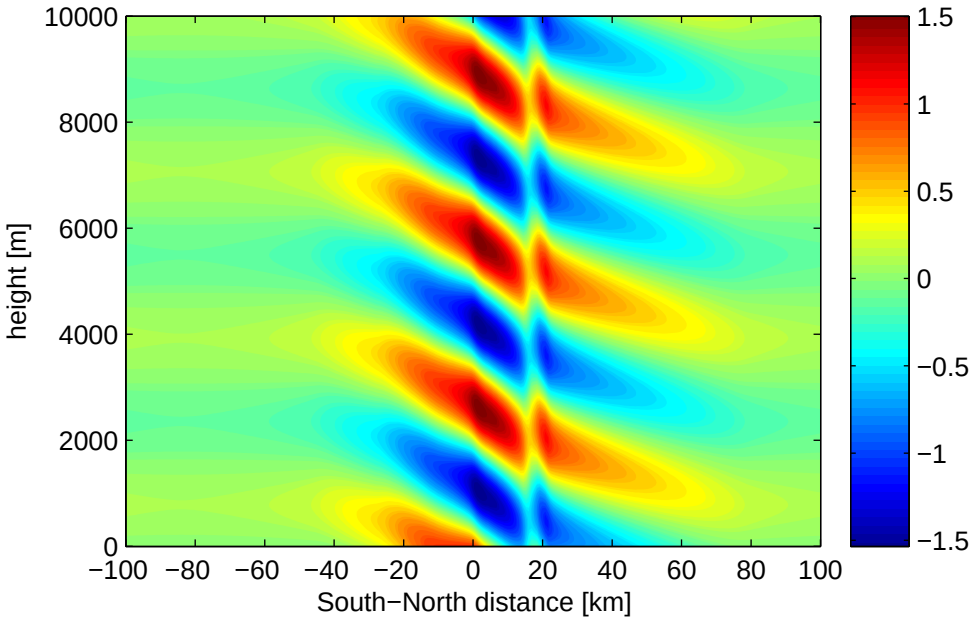

Figure 4.24: Pressure disturbance in hPa for the steady, hydrostatic flow over Hofsjökull with a constant wind of 5 m/s from south. The pressure disturbance profile from 7 August to 10 August was used as lower boundary.

fore, the wind velocity of the vertical sounding from Keflavik, measured by the University of Wyoming (www.umyo.edu) was used. For the profiles from 7 August to 10 August the vertical sounding from 7 August, 15:00 LT was used. For the profile from 15 August to 16 August the vertical sounding from 15 August, 12:00 LT was used. There was no vertical sounding at 5 August. For the profile from 5 August, 00:00 to 12:00 LT a constant wind was assumed above the last balloon measurement.

For the pressure profile from 5 August 0:00 to 12:00 LT, the balloon wind profile from 5 August 16:28 LT was used (figure 4.26). The average speed was about 5 m/s. Near the ground, wind velocities were higher with 10 m/s. The profile reaches up to 1200 metres and shows velocities of 9 m/s in the uppermost levels.

The perturbation in the upper regions is similar to the one before, even though with a higher wavelength due to stronger winds. Near the ground, the perturbation seizes in the region of the wind minimum. The vertical wavelength there is low, which leads to a weaker tilt of the perturbation field in that height.

For the pressure profile from 7 August to 10 August, three different wind profiles were used. The first was the profile from 7 August 10:33 LT (figure

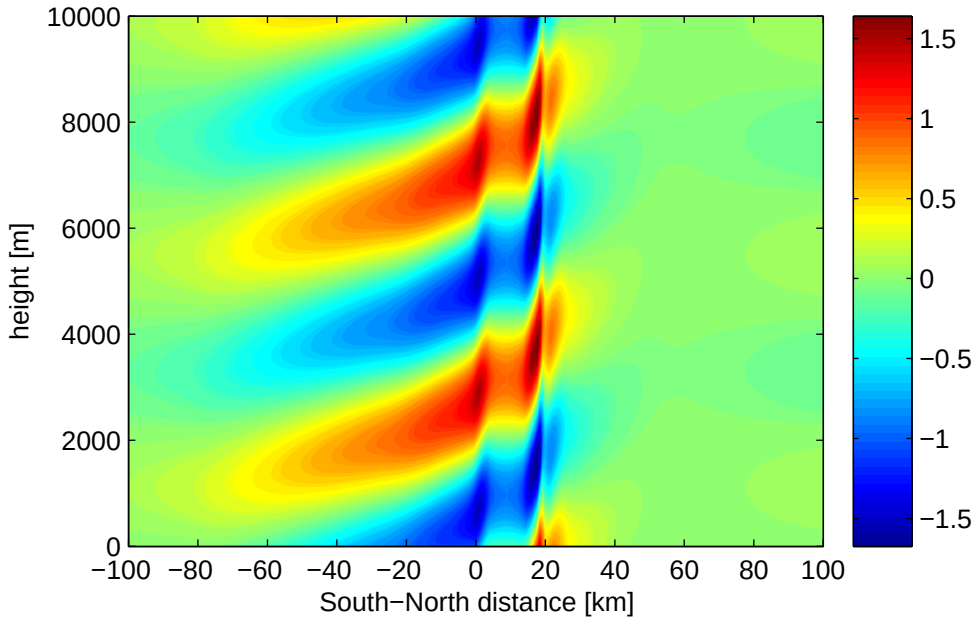

Figure 4.25: Pressure disturbance in hPa for the steady, hydrostatic flow over Hofsjökull with a constant wind of 7 m/s from north. The pressure disturbance profile from 15 August to 16 August was used as lower boundary.

4.27). It shows very calm winds of 1 m/s at the ground increasing to 2 m/s at a height of 500 metres. The region from 500 to 1200 metres shows relatively constant wind speeds of 2 to 2.5 m/s. From 1200 metres up to 1800 metres the velocity is increasing once again to 4 m/s. From this height on, the sounding from Keflavik was used. It shows high wind speeds of about 10 m/s up to a height of approximately 7000 metres. Above it increases up to 20 m/s.

The disturbance is very weak at the ground with a wavelength of approximately only 600 to 800 metres. Both wavelength and perturbation amplitude increase gradually with increasing wind speed. The horizontal extend grows as well with increasing wind velocities. The values of the perturbation range between -3 and 4 hPa. The thin maximum in the north is still visible in upper regions.

The second wind profile used is from 7 August 12:31 LT (figure 4.28) and reaches up to 3500 metres. It shows velocities of 6 m/s at the ground, which are declining to a minimum of 2 m/s in the height of 500 to 1000 metres. From there on, the wind is increasing linearly to 12 m/s at the uppermost level. Above 3500 metres, the profile is equal to the one mentioned above.

The disturbance field on the ground shows strong positive values in the

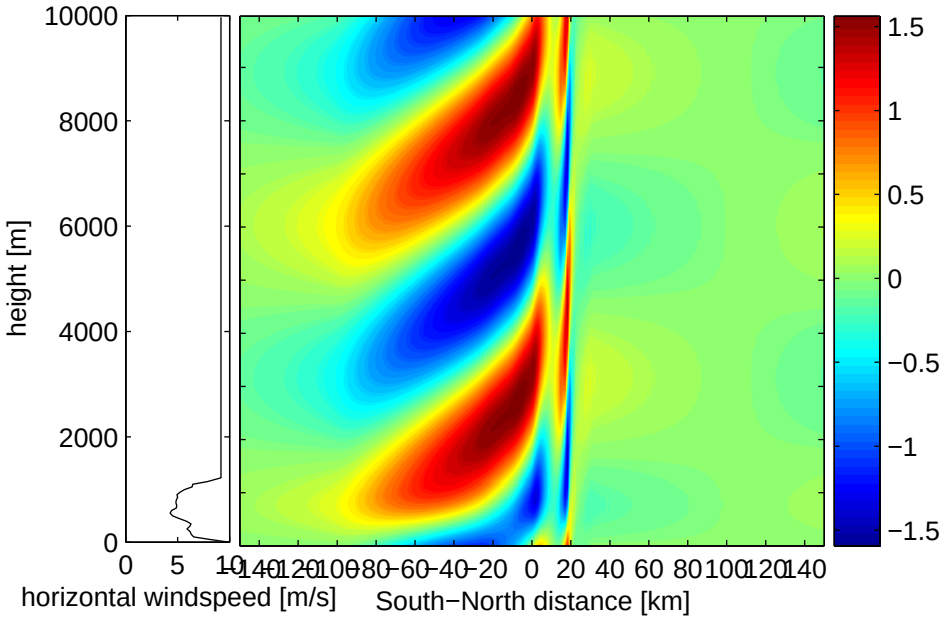

Figure 4.26: Pressure disturbance in hPa for the steady, hydrostatic flow over Hofsjökull from north. The pressure disturbance profile from 5 August 00:00 to 12:00 LT was used as lower boundary. The wind profile, shown on the left, is based on the balloon sounding from 5 August 16:28 LT.

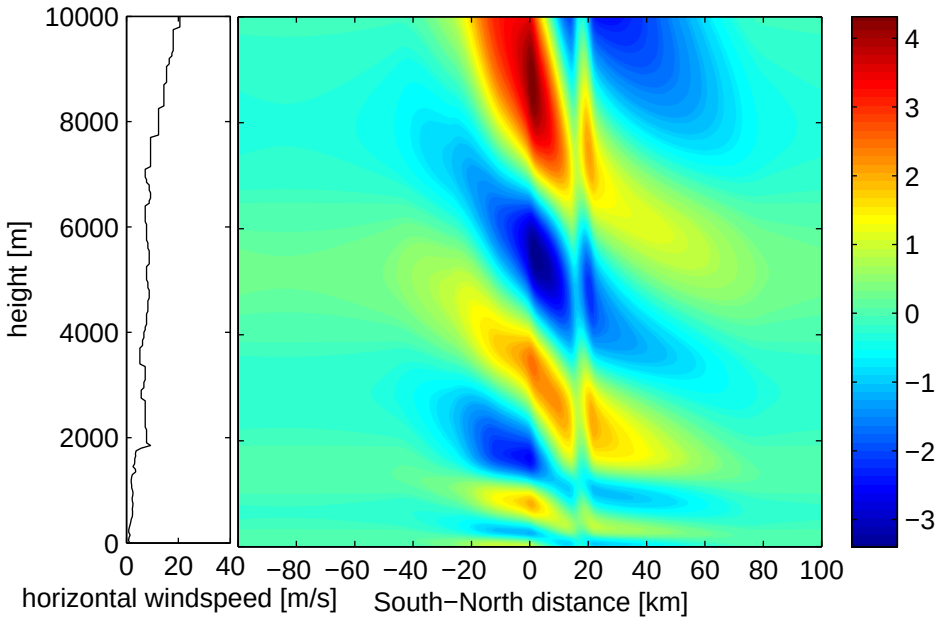

Figure 4.27: Pressure disturbance in hPa for the steady, hydrostatic flow over Hofsjökull from south. The pressure disturbance profile from 7 August to 10 August was used as lower boundary. The wind profile, shown on the left, is based on the balloon sounding from 7 August 10:33 LT and the vertical sounding from Keflavik from 7 August, 15:00 LT.

south and negative ones in the north. They reach up to a height of 500 metres with a small horizontal extend and sharp gradients. Up to the height of 2000 metres the disturbance is separated into several fields. The structure is not that of a upstream–tilting field, but more chess–board like. Tilt, horizontal extend and wavelength increase from 2000 metres on. This probably again caused by increasing wind speeds. The wavelength in the lower regions is approximately 1500 metres. Above it reaches values of 3000 to 4000 metres. The amplitude however does not increase that much. It shows values of only -0.4 to 0.8 hPa, which are smaller than the values at the ground.

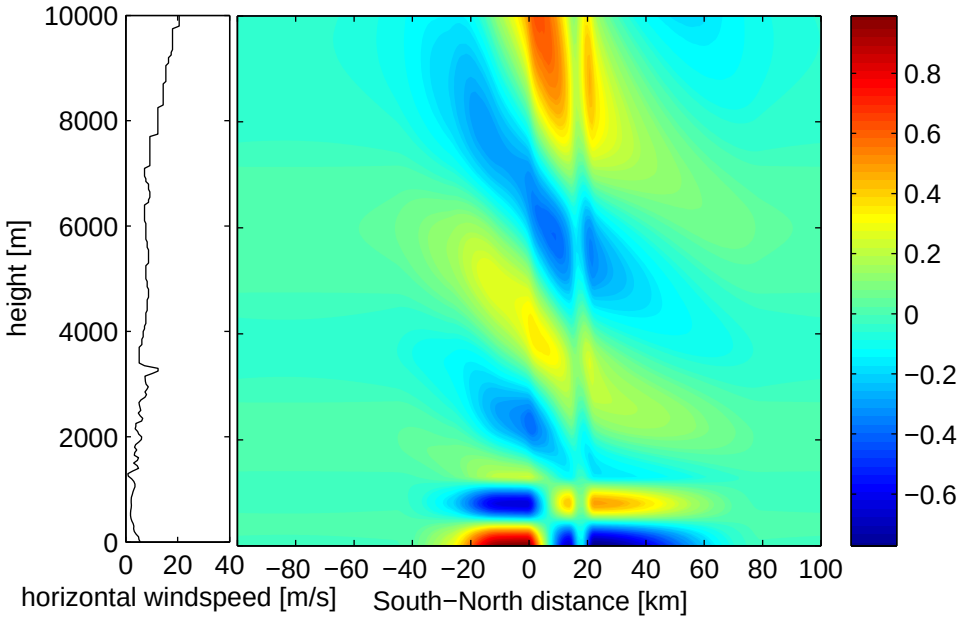

Figure 4.28: Pressure disturbance in hPa for the steady, hydrostatic flow over Hofsjökull from south. The pressure disturbance profile from 7 August to 10 August was used as lower boundary. The wind profile, shown on the left, is based on the balloon sounding from 7 August 12:31 LT and the vertical sounding from Keflavik from 7 August, 15:00 LT.

The last wind profile is from 7 August 18:27 LT. It shows high wind speeds of 7 m/s at the ground. From 200 to 1400 metres velocities are very constant with values of 2 to 3 m/s. At about 1800 metres, there is a sharp gradient. The profile above is as in the calculations before the one from Keflavik from 7 August, 15:00 LT.

The very regions near the ground show a strong but shallow perturbation with sharp gradients with values between -0.6 and 0.8 hPa. The perturbation seizes up to the height of 2000 metres. Tilt, amplitude and horizontal extend

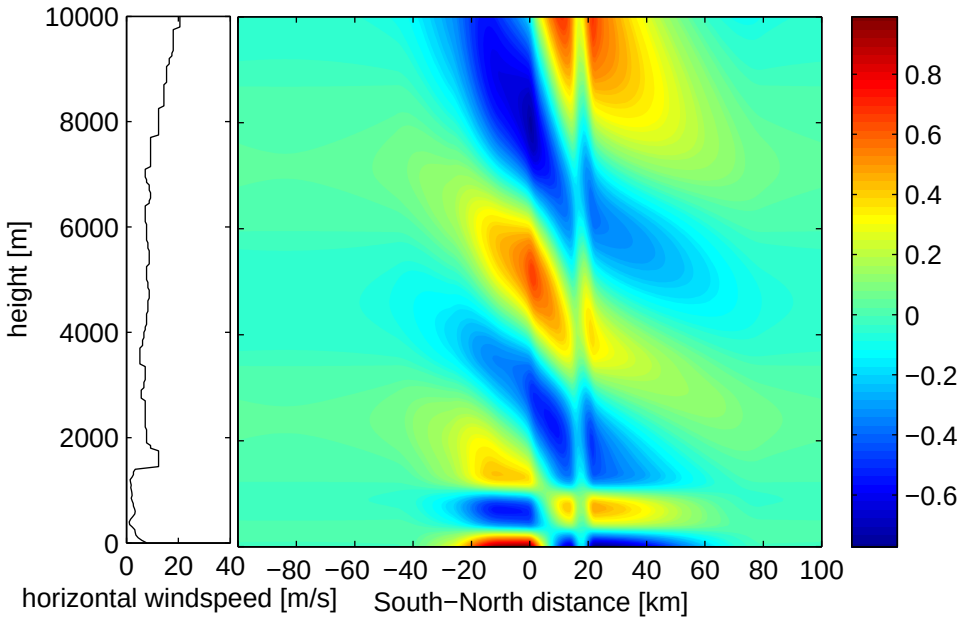

Figure 4.29: Pressure disturbance in hPa for the steady, hydrostatic flow over Hofsjökull from south. The pressure disturbance profile from 7 August to 10 August was used as lower boundary. The wind profile, shown on the left, is based on the balloon sounding from 7 August 18:27 LT and the vertical sounding from Keflavik from 7 August, 15:00 LT.

increase above. The structure of the perturbation is similar to that of the calculation with the wind from 7 August 12:31 LT. However, the amplitude of the perturbations is higher above 1800 metres.

The wind profile from 15 August 14:06 LT, which was used for the last disturbance profile from 15 August to 16 August, reaches only up to the height of 450 metres. The velocity at the ground is approximately 6 m/s and increases to 10 m/s in a height of 200 metres. The sounding from Keflavik from 15 August, 12:00 LT shows high but rather constant wind speeds of about 10 to 20 m/s.

The perturbations have very regular structure because of the constant wind speeds. There is on region of less amplitude and horizontal extend in the height of approximately 3000 to 4000 metres, which is congruent to a region of smaller wind velocities. The small region of lower wind speeds at the ground does not seem to have a large impact on the perturbation. The amplitudes show values between -1 and 1.5 hPa. The regions of strong pressure perturbation gradients (see figure 4.10) are still visible in the upper regions. The perturbation is stronger on the south side of the mountain with weaker gradients.

Figure 4.31 shows the comparison of the Hofsjökull height profile and the recalculated profile. For the calculation of the height profile the pressure disturbance, calculated with the pressure profile from 7 August to 10 August with the wind profile from 7 August 10:33 LT, was used. The recalculated profile differs significantly from the Hofsjökull profile. The height of the profile reaches values of 8000 metres. There are two maxima. The second maxima is probably caused by the thin maxima in the pressure profile. The profile shows two depressions flanking the recalculated "mountain". The new height profile is broader than the Hofsjökull profile.

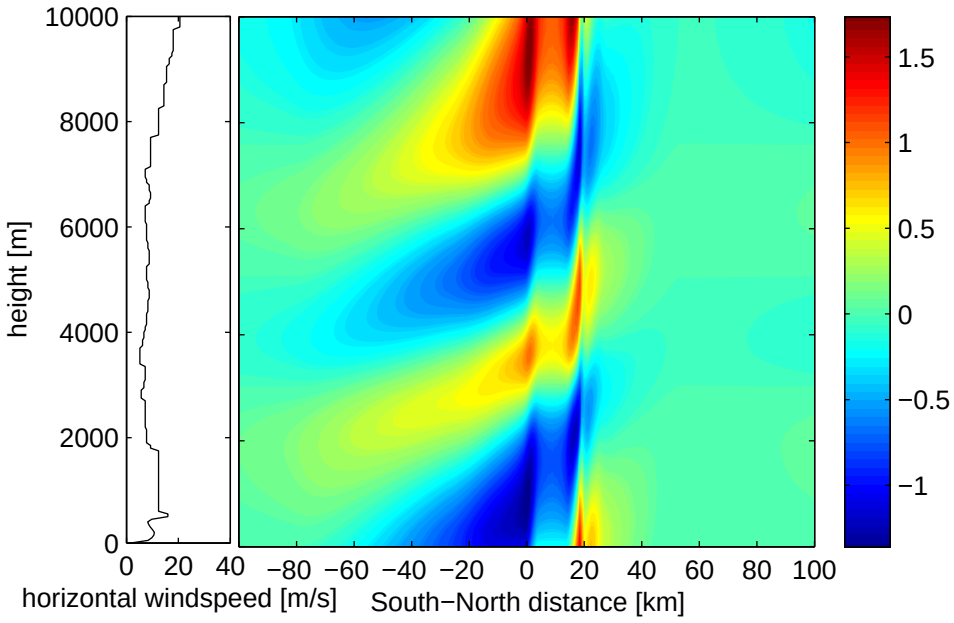

Figure 4.30: Pressure disturbance in hPa for the steady, hydrostatic flow over Hofsjökull from south. The pressure disturbance profile from 15 August to 16 August was used as lower boundary. The wind profile, shown on the left, is based on the balloon sounding from 15 August 14:06 LT and the vertical sounding from Keflavik from 15 August, 12:00 LT.

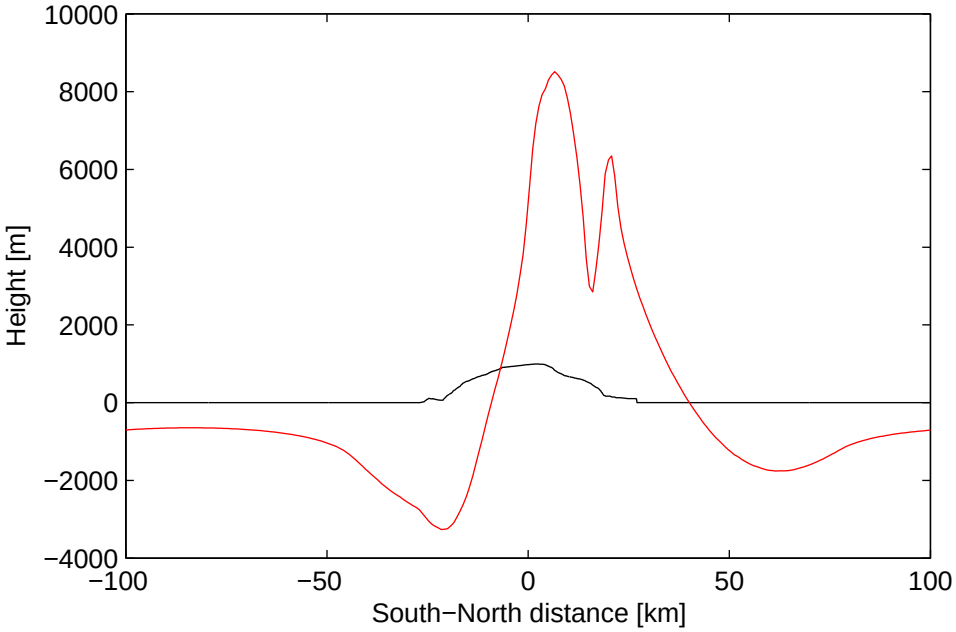

Figure 4.31: Height profile of Hofsjökull (black line) and recalculated height profile (red line) of the pressure disturbance profile from 7 August to 10 August with the wind measurements from 7 August 10:33 LT.

4.9 Linear 3D Model

This chapter provides a view on the calculations of the linear three–dimensional model. As in chapter 4.7 for the two–dimensional model, the model is first applied on a mountain with ideal shape. The height function is a combination of two sinusoidal functions. The model is based on Spengler's model for three–dimensional gravity waves (2008).

$$h(x,y) = \frac{H}{2}((\cos(\frac{2\pi}{L_x}x)+1)(\cos(\frac{2\pi}{L_y}y)+1)) \qquad x,y = -\frac{L_{x,y}}{2},\ldots,\frac{L_{x,y}}{2}$$

$$h(x,y) = 0 \qquad x,y < -\frac{L_{x,y}}{2}, x,y > \frac{L_{x,y}}{2}$$

The horizontal length $L_{x,y}$ of the mountain was set to 40000 metres. The height of the mountain H was set to 1000 metres. We assume a wavelike solution of the form $w' = \widehat{w}\exp(i(kx+ly+mz))$ with complex amplitude $\widehat{w}$, horizontal wave numbers k and l and vertical wave number m. The lower boundary condition is once again:

$$w'(z=0) = U\frac{\partial h}{\partial x} \tag{4.6}$$

Which states that the air parcels have to follow the slope when travelling over the mountain. The mean flow was set to 10 m/s. The buoyancy frequency is set to a typical value of 0.01s^{-1}. For the explicit calculation a Fourier transformation was applied on the topography defined by:

$$\widehat{h}(k,l) = \frac{1}{4\pi^2}\iint_{-\infty}^{\infty} h(x,y)\exp(-i(kx+ly))dxdy$$

With the inverse transformation defined by:

$$h(x,y) = \iint_{-\infty}^{\infty} \widehat{h}(k,l)\exp(i(kx+ly))dkdl$$

The lower boundary condition (4.6) becomes hereby:

$$\widehat{w'}(z=0) = Uik\widehat{h}(k,l)$$

Where the hat describes the Fourier transform of w' and h. The full solution is then calculated via:

$$\widehat{w'}(k,l,z) = Uik\widehat{h}(k,l)\exp(imz)$$

Which needs to be transformed back to x–y space. A more detailed view of the calculation with Fourier transformations can be found in Smith (1980).

The calculations near the ground show a positive vertical wind component in front of the mountain and a downwind component behind the mountain. The phase lines tilt upstream and outwards. The main wave occurrence is concentrated over the mountain but wave trails form downstream laterally. The horizontal structure of the wave is parabolic with the vertex over the mountain. The parabola is widening with increasing height. The amplitude of the up and downwind fields is varying between -0.8 and +0.8 m/s. The most extreme values occur near the ground in the region of the highest gradients of the topography relative to the flow. The disturbance is decreasing in the vertical. Smith (1980) provides a detailed analysis of the three–dimensional flow past an isolated mountain.

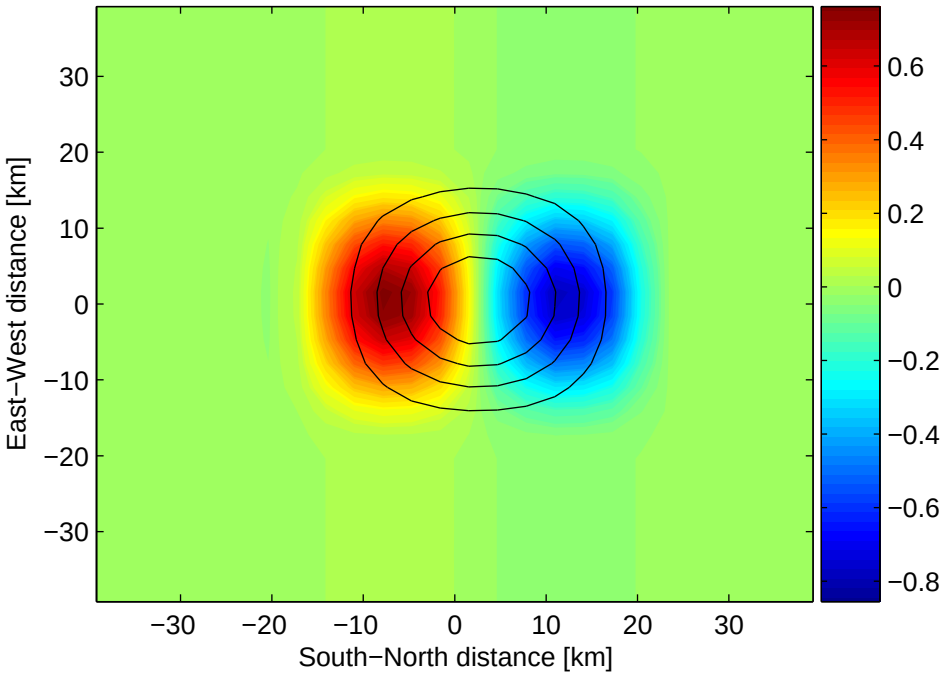

Figure 4.32: Vertical wind component (m/s) at ground level for the three–dimensional, steady and hydrostatic flow over an ideal mountain. The flow direction is from south to north. The figure shows the view from above. The topography is shown by the black lines.

The calculations were repeated for the topography of Hofsjökull under southerly flow. The mean wind speed was once again set to 10 m/s. The

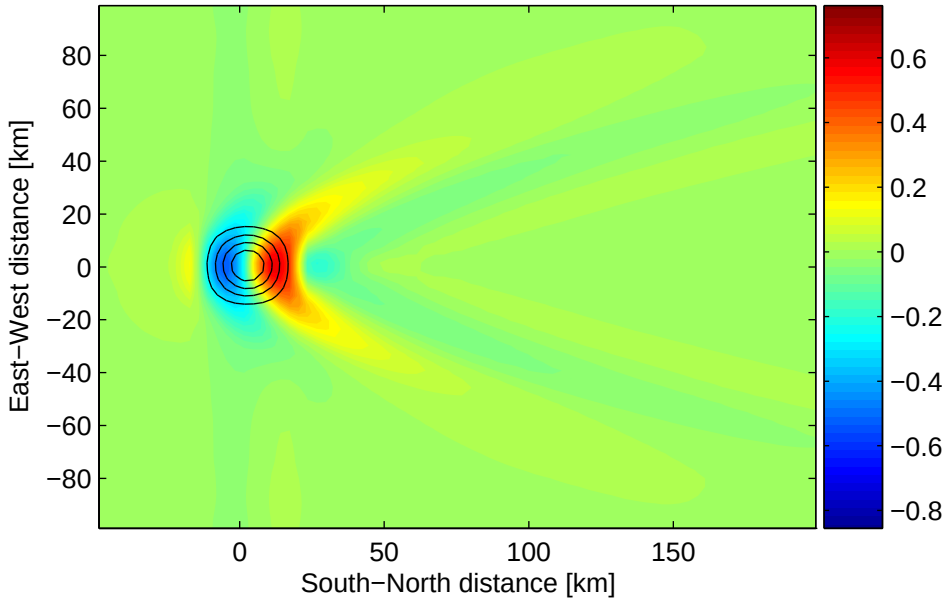

Figure 4.33: Vertical wind component (m/s) in 2500 metres for the three–dimensional, steady and hydrostatic flow over an ideal mountain. The flow direction is from south to north. The figure shows the view from above. The topography is shown by the black lines.

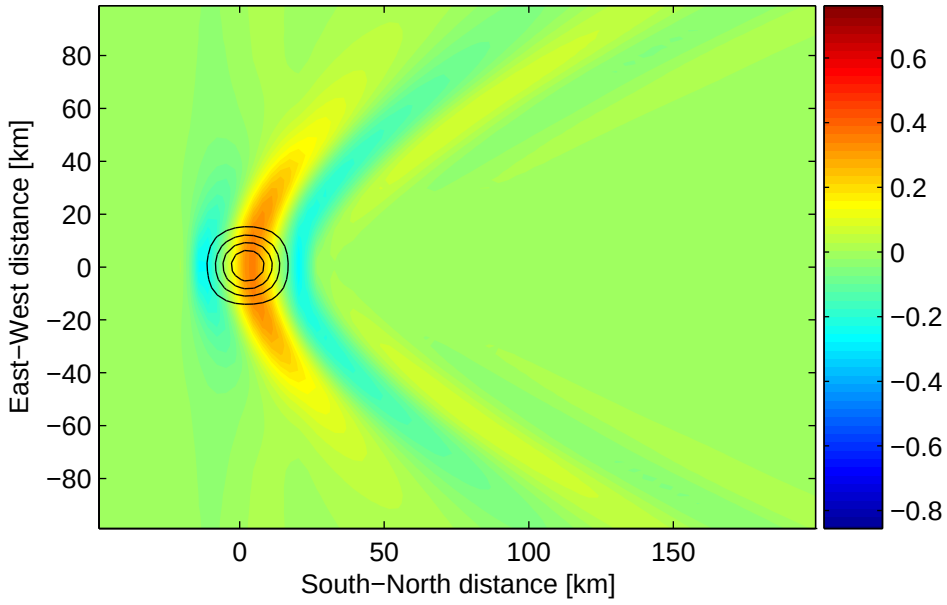

Figure 4.34: Vertical wind component (m/s) in 10000 metres for the three–dimensional, steady and hydrostatic flow over an ideal mountain. The flow direction is from south to north. The figure shows the view from above. The topography is shown by the black lines.

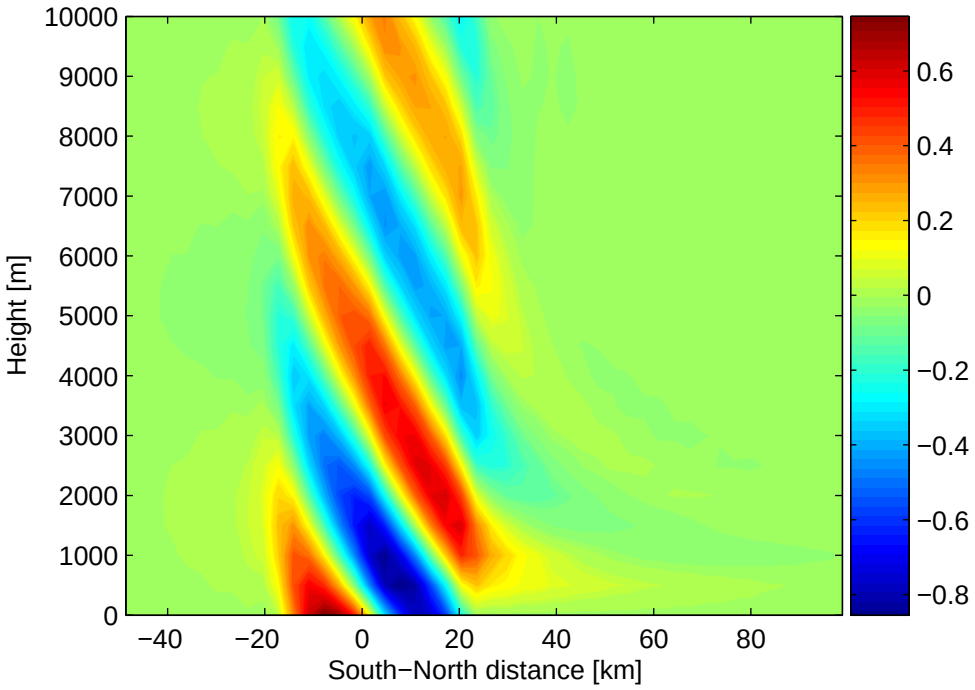

Figure 4.35: Vertical cross section of the vertical wind component (m/s) along the flow axis for the three dimensional, steady and hydrostatic flow over an ideal mountain. The flow direction is from south to north.

buoyancy frequency was set to $0.01s^{-1}$. The topography was based on data from the 2000 Shuttle Radar Topography Mission. The vertical wind at the ground shows maximum values of about 0.5 m/s in the southern sloping regions and south of the summit Miklafjell in the east. The downwind regions are concentrated at the north-easterly part of the mountain and north of the summit. The region of strongest downwind is located north of Miklafjell with a value of -0.8 m/s. The extreme values occur, as in the case of the ideal mountain, in regions of strong topographic gradients relative to the mean flow. The trailing perturbation fields are in general very weak and do barely exceed ± 0.1 m/s. The perturbation is separated into several fields according to the irregular topography. Thereby, the steep slopes to the north and south of Miklafjell in the north-east of Hofsjökull have a major impact on the disturbance. The strongest vertical wind components can be found north of Miklafjell. The disturbance is declining with height.

Compared to the results of the two–dimensional model in section 4.7, in which the vertical wind perturbation was concentrated over the mountain, it penetrates further downstream in the threedimensional model (figures 4.35 and 4.39. Especially in the lower regions up to 2000 metres, the perturbation is visible 80 kilometres from the mountain top. The amplitude is weak with values ranging between -0.2 to 0.2 m/s.

The calculations have been repeated for a non-hydrostatic regime. Thereby, equation (2.49) was used for the calculation of the vertical wave number m. The figures 4.40 to 4.42 show the results of the calculations. The vertical cross sections of the calculations for the ideal mountain do not show remarkable differences. This is probably because the shape of the ideal mountain is very smooth and regular so that non-hydrostatic modes excited only minimal. The comparison of the vertical cross sections for Hofsjökull shows a more distinct wave structure in the lee of the mountain for the non-hydrostatic regime. Both the hydrostatic and non-hydrostatic regime show a trailing perturbation in the lee of the mountain, but with different structure. Especially in the higher regions above 7000 metres in the lee of the mountain, the amplitude of the perturbation is stronger for the non-hydrostatic regime. One can see that as well in the figures showing the perturbation field from above in 10000 metres (figures 4.38 and 4.42).

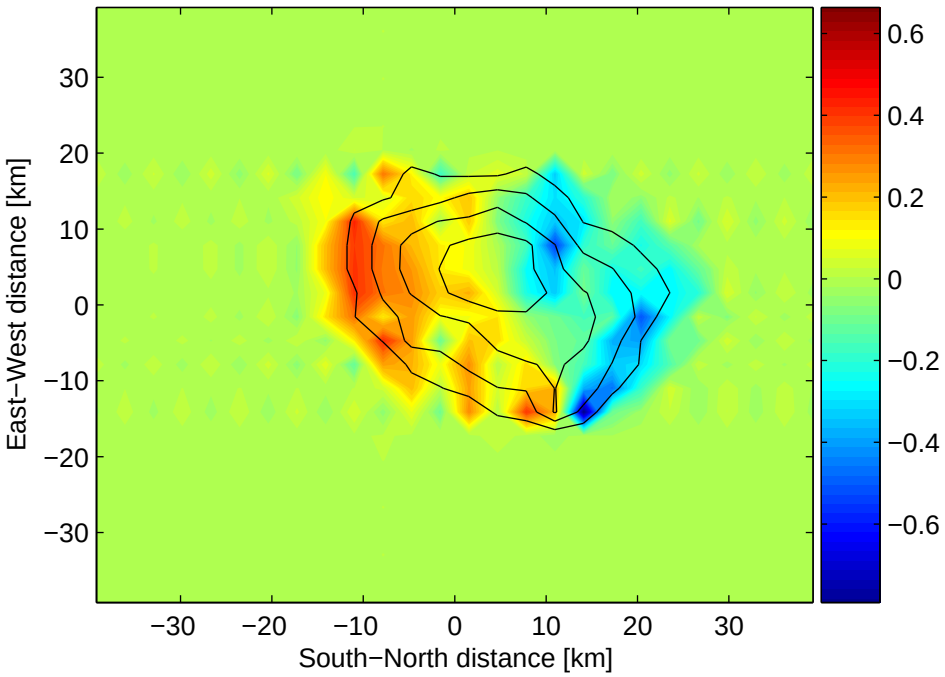

Figure 4.36: Vertical wind component (m/s) at ground level for the three–dimensional, steady and hydrostatic flow over Hofsjökull. The flow direction is from south to north. The figure shows the view from above. The topography is shown by the black lines.

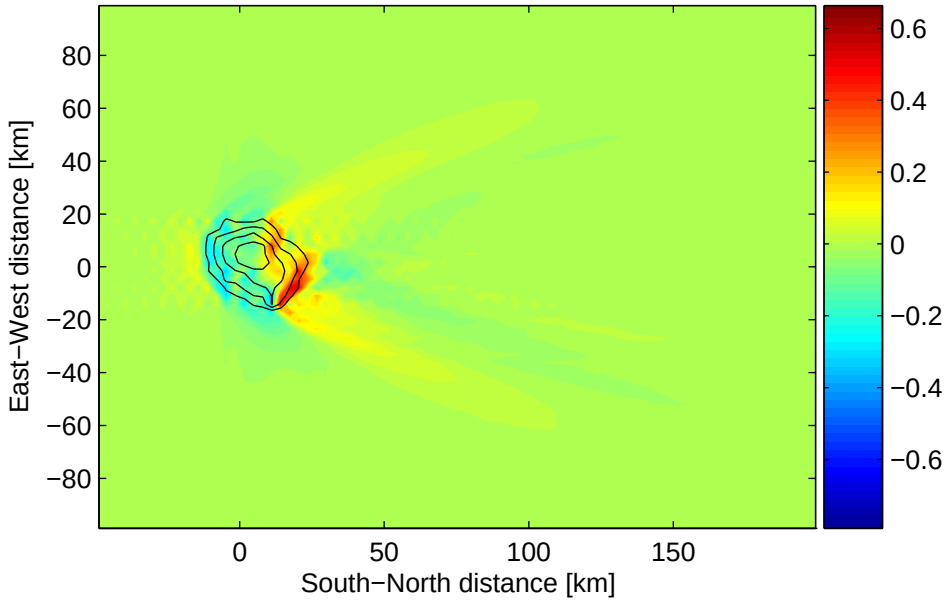

Figure 4.37: Vertical wind component (m/s) in 2500 metres for the three–dimensional, steady and hydrostatic flow over Hofsjökull. The flow direction is from south to north. The figure shows the view from above. The topography is shown by the black lines.

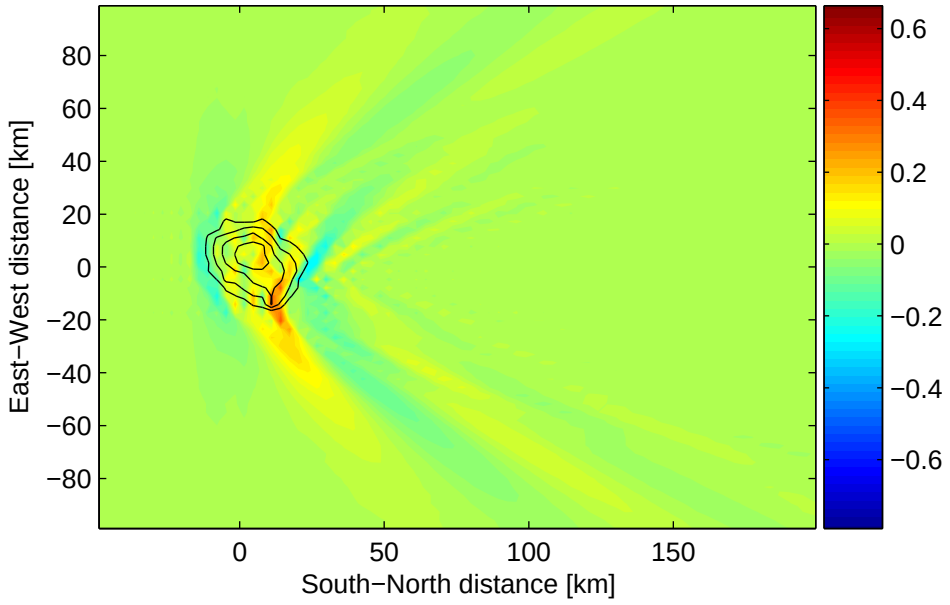

Figure 4.38: Vertical wind component (m/s) in 10000 metres for the three–dimensional, steady and hydrostatic flow over Hofsjökull. The flow direction is from south to north. The figure shows the view from above. The topography is shown by the black lines.

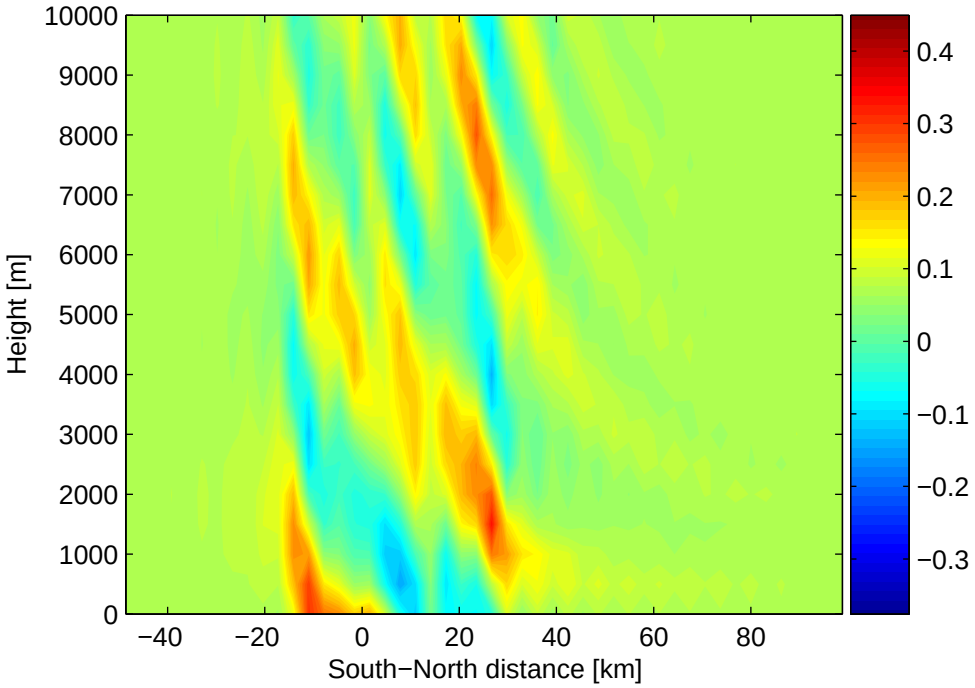

Figure 4.39: Vertical cross section of the vertical wind component (m/s) along the flow axis for the three dimensional, steady and hydrostatic flow over Hofsjökull. The flow direction is from south to north.

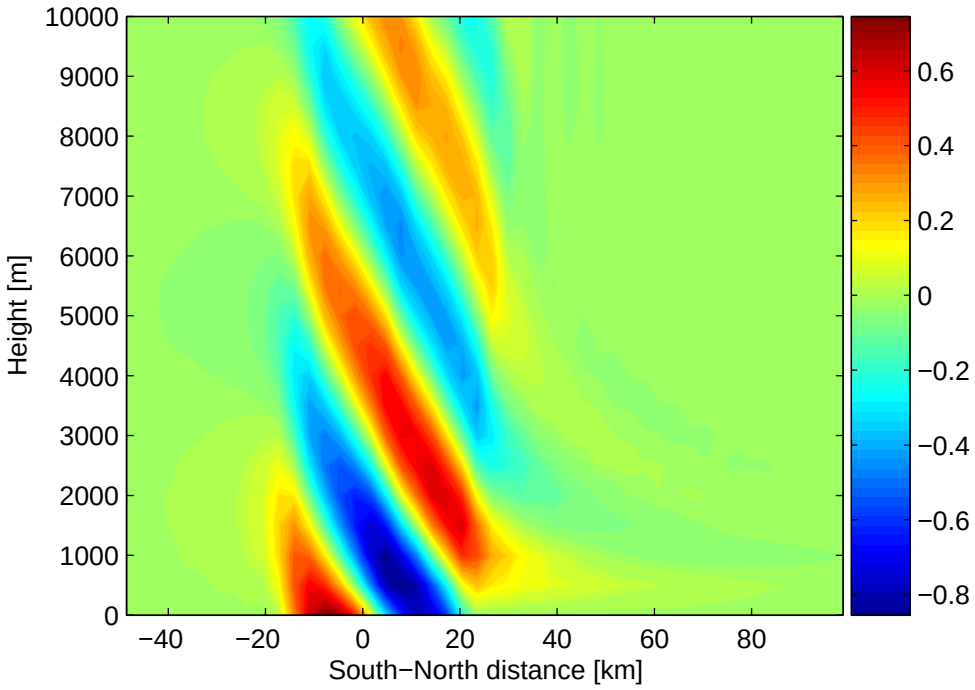

Figure 4.40: Vertical cross section of the vertical wind component (m/s) along the flow axis for the three dimensional, steady and non-hydrostatic flow over an ideal mountain. The flow direction is from south to north.

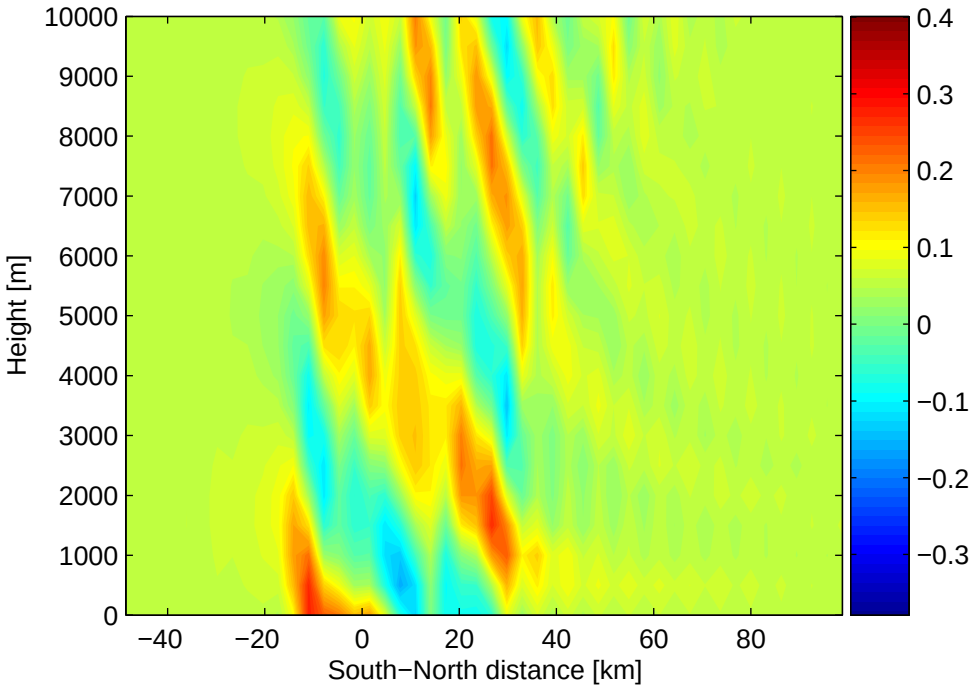

Figure 4.41: Vertical cross section of the vertical wind component (m/s) along the flow axis for the three dimensional, steady and non-hydrostatic flow over Hofsjökull. The flow direction is from south to north.

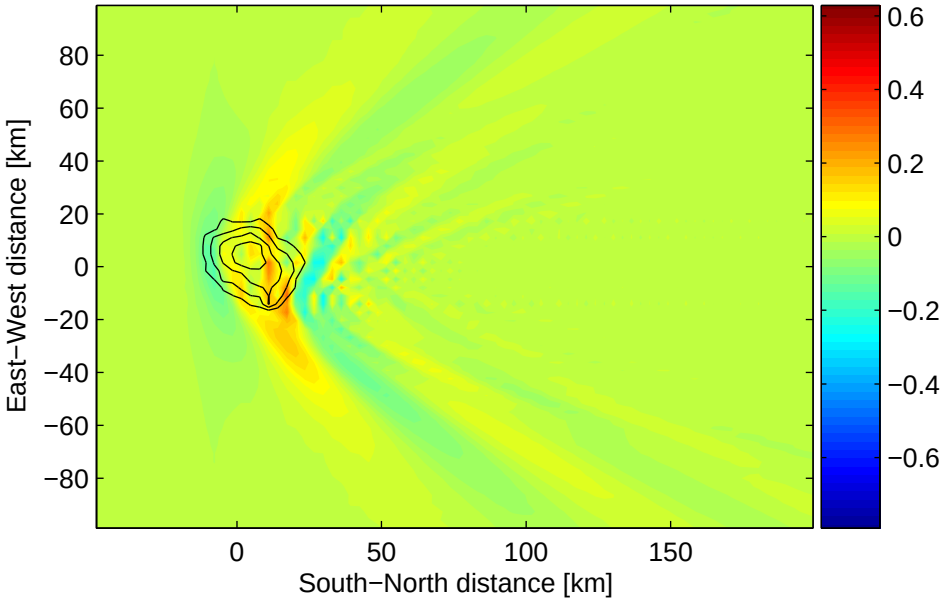

Figure 4.42: Vertical wind component (m/s) in 10000 metres for the three–dimensional, steady and non-hydrostatic flow over Hofsjökull. The flow direction is from south to north. The figure shows the view from above. The topography is shown by the black lines.

Chapter 5

Discussion

5.1 Linear 2D Model

The comparison of the two–dimensional model of the ideal mountain with the Hofsjökull profile shows that only the vertical wind perturbation differs significantly. The up and downwind fields are separated more distinct than the horizontal wind field or the pressure perturbation. The vertical wind component is directly related to the lower boundary condition, equation (4.1), from chapter 4.7 and thus to the gradient of the topography. The comparison of the measured pressure disturbance profiles with the ones from the linear model show that the values have the same order of magnitude.

5.2 Linear 2D Model with Pressure as Lower Boundary

In chapter 4.8 the calculations of the two dimensional model, with pressure disturbances prescribed at the lower boundary, are presented. The pressure profiles from 5 August 00:00 to 12:00 LT, 7 August to 10 August and 15 August to 16 August were used as the lower boundary. The profiles show high pressure on the windward side of the mountain and low pressure on the lee side of the mountain, as suggested by linear theory. Significant in all these pressure profiles is the narrow maximum near the stations HN10 and N3. The local maximum appears both for southerly and northerly winds. Even the profile from 3 August to 4 August with easterly winds shows it. Since all the neighbouring stations follow this local maximum, it is unlikely, that it is caused by a defective reading of the stations. These special stations in the north were neighboured by two smaller hills. To the west was Krokafell and

to the east Tvifell. Both had a height of approximately 100 metres relative to the surroundings. It is possible that the local maximum has to be related to local orographic phenomena.

The wind observations of these periods show higher velocities on the leeward side of the mountain. This fact matches as well the linear theory of fast down slope winds generated by orographic waves. The variability both of wind speed and wind direction is higher on the lee side, probably caused by a higher wave activity on the lee side. The standard deviations show a tendency to be higher on the leeward side, as well suggesting a higher wave activity there.

The balloon soundings on August 5 showed constant winds with approximately 5 to 7 m/s. The temperature profiles were adiabatic almost all the time. An inversion can be found at 16:28 and 18:33 LT in about 1000 metres and relative humidity is decreasing in that height by 20%. But these observations are more likely caused by different air masses or cloud phenomena. The *KALI* pilots reported a strong wind shear in that height and the ascents were made in a period of changing inflow direction. The period of constant inflow was in the time from 00:00 to 12:00 LT.

The results of the model calculations in chapter 4.8 are heavily influenced by the sharp pressure disturbance gradient in the north. The decay of the disturbance in the south and north was estimated and thus has to be treated with caution.

The calculations for the profile from 7 August to 10 August show a more similar structure compared with the calculations from chapter 4.7. The results of the model with vertical wind shear show increasing wavelength and tilt with increasing wind speeds. The structures of all three calculations are similar. The perturbation fields near the ground are smaller than those in higher regions. The calculations, in which the wind speed declines with height at the ground, are very similar (figure 4.28 and 4.29). There, the separation of the perturbation fields is preserved because of the decline of the amplitude. In the calculation with the wind profile from 7 August 10:33 LT (figure 4.27), the perturbations are not separated at the ground. The horizontal extend is growing with increasing wind speeds. So do the amplitudes of the perturbations.

The temperature profiles of the period from 7 August to 10 August show slight inversions at about 600 and 1200 to 1300 metres from time to time (figure 4.12), which might be related to wave activity. Remarkable is the wind profile from 8 August 12:30 LT (figure 4.11). One can see a wavelike behaviour of the horizontal wind speed. It is oscillating between 1 and 4 m/s in the region up to 1500 metres. The wavelength is approximately 500 to 600 metres. The calculations of the model with the wind profile from 7

August, 10:33 LT (figure 4.27) show similar wavelengths near the ground. This special profile showed increasing wind velocities up to 1800 metres with values from 1 to 4 m/s. The calculations mentioned above might therefore be a good representation of the wave over the mountain up to 2000 metres.

The disturbance calculated with the profile from 15 August to 16 August is once heavily influenced by the sharp gradient in the north. However the disturbance fields over the mountain are not separated that much. Due to cloud cover, no significant balloon and *KALI* soundings could be done. The high pressure field on the windward side of the mountain is shifted to the north compared with the profile from 5 August. Slightly higher wind velocities of the flow in the north may have caused this. For the wind profile the sounding from Keflavik was used. This profile shows relative constant wind with values of 10 to 20 m/s, which leads to a regularly structure of the profile.

The calculations above included the special structure of the pressure profiles, as for example the thin maxima in the north. Assuming linear behaviour, the model could give an idea of the wave structure above the mountain. The calculations for Hofsjökull from chapter 4.7 was not able to reproduce this thin maxima since it was probably caused by a local orographic phenomena. Another advantage is the possibility to include varying wind profiles. The calculations showed that the wavelength, tilt, amplitude and the horizontal extend of the perturbation follows the wind speed.

The comparison of the height profile of Hofsjökull with a recalculated one shows significant differences. The recalculated profile is broader and higher than the Hofsjökull profile. It shows two maxima and there are two depressions flanking the recalculate "mountain".

5.3 Linear 3D Model

The results of the three dimensional model suggest that the steep slopes in the south of Hofsjökull and to the south and north of Miklafjell have a major impact on the wave generation. The wind perturbation above and in the lee of Miklafjell is much larger than over the rest of the mountain. It even penetrates further up. The perturbations are well separated. There are two downwind fields in the lee of the mountain near the ground and one separate upwind field directly south of Miklafjell.

Comparing the vertical cross sections of the two and three–dimensional model (figure 4.21 and 4.39) one can see that both have several smaller up and downwind perturbations. However, the three–dimensional calculations show smaller amplitudes. The perturbation for the two–dimensional model

is concentrated over the mountain while the three–dimensional model shows trailing perturbations in the lee of the mountain, especially near the ground.

The calculations were repeated for a non-hydrostatic regime. The calculations for the ideal mountain did not show any significant differences. The results for the Hofsjökull profile however had a more distinct wave pattern in the lee of the mountain near the ground. This is probably caused by the more irregular shape of the mountain profile, which might produce a stronger non-hydrostatic influence. There were as well higher amplitudes in the lee of the mountain in the region from 7000 to 10000 metres.

Chapter 6

Summary

The *FLOHOF*-field campaign took place from 20 July to 24 August, 2007. During that time, 18 autonomous weather stations had been placed on and around Hofsjökull. The stations were provided by the Swiss Federal Institute of Technology Zurich (ETH), the Geophysical Institute in Bergen (GFI) and the Meteorological Institute in Munich (MIM). In addition balloon soundings for wind profile measurements and soundings for temperature and relative humidity profiles via remotely controlled model planes (*KALI*) were conducted.

The measured parameters were presented in this work. The absolute pressure had been reduced to pressure disturbances for each station. The covariances and correlations of these pressure disturbances were calculated. Three regions of high correlation were visible. The stations in the south formed one group, the stations on the mountain a second and the last group was built by the stations in the north.

Pressure disturbance profiles had been calculated for three periods of northerly or southerly flow. All profiles showed high pressure on the windward side and low pressure on the leeward side. A local pressure maximum was always visible in the north of the mountain, probably caused by local phenomena through shallow mountains there.

A two dimensional–model was built following the basic linear theory of hydrostatic gravity waves. The lower boundary condition was one which assumes that air parcels have to follow topography when travelling over a mountain. This model was applied on an ideal mountain, as well as on a Hofsjökull topography. The calculations showed a vertical propagating wave with windward–tilted phase lines. The vertical wind perturbation for the Hofsjökull profile was separated in several smaller perturbation regions.

A second two–dimensional model was investigated, in which the lower boundary condition was formed by the pressure observations at the ground.

This model was applied to all three pressure perturbation profiles mentioned above. Wind shear was included in this model. The wind profiles of some balloon soundings and vertical soundings from Keflavik, performed by the University of Wyoming, were used for the calculations. The results showed an increasing wavelength, tilt of the phase lines, amplitude and horizontal extend with increasing wind speed. The calculations for the profiles of northerly wind showed a sharp pressure gradient in the north. The result of the profile of southerly wind showed more similarity to that of the hydrostatic model mentioned before.

The last model was three–dimensional one. The "parcel" boundary condition was used once again. The calculations were done for southerly winds. The results suggested that the Miklafjell summit to the east of Hofsjökull has a major impact on the wave generation above the mountain. The vertical wind fields over and in trail of Miklafjell were greater and penetrating further up than the ones over the rest of the mountain, a fact that is caused by the steep slopes around Miklafjell. A comparison of hydrostatic and non-hydrostatic calculations showed differences on the lee side of Hofsjökull. The amplitudes in higher regions in the lee of the mountain were stronger for the non-hydrostatic model. Near the ground, the non-hydrostatic calculations showed a more distinct wave pattern in the lee of Hofsjökull.

Chapter 7

Acknowledgements

I would like to thank Joseph Egger, Ute Egger, Joachim Reuder, Haraldur Olafsson, Günther Zängl, Thomas Spengler, Tor de Lange, Wolfang Schäper, Stephan Lämmlein, Stephanie Mayer, Markus Ablinger, Markus Garhammer, Marius Jonassen, Trausti Jonsson, Tomas Johannesson, Olafur Rögnvaldsson, Halfdan Agustsson, Sveinn Brynjolfsson, Martin Müller, Christian Lindenberg, Sylvie Malardel, Pascal Brisset, Jakob Amphlett, Stefanie Vogl.

Chapter 8

References

Ablinger, M. 2006: Daten und Ergebnisse der Messkampagne AllgEx 2005 im Allgäu und Lechtal. *Diploma thesis, Meteorological Institute University Munich.*

AANDERAA, November 2006: data sheet D161.

AANDERAA, December 2006: data sheet D276.

AANDERAA, January 2003: data sheet D271.

AANDERAA, November 2006: data sheet D300.

AANDERAA, November 2006: data sheet D151.

Bannon, P.R. and Zehnder, J. A. 1985: Surface Pressure and Mountain Drag for Transient Airflow over a Mountain Ridge. *Journal of the atmospheric sciences*, Vol. 42, 2454–2462

Bell, T. H. 1974: Lee waves in stratified flows with simple harmonic time dependence. *Journal of Fluid Mechanics*, Vol. 67, 705–722

CAMPBELL, 2007: data sheet

Holton, J. R. 2004: An introduction to dynamic meteorology. *Elsevier Academic Press*, 196–204.

Keller, T. L. 1994: Implications of the Hydrostatic Assumption on Atmospheric Gravity Waves. *Journal of the atmospheric sciences*, Vol. 51.

Lott, F. and Teitelbaum, H. 1993: Topographic waves generated by a transient wind. *Journal of the atmospheric sciences*, Vol. 50, 2607–2623

Mayer, S. 2005: Daten und Ergebnisse der Messkampagne Juipitaya 2003. *Diploma thesis, Meteorological Institute University Munich.*

Schween, J. 1998: Anleitung und Theorie zum Auswertprogramm PILPLOT für die Ballonpilotierung. *Meteorological Institute University Munich.*

Scorer, R. S. 1949: Theory of waves in the lee of mountains. *Quart. J. Roy. Meteor. Soc.*, Vol. 75, 41-56.

Smith, R. B. 1979: The influence of mountains on the atmosphere. *Advances in Geophysics*, Vol. 21. p.87–230

Smith, R. B. 1980: Linear theory of a stratified hydrostatic flow past an isolated mountain. *Tellus*, Vol. 32, 348–364

Spengler, T. 2008: Gravity Waves. *Swiss Federal Institute of Technology Zurich*

Storch, H. v., Zwiers, F. W. 1999: Statistical analysis in climate research. *Cambridge University Press*, 22-23, 40.

Teixeira, M. A. C. and Miranda P. M. A. 2004: The effect of wind shear and curvature on the gravity wave drag produced by a ridge. *Journal of the atmospheric sciences.* Vol. 61, 2638–2643.

VAISALA, 2007: Instruments Catalog

www.umyo.edu

www.Vaisala.com

www.wetterzentrale.de

Appendix A

Additional Plots

The following plots show the observations of all automatic weather stations. Ingolfsskali cottage (Base–Camp of the campaign) was additional equipped with an *OPUS* pressure sensor, named N3b in these plots. The measurements of the ETH-Station near Ingolfsskali cottage are declared with N3b ETH.

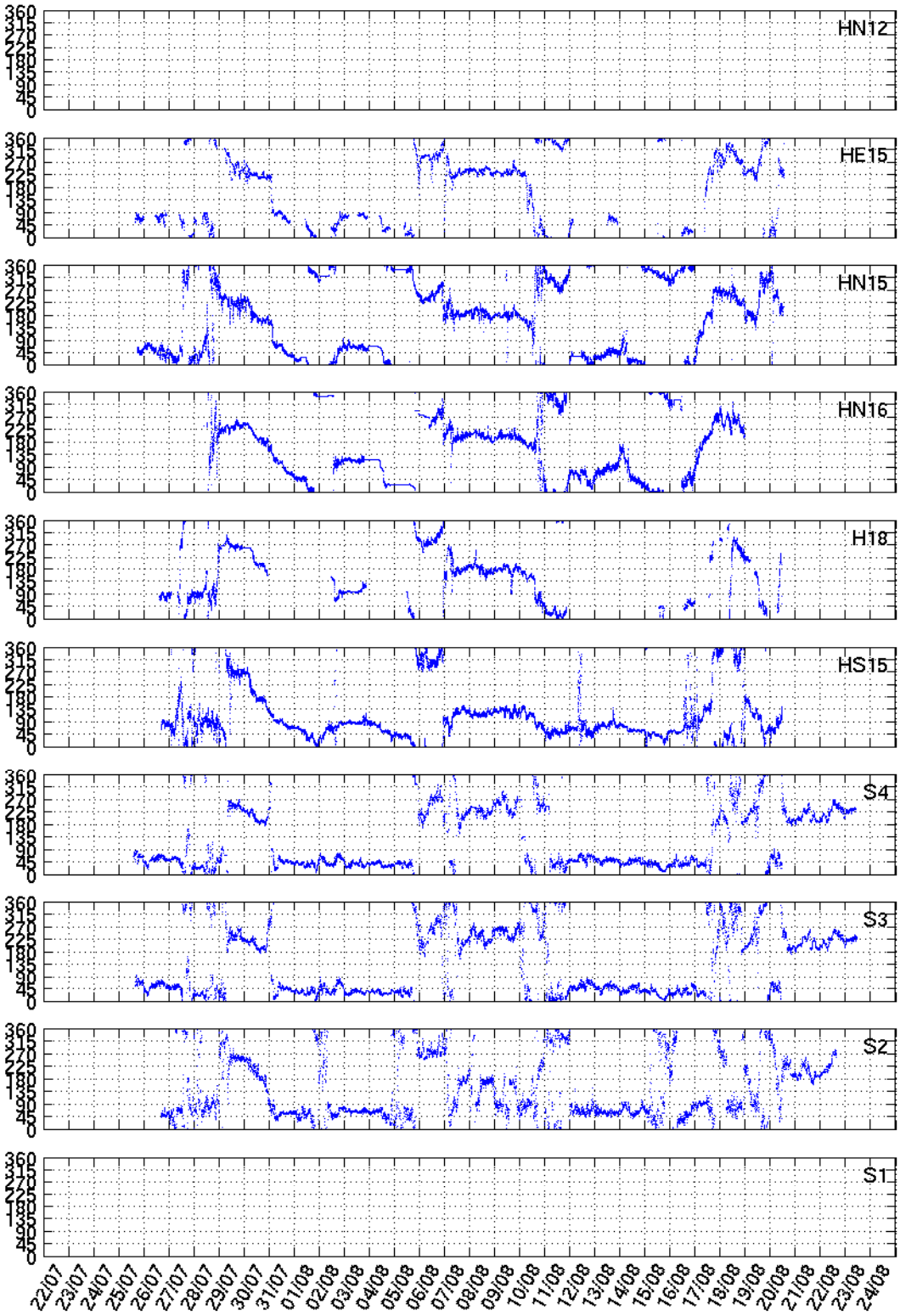

Figure A.1: Measured wind direction in degrees during the campaign. The abscissa shows day and month.

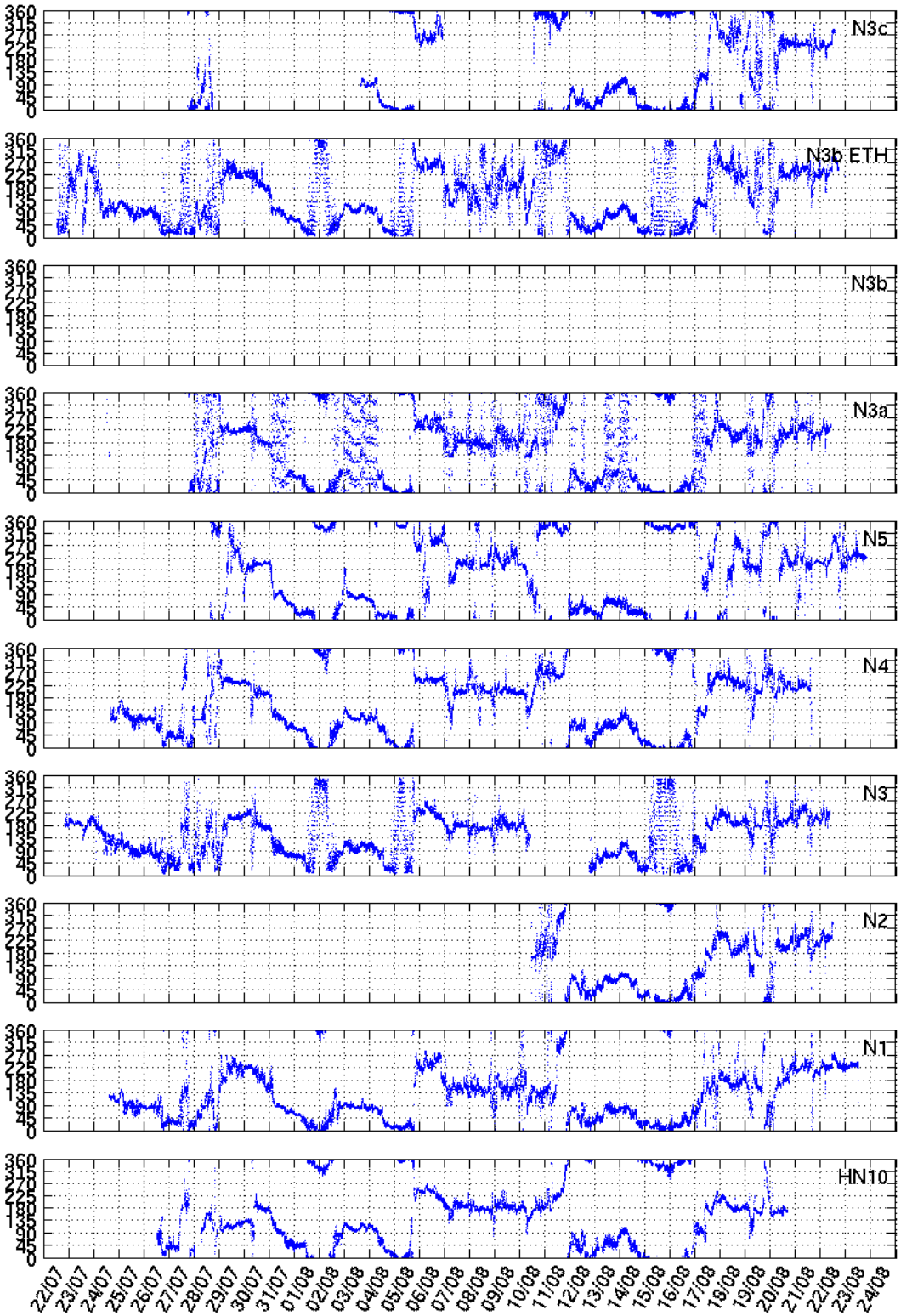

Figure A.2: Measured wind direction in degrees during the campaign. The abscissa shows day and month.

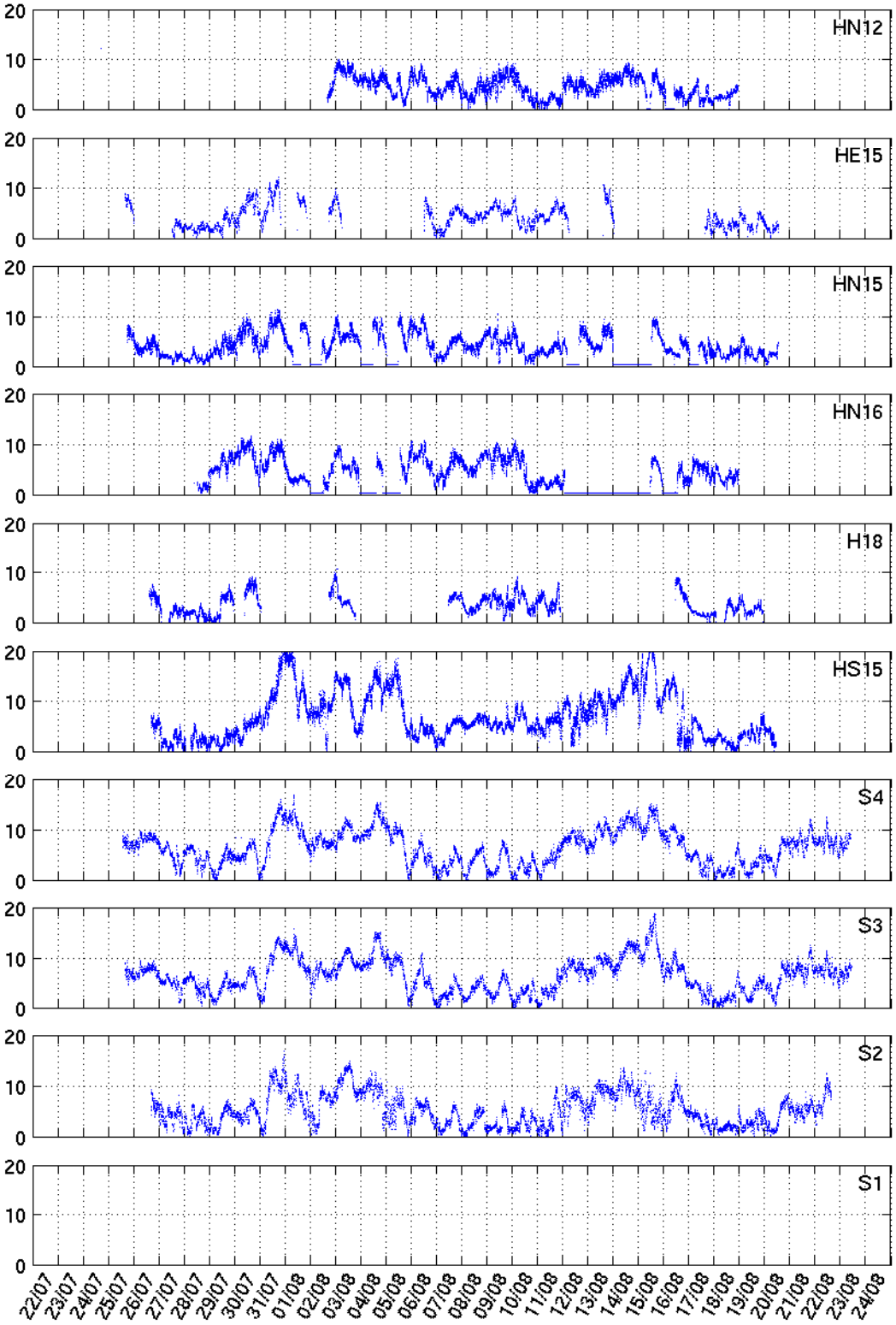

Figure A.3: Measured wind speed in m/s during the campaign. The abscissa shows day and month.

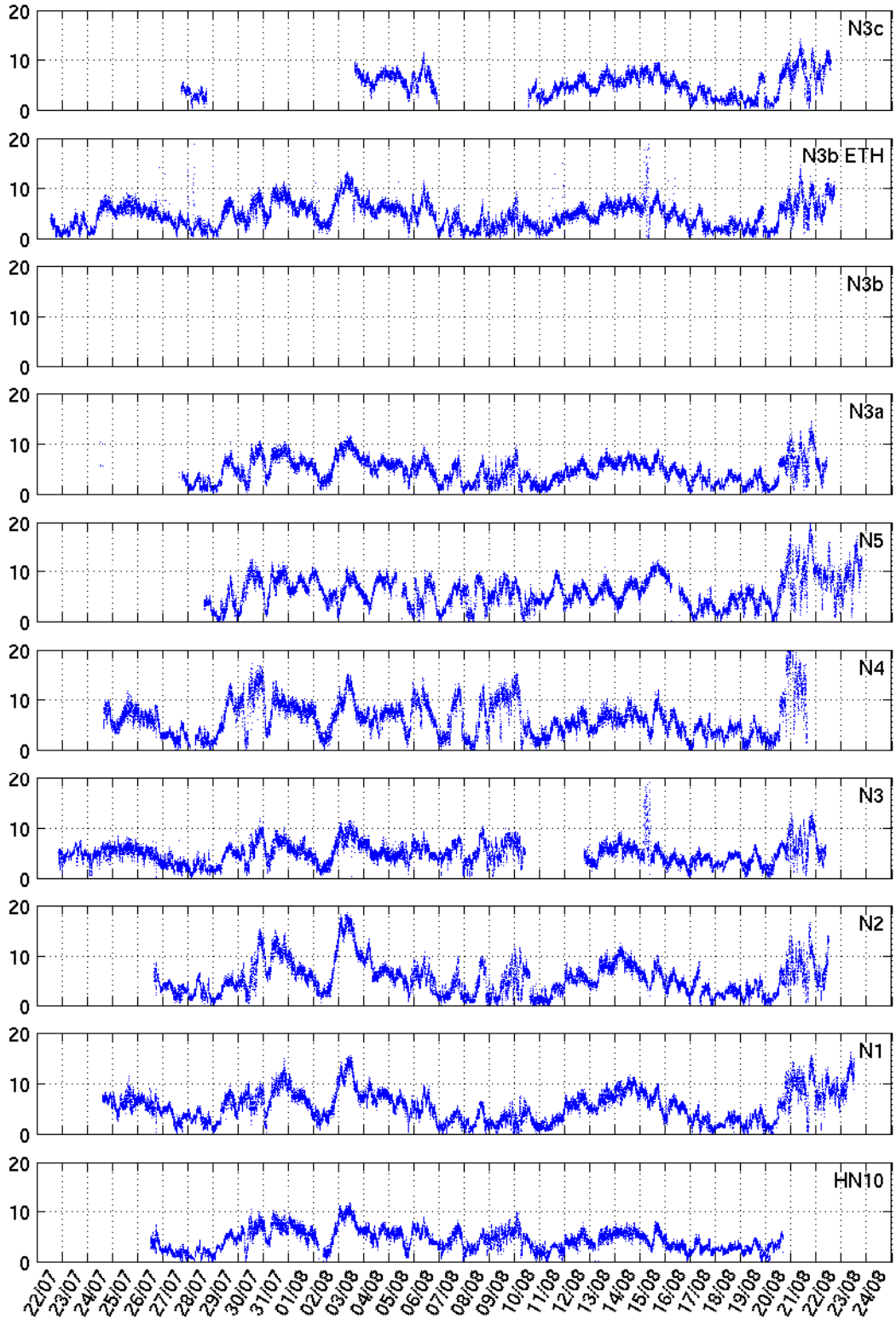

Figure A.4: Measured wind speed in m/s during the campaign. The abscissa shows day and month.

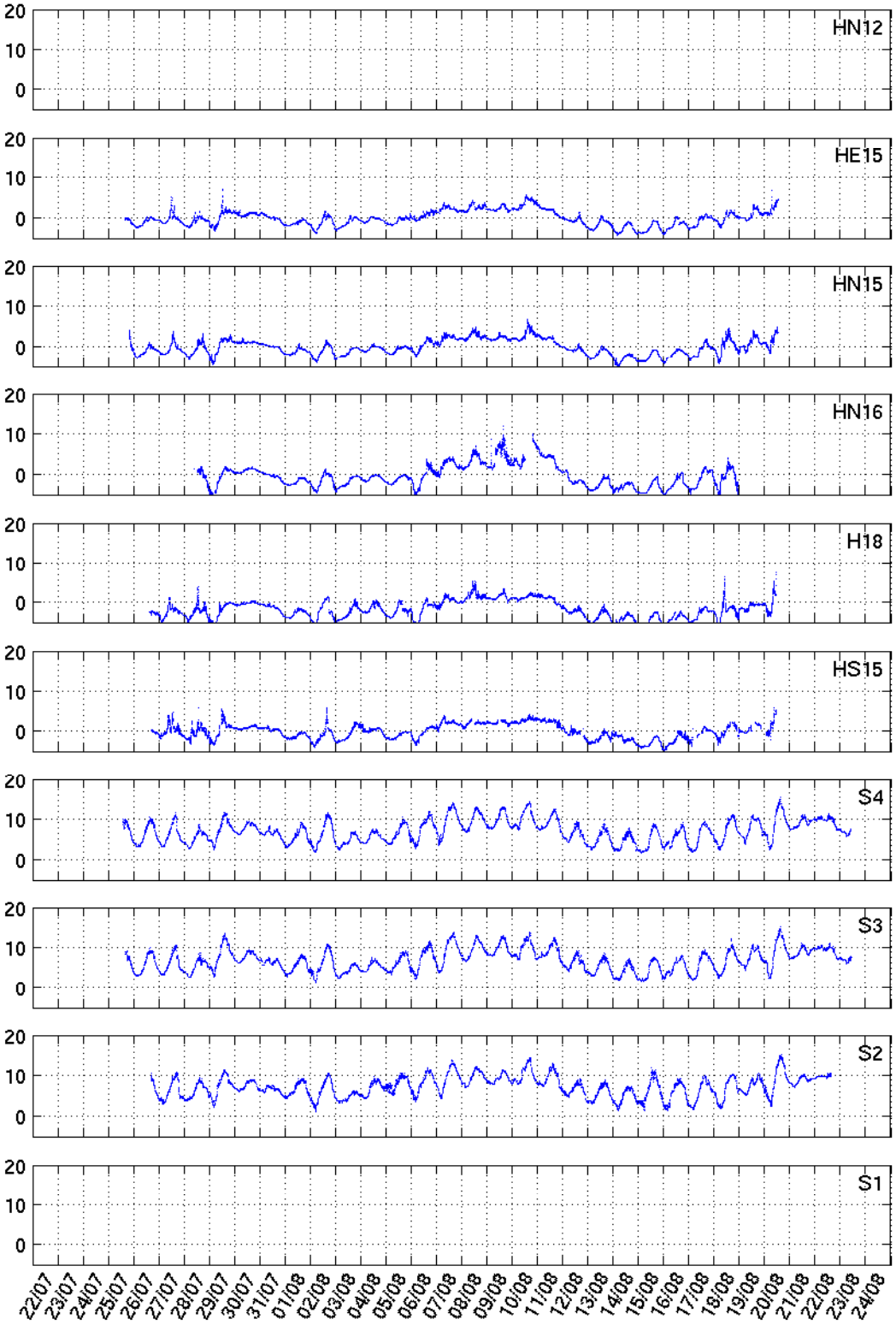

Figure A.5: Measured temperature in °C during the campaign. The abscissa shows day and month.

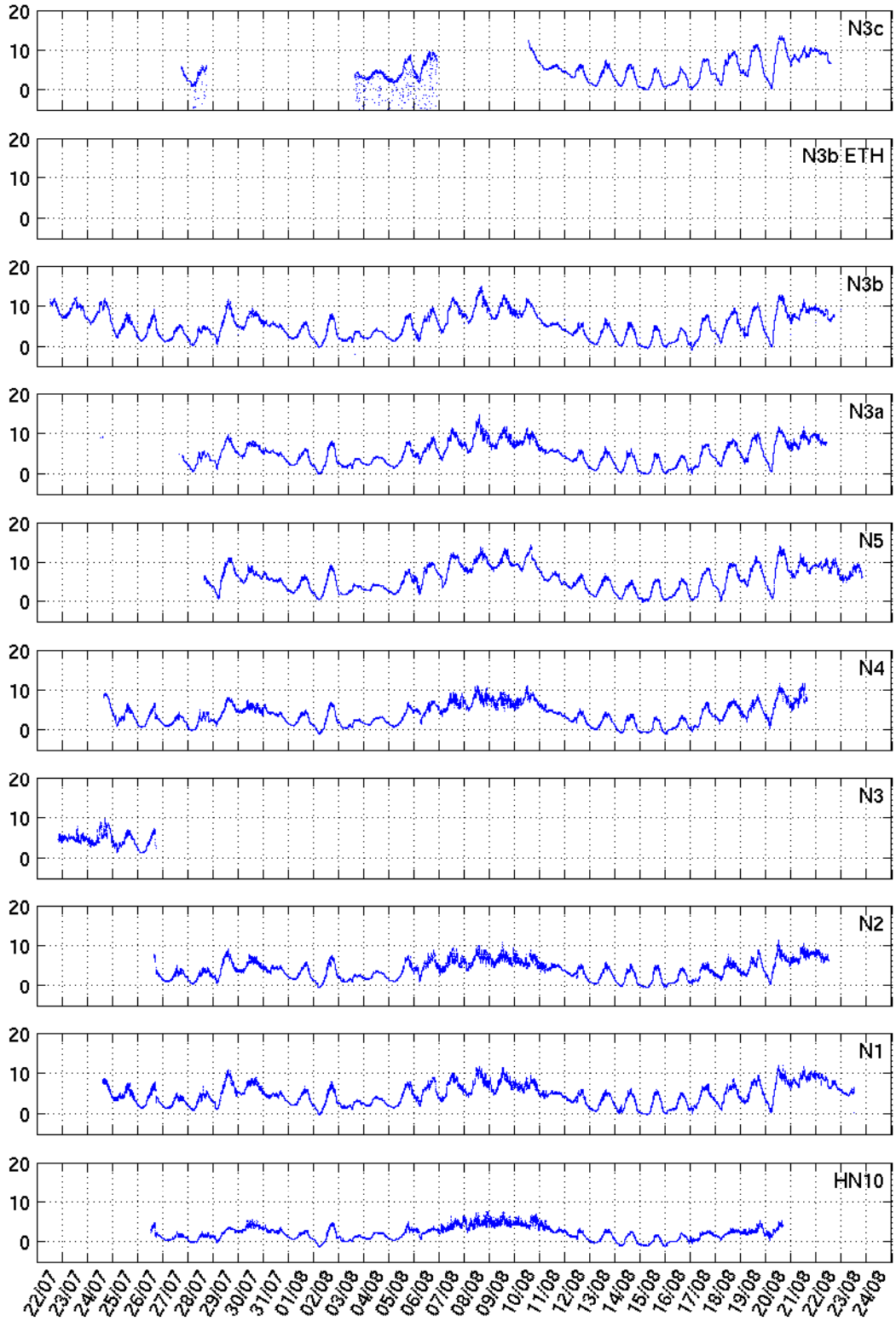

Figure A.6: Measured temperature in °C during the campaign. The abscissa shows day and month.

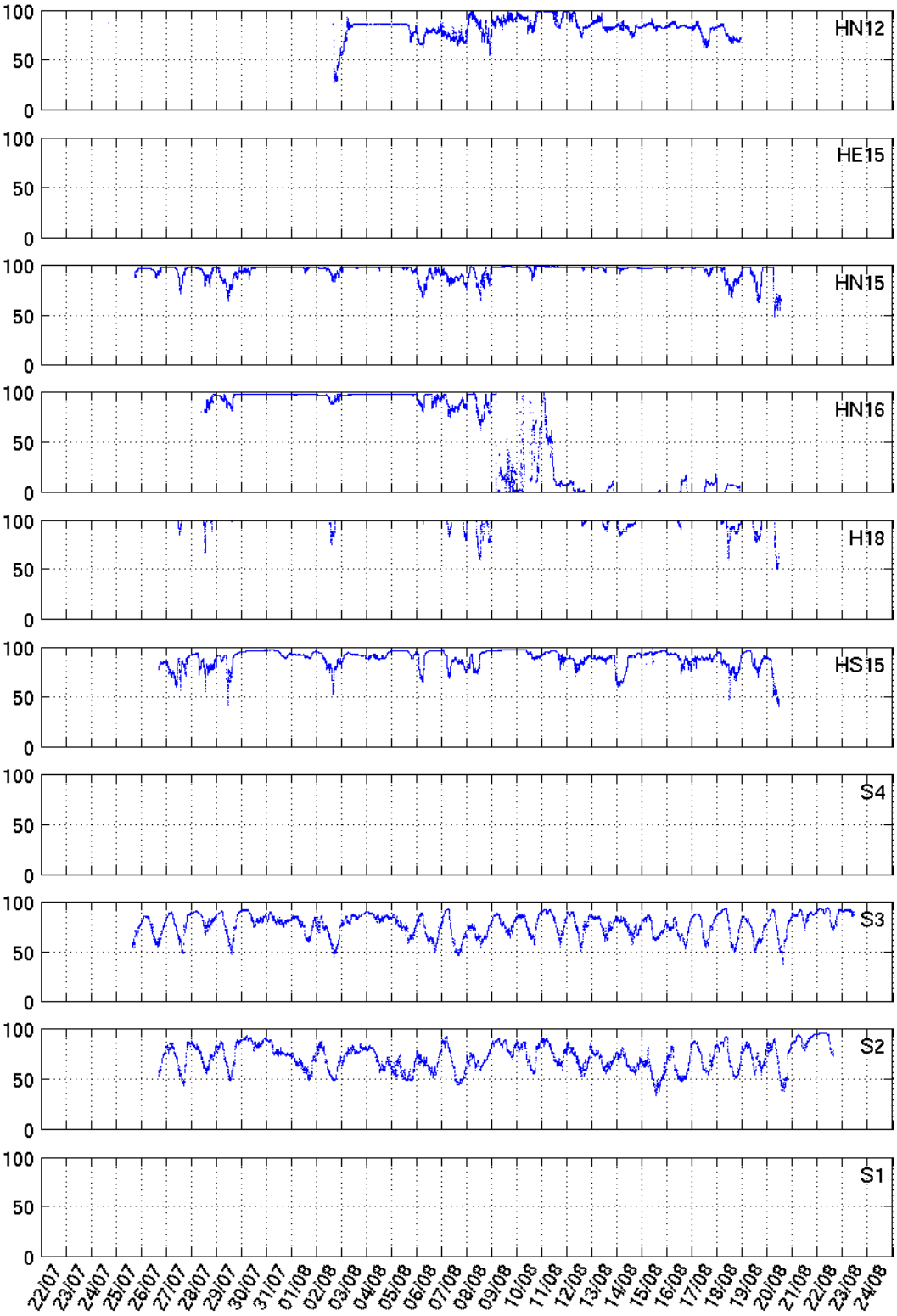

Figure A.7: Measured relative humidity in % during the campaign. The abscissa shows day and month.

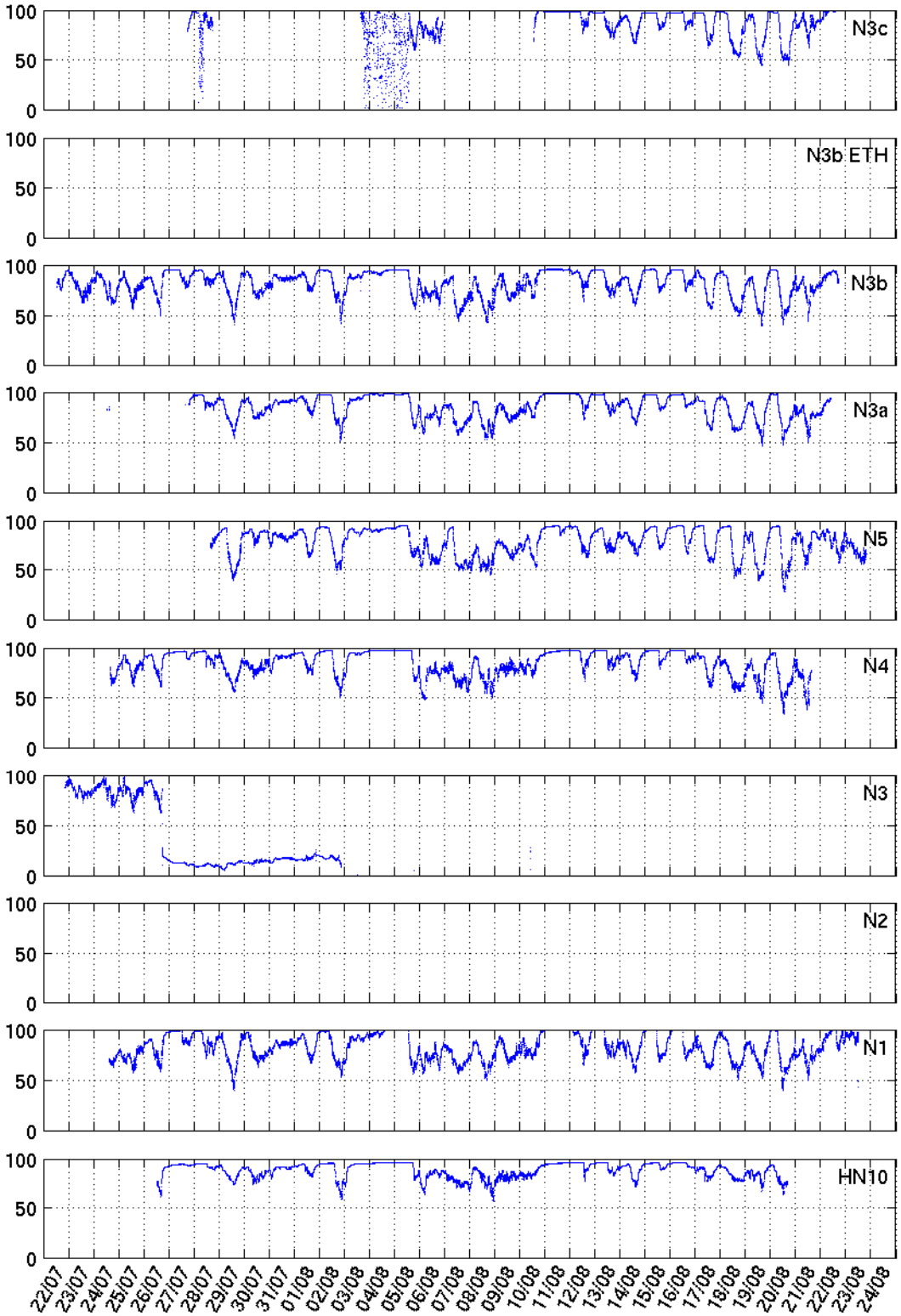

Figure A.8: Measured relative humidity in % during the campaign. The abscissa shows day and month.

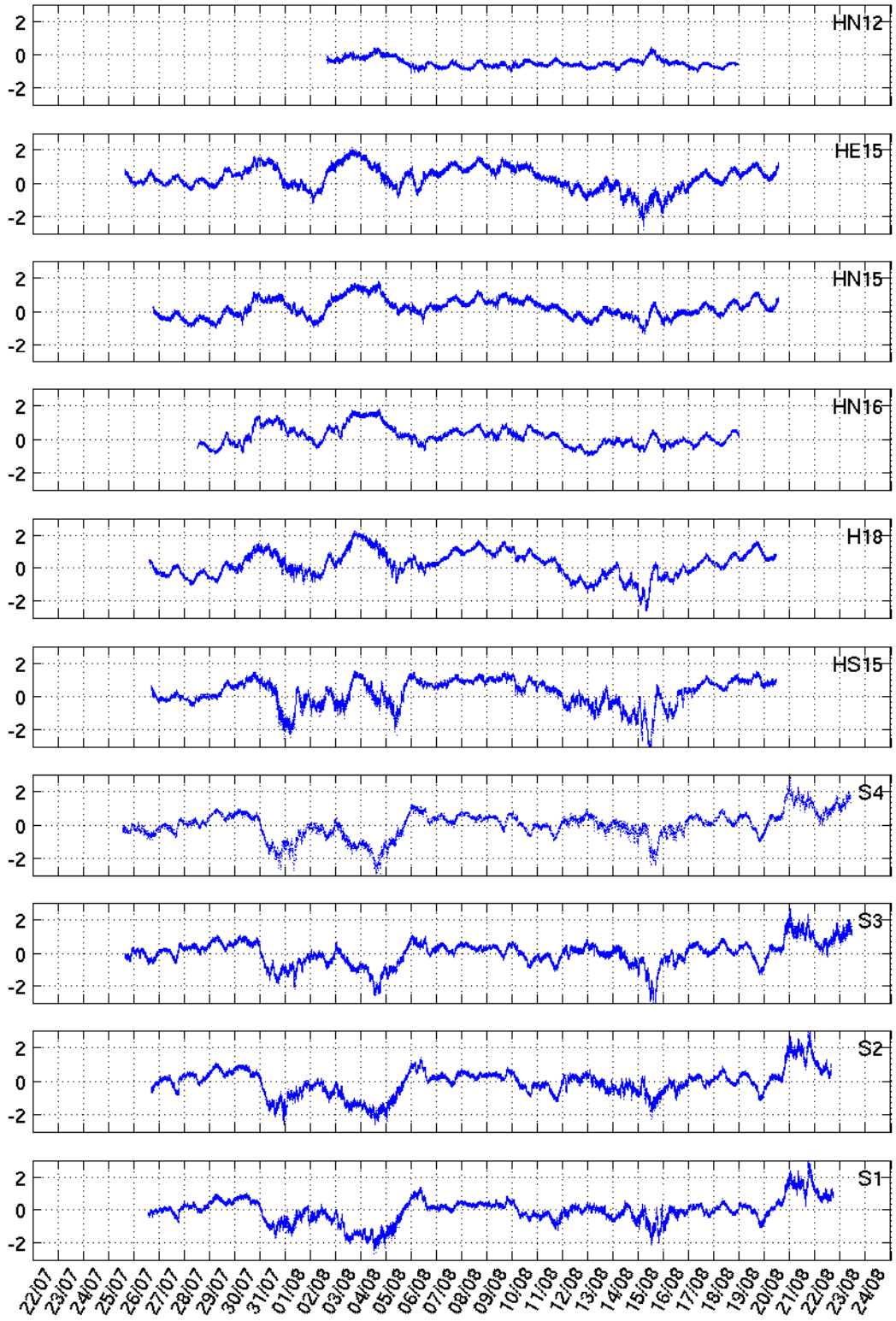

Figure A.9: Pressure perturbation in hPa during the campaign. The abscissa shows day and month.

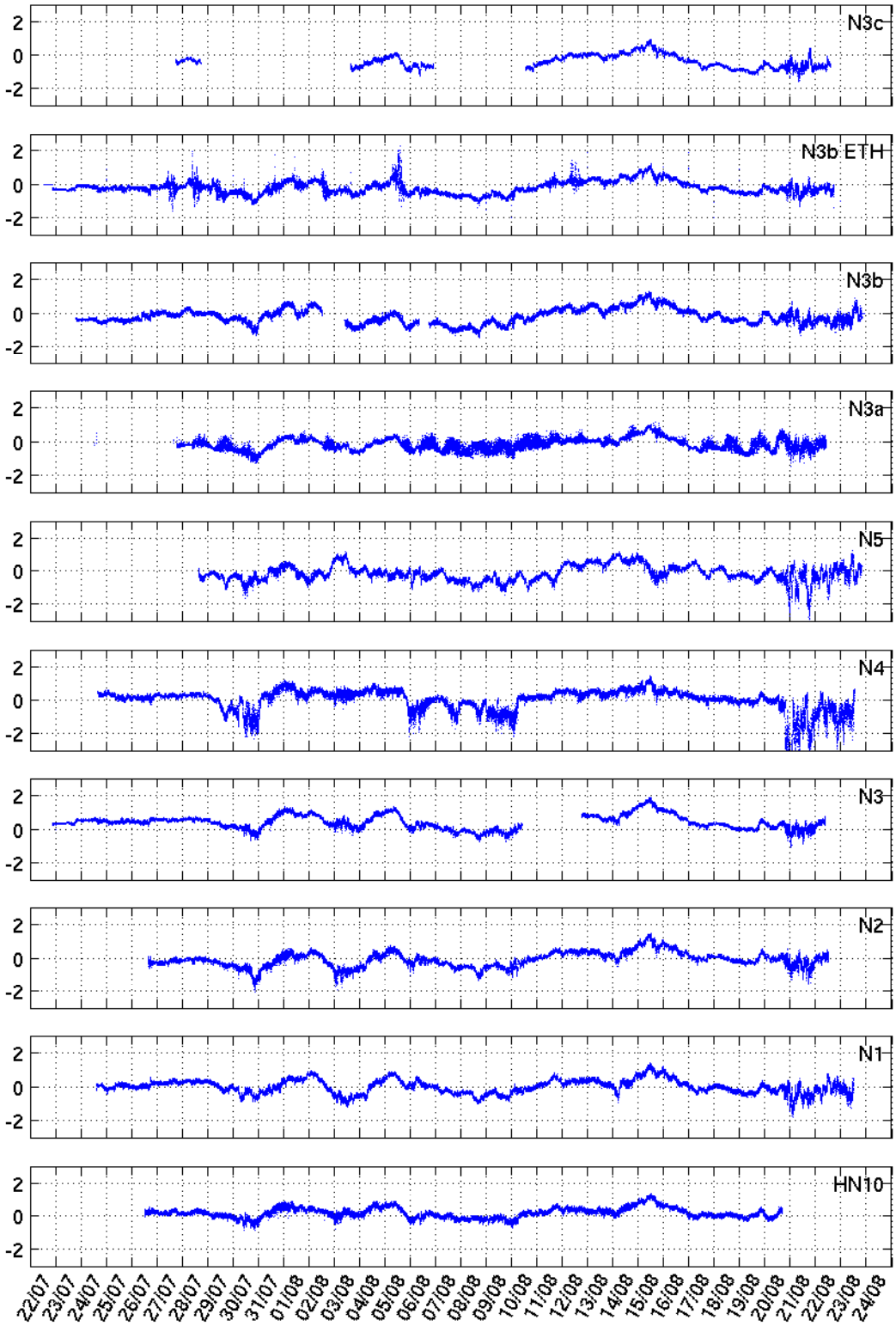

Figure A.10: Pressure perturbation in hPa during the campaign. The abscissa shows day and month.

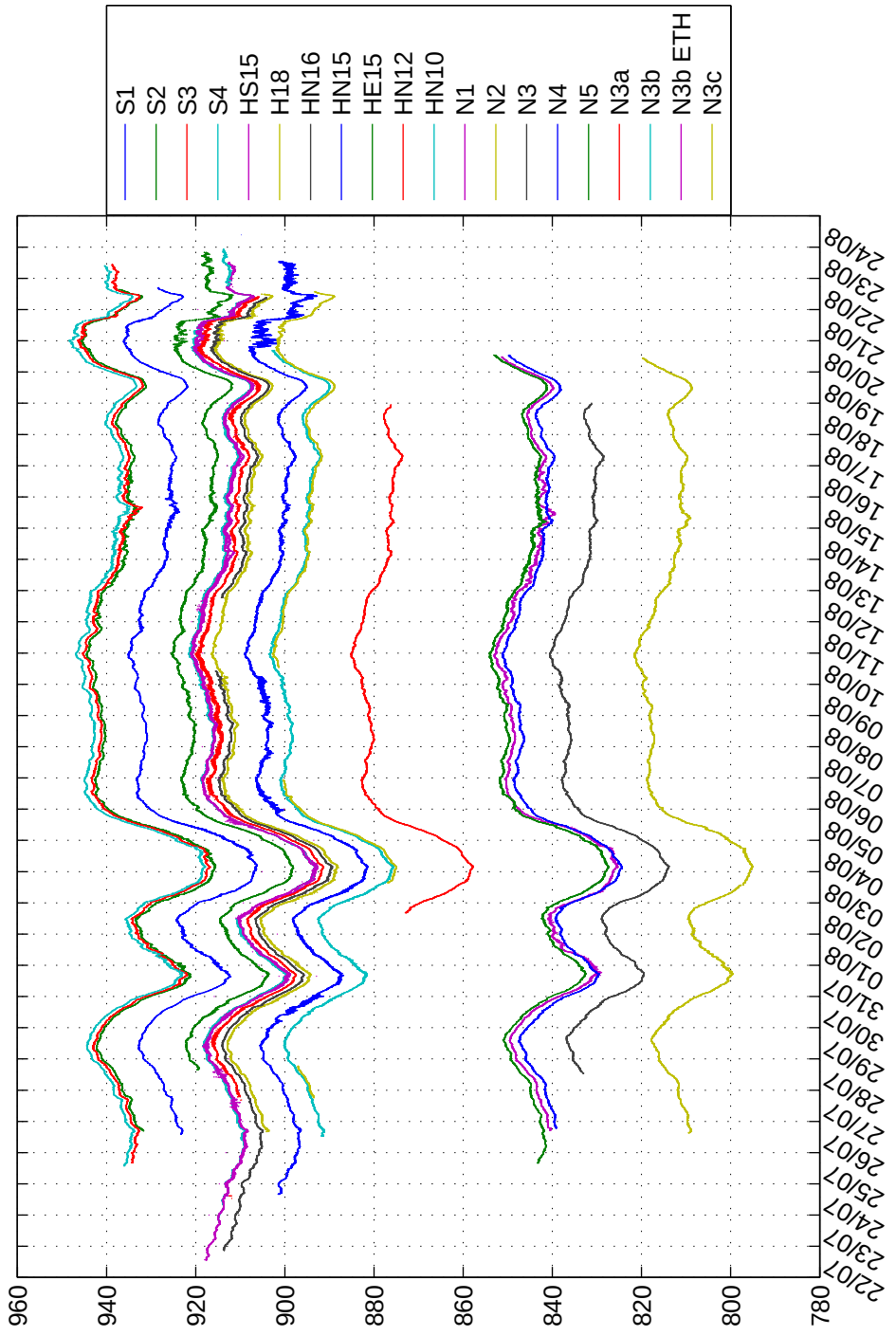

Figure A.11: Measured absolute pressure in hPa during the campaign. The abscissa shows day and month.